Reconstruction of dynamic regulatory networks reveals signaling-induced topology changes associated with germ layer specification

Emily Y. Su[1,2*], Abby Spangler[1*], Qin Bian[1,2], Jessica Y. Kasamoto[2], Patrick Cahan[1,2,3]

[1]Institute for Cell Engineering, Johns Hopkins School of Medicine, Baltimore MD 21205 USA

[2]Department of Biomedical Engineering, Johns Hopkins School of Medicine, Baltimore MD 21205 USA

[3]Department of Molecular Biology and Genetics, Johns Hopkins School of Medicine, Baltimore MD 21205 USA

* These authors made equal contributions.

Correspondence to: patrick.cahan@jhmi.edu

Declarations of interest: none

Keywords: Single cell RNA-seq, Gene regulatory network, Network inference, Directed differentiation, Gastrulation, Embryoid body, Peg3, Wnt

Abstract

Elucidating regulatory relationships between transcription factors (TFs) and target genes is fundamental to understanding how cells control their identity and behavior. Computational gene regulatory network (GRN) reconstruction methods aim to map this control by inferring relationships from transcriptomic data. Unfortunately, existing methods are imprecise, may be computationally burdensome, and do not uncover how networks transition from one topology to another. Here we present Epoch, a computational network reconstruction tool that leverages single cell transcriptomics to infer dynamic network structures. Epoch performs favorably when benchmarked using data derived from *in vivo*, *in vitro,* and *in silico* sources. To illustrate the usefulness of Epoch, we applied it to identify the dynamic networks underpinning directed differentiation of mouse embryonic stem cells (ESC) guided by multiple primitive streak induction treatments. Our analysis demonstrates that modulating signaling pathways drives topological network changes that shape cell fate potential. We also find that Peg3 is a central contributor to the rewiring of the pluripotency network to favor mesoderm specification. By integrating signaling pathways with GRN structures, we traced how Wnt activation and PI3K suppression govern mesoderm and endoderm specification, respectively. Finally, we compare the networks established in *in vitro* directed differentiation of ESCs to those in *in vivo* gastrulation and mesoderm specification. The methods presented here are available in the R package Epoch, and provide a foundation for future work in understanding the biological implications of dynamic regulatory structures.

Introduction

Gene regulatory networks (GRNs) model the regulatory relationship between a set of regulators, or transcription factors (TFs), and their target genes. The topology of these networks, defined by edges that map regulatory interactions between TFs and targets, offers a molecular-level view of a controlled system in which genes work together as part of a framework to accomplish specific cell functions (Karlebach and Shamir, 2008; Le Novère, 2015). Uncovering the topology of these GRNs is fundamental in answering a number of questions including: understanding how cellular identity is maintained and established (Davidson and Erwin, 2006), elucidating mechanisms of disease caused by dysfunctional gene regulation (Morgan et al., 2020; Qin et al., 2019), and finding novel drug targets among others (Carro et al., 2010). In the context of cell fate engineering, accurate mapping of GRNs would enable the identification of TFs required to activate expression of target genes of interest such that we could more accurately control cell fate transitions or cell behavior (Cahan et al., 2021; Rackham et al., 2016). Unfortunately, how best to map these relationships remains both an experimental and computational challenge.

Experimental approaches, including ChIP-ChIP and ChIP-seq, have provided valuable insights into identifying regulatory targets and TF binding site motifs of specific TFs in certain cell lines and cell types. Similarly, chromatin accessibility assays that detect transcription factor binding site (TFBS) footprints at regulatory genomic regions, such as ATAC-Seq (Buenrostro et al., 2013), enable the inference of regulatory networks. However, these types of experimental approaches are generally limited in scope (e.g. ATAC-defined networks are limited to TFs with known motifs) and scalability (e.g. it is infeasible to perform ChIP-seq for all TFs in all cell types). For these reasons, computational methods to efficiently infer GRN structures are needed. Existing methods have leveraged advances in data collection and machine learning approaches that have allowed for the statistical inference of GRNs via gene expression data. These include tools that rely on information theoretic measures (Faith et al., 2007; Margolin et al., 2006; Meyer et al., 2007), ensemble methods (Huynh-Thu et al., 2010), Bayesian approaches (Yu et al., 2004; Hartemink, 2005), or differential equation-based (ODE) approaches (di Bernardo et al., 2005). Unfortunately, computational methods developed to date suffer from several drawbacks including low precision and low sensitivity. Some of the leading contributors to the low performance include the difficulty in distinguishing direct from indirect interactions (Marbach et al., 2010), the confounding effects of Simpson's Paradox (Trapnell, 2015), and the fact that bulk derived data does not offer perturbation sufficient to detect true

95 regulatory relationships (Stark et al., 2003). Attempts to ameliorate these by aggregation across
96 methods have met with modest success (Marbach et al., 2012).
97 With the advent of droplet-based systems for single-cell RNA-sequencing (Klein et al.,
98 2015; Macosko et al., 2015; Zheng et al., 2017), and the corresponding rapidly growing body of
99 single-cell transcriptomic data, computational analysis techniques have seen widespread
100 advancement in harnessing the single-cell resolution to identify cell types and states (Villani et
101 al., 2017) and to trace developmental trajectories (Treutlein et al., 2014). Of particular interest,
102 trajectory inference (TI) methods, or pseudotemporal ordering methods, such as the
103 transcriptomic-based methods Monocle (Trapnell et al., 2014), Slingshot (Street et al., 2018),
104 and DPT (Haghverdi et al., 2016), as well as cytometry-based methods such as SPADE (Qiu et
105 al., 2011), have allowed for computational modelling of dynamic processes like cell
106 differentiation. Such methods order cells in an unbiased fashion along a trajectory following a
107 linear, bifurcating, or more complex graph structure. In doing so, TI methods have proven
108 valuable in the identification of novel cell subpopulations (Chen et al., 2016) and the elucidation
109 of differentiation trees (Velten et al., 2017).
110 Unsurprisingly, several recently published tools have aimed to take advantage of the
111 resolution offered by single-cell transcriptomics to infer GRN structures (Aibar et al., 2017;
112 Matsumoto et al., 2017; Qiu et al., 2020). Just like their bulk counterparts, these methods can
113 be categorized into information theoretic, ensemble, Bayesian, and ODE approaches.
114 Unfortunately, they also suffer from similar limitations, and aside from low precision and
115 sensitivity (Chen and Mar, 2018), many of these methods are computationally burdensome,
116 limiting users' ability to hone analysis through iterative application (Bonnaffoux et al., 2019).
117 Additionally, though many of these methods employ pseudotemporal analysis to aid in
118 reconstruction, they are limited in their ability to explain how network topology evolves over
119 time. Importantly, we define a dynamic topology as one that exhibits changes in the edge-level
120 regulatory relationships between TFs and targets over time (i.e. changes in the GRN
121 connectivity) which thereby increases the number of reachable cell states (**Figure 1**). This
122 implies that for a given TF-target relationship, the modulation of the TF in a particular context or
123 time point would lead to changes in target expression (i.e. the relationship exists and is
124 functional at one time point), but the modulation of the same TF in another context or time point
125 would not lead to changes in target expression (i.e. the relationship is not functional at another
126 time point). In other words, the dynamic and noncommutative nature of regulatory networks
127 permits independent control of targets or genetic programs that would otherwise be
128 simultaneously activated with non-sequential, or combinatorial, logic (Letsou and Cai, 2016).

Such changes or shifts in network topology can arise for several reasons including the presence or absence of co-factors, the addition of epigenomic modifications, or changes in chromatin accessibility. Thus, for GRNs to more accurately model the emergence of distinct cell fates in development, they must encapsulate this dynamic behavior changing GRN topology. Moreover, because GRN topology dictates how a cell responds to perturbation, uncovering the dynamic GRN aids in understanding how the landscape of reachable cell states changes over time, which has significant implications in the quest to engineer cell fate.

For those reasons, we developed a computational GRN reconstruction tool called Epoch, which leverages single-cell transcriptomics to efficiently reconstruct dynamic network structures. Three key strategies exist at the center of Epoch: first, reconstruction is limited to dynamically expressed genes. Second, Epoch employs an optional “cross-weighting” strategy to reduce false positive interactions. Third, Epoch divides pseudotime into “epochs”, or time periods, and extracts a dynamic network and predicted top regulators influential in driving topology changes. Finally, Epoch includes a number of functionalities to aid in network analysis and comparison, including integration of the reconstructed GRN with major signaling pathways and the subsequent tracing through the GRN of shortest paths from signaling effectors toward activation or repression of target genes.

To demonstrate the utility of our tool we benchmarked Epoch’s performance against commonly used computational GRN reconstruction tools on synthetically generated data, *in vivo* mouse muscle development data, and *in vitro* directed differentiation data. We demonstrate that Epoch performs well in precision-recall analysis and in runtime comparison. We further highlight how Epoch’s stepwise-structured pipeline allows for user flexibility in adapting it to other GRN reconstruction methods.

Finally, we applied Epoch to answer open questions in gene regulation and directed differentiation. In particular, as pluripotent cells differentiate and undergo gastrulation, their transcriptomic profiles diverge, ultimately specifying and committing to distinct germ layers. Pluripotent cells undergoing *in vitro* differentiation often do so via embryoid body (EB) formation, which mimics *in vivo* gastrulation events such as primitive streak formation. Importantly, cell migration and specification *in vivo* are guided by a tightly-orchestrated combination of signals. Notably, Wnt3a, Bmp4, and Nodal concentration gradients (generated by Bmp and Wnt antagonist secretion on the anterior side of the embryo) are established early on, and are responsible for initiating primitive streak (Brennan et al., 2001; Yamamoto et al., 2004). For example, Wnt3a activates Brachyury in posterior epiblast cells, generating mesodermal cells (Perea-Gomez et al., 2002). Additionally, a number of FGFs (fibroblast growth factors) have

163 roles in coordinating events in early embryo development including the exit from pluripotency.
164 For example, primitive streak cells both synthesize and respond to FGFs, including Fgf4 and
165 Fgf8, the absence of which results in failure of cells to migrate away from the primitive streak,
166 resulting in the lack of mesodermal and endodermal tissue development and the disrupted
167 patterning of the neuroectoderm (Sun et al., 1999). The orchestration of development by
168 signaling pathways is mediated by the direct regulation of distinct transcriptional targets by
169 pathway effectors (**Figure 1**). However, signaling cascades also have non-transcriptional
170 consequences, including the alteration of epigenomic state and thus GRN topology (Fagnocchi
171 et al., 2016; Mohammad and Baylin, 2010). The extent to which signaling pathways influence
172 cell fate by altering GRN topology is unknown. To address this question, we performed scRNA-
173 seq on day 0 through day 4 *in vitro* mouse embryonic stem cell (mESC) directed differentiation
174 guided by four separate primitive streak induction treatments. We used Epoch to reconstruct
175 GRNs associated with each treatment and compared the resulting topologies.
176 Specifically, we used Epoch to explore why cells treated with different induction
177 treatments exhibited differing mesodermal fate potential, the lineage that was overall least likely
178 chosen by differentiating cells. Our analysis revealed a number of topological features affecting
179 mesodermal fate potential, including a central role for Peg3 in regulating the exit of pluripotency
180 and transition to mesodermal fate. Additionally, by integrating signal transduction pathways with
181 Epoch-reconstructed networks, we found that primitive streak induction via GSK inhibition
182 produced a network topology that allows for more effective mesodermal specification. This was
183 in direct contrast to other treatments in which network topologies more easily specified
184 endodermal fate through suppression of PI3K signaling and subsequent activation of Foxo1.
185 Indeed, there were remarkably large differences between target genes of the same TF across
186 treatments, supporting a model where activation of signaling pathways directly alters network
187 topology to influence cell fate potential. Finally, we reconstructed the dynamic GRN
188 underpinning *in vivo* gastrulation and mesoderm specification for the purposes of comparison to
189 our *in vitro* network. We identified *in vivo*-specific patterning modules that were not activated in
190 the *in vitro* network, and further identified residual neuroectoderm modules present in the *in vitro*
191 network. We believe that these results and similar analyses can be used to hone more efficient
192 differentiation of mesodermal-fated cells. Further, we expect that analogous analyses can be
193 performed to explain fate decisions in other dynamic biological processes.
194
195
196 **Results**

Epoch workflow relies on single-cell analysis techniques to infer dynamic network structures

Epoch takes as minimum input processed single-cell transcriptomic data and pseudotime or equivalent annotation from any trajectory inference method a user chooses to utilize (**Figure 2**). From here, Epoch employs its first step: limiting reconstruction to dynamically expressed genes in an effort to both focus on genes playing an active role in cell state changes, and to ensure that identified interactions are ones that can be inferred from perturbations in transcriptomic data. To accomplish this, Epoch models individual genes across pseudotime using a generalized additive model, and filters for significance. Alternatively, users have the option to employ TradeSeq (Van den Berge et al., 2020), a recently developed tool that employs a generalized additive model based on the negative binomial distribution to check for dynamic gene expression. Upon filtering the data for dynamically expressed genes, Epoch reconstructs an initial static network via a CLR-like (Context Likelihood of Relatedness) method, employing either Pearson correlation or mutual information to infer interactions (Faith et al., 2007).

In the second step, which we have termed “cross-weighting”, Epoch employs an optional network refinement step that relies on a cross-correlation-based weighting scheme. This helps to reduce false positives that may result from indirect interactions or that may represent non-logical interactions, ultimately improving precision (**Supplementary Figure 1a**). In this step, the expression profiles over pseudotime for each TF-target pair is aligned and progressively shifted to determine an average estimated offset value at which maximum correlation is achieved between the two profiles. A graded-decline weighting factor is computed based on this offset, and used to negatively weight interactions that are less likely to be true positives.

Once a static network has been inferred, Epoch extracts a dynamic network from the static network, and further identifies the top regulators driving changes in network topology and thus cell state. Specifically, this begins with Epoch breaking down pseudotime into “epochs”, or discrete time periods, based on pseudotime, cell ordering, k-means or hierarchical clustering, sliding window similarity, or user-defined assignment. With the exception of user-defined assignment, all methods of defining epochs are, to some extent, automated, with epoch definitions learned directly from the data (see Methods). From here, genes are assigned to epochs based on their activity along pseudotime (a given gene may be assigned to multiple epochs). Epoch then fractures the static network into a dynamic one, composed of “epoch networks”, representing active interactions within a particular epoch, and possible “transition networks”, describing how an epoch network transitions into a subsequent epoch network.

As Epoch was initially built with the improvement of cell fate engineering protocols in mind, we included in the Epoch framework a number of network analysis and network comparison capabilities. For example, Epoch will identify influential transcription factors within a given static or dynamic network by extracting top regulators that appear to have the most influence on network state. Specifically, Epoch will compute and rank TFs according to their PageRank (Brin and Page, 1998) in the context of their epoch networks, and will further look for TFs that simultaneously score high in betweenness and degree centralities as compared to all other TFs. Additionally, Epoch can integrate major signal transduction pathways with reconstructed networks. This can be used to determine the shortest paths through the networks from pathway effectors to functional groups of specified target genes. This allows users to identify and trace topologies capable of activating or repressing specific groups of genes.

Finally, Epoch is modularly designed such that it can be broken into individual steps and flexibly merged and used with any trajectory inference, network reconstruction, and even network refinement tools that currently exist or that may be developed in the future.

Epoch performs favorably on synthetically generated data

To assess the performance of Epoch in reconstructing static networks, we benchmarked it on synthetically generated data. We generated fifteen synthetic datasets using the Dyngen R package (Cannoodt et al., 2020). Networks were designed to encompass varying regulatory motifs and spanned 100-420 genes including 20-70 transcription factors. Synthetic single-cell datasets generated from these networks varied in size, from as low as 20 to as high as 1000 cells. We compared Epoch to the original versions of GENIE3 (Huynh-Thu et al., 2010), which is the GRN reconstruction engine of SCENIC (Aibar et al., 2017), and CLR (Faith et al., 2007) as well as variations on these methods that incorporated them within the Epoch framework. Thus, we assessed a total of 11 methods: CLR using mutual information (original CLR), CLR using Pearson correlation, CLR using mutual information with cross-weighting, CLR using Pearson correlation with cross-weighting, GENIE3 (original GENIE3), GENIE3 limited to dynamically expressed genes, GENIE3 limited to dynamically expressed genes with cross-weighting, Epoch with Pearson correlation (with and without cross-weighting), and Epoch with mutual information (with and without cross-weighting).

We reconstructed individual networks with each method for each dataset, using normalized simulation time as the pseudotemporal annotation for Epoch. To assess performance, we compared each resulting network to a set of five random networks, unique to

each reconstructed network, that were generated by permuting edge weights of targets for each transcription factor in the reconstructed network (**Figure 3a**). As a gold standard, all networks were compared against the original network used to generate the synthetic single-cell data. Based on fold improvement in area under the precision-recall curve over the random networks, all variations of Epoch outperformed original versions of CLR and GENIE3 (**Figure 3b, Supplementary Figure 1b**). Additionally, we found that Epoch using mutual information with or without cross-weighting resulted in higher fold improvement over random compared to any other method. The addition of cross-weighting improved median AUPR fold change over random for all methods. Further, limitation to dynamic genes (e.g. versions of CLR vs. corresponding versions of Epoch as well as GENIE3 vs. GENIE3 limited to dynamic genes) also improved performance. In all cases, it was apparent that key steps in the Epoch framework improved overall static reconstruction, as limiting reconstruction to dynamically expressed genes and applying the cross-weighting scheme both led to increased fold improvement in AUPR over random, demonstrating the utility of Epoch's framework.

We next compared Epoch to recently developed GRN reconstruction methods designed for single-cell data. We used the benchmarking platform, BEELINE (Pratapa et al., 2020), to assess Epoch's performance against 11 other single-cell methods across the synthetic datasets available within the tool (**Figure 3c, Supplementary Figure 2**). Importantly, these covered a range of cell state trajectories (linear, long linear, bifurcating, bifurcating converging, cycle) as well as dataset sizes (100 to 5000 cells). Our results demonstrate that Epoch with cross-weighting (using either mutual information or Pearson correlation) performed best based on AUPR. Additionally, while SINCERITIES almost approaches Epoch's performance at the 5000-cell dataset size, it performs markedly worse with smaller datasets, unlike Epoch. Finally, additional comparison of computational runtimes demonstrated that Epoch has the additional benefit of running magnitudes more efficiently than other methods including GRNBOOST2, PIDC, and GENIE3 (**Supplementary Figure 3**).

We then compared Epoch against the same 11 single-cell GRN reconstruction methods across the curated datasets available in BEELINE (**Supplementary Figure 4**). Importantly these datasets, though synthetic, were simulated from literature-derived networks and pseudotime was computed using Slingshot (Street et al., 2018). In this case performance based on AUPR was more equal across the methods, with GENIE3, GRNBoost2, and PIDC slightly out-performing other methods (**Supplementary Figure 4a**). On closer inspection, it was clear that performance was dataset dependent. For example, Epoch and other pseudotime-based methods performed relatively better in reconstructing the GSD network vs the HSC network

298 (**Supplementary Figure 4b,c**). The same phenomenon was present in the BEELINE
299 publication where it was initially attributed to imprecision of trajectory inference in estimating
300 pseudotime. To test this, we used the underlying literature derived-networks and re-simulated
301 the datasets. We then used the true simulation time, rather than Slingshot-derived pseudotime,
302 for reconstruction and benchmarking. Our results demonstrated that despite using the true
303 simulation time, AUPR of pseudotime-based reconstruction methods was largely unchanged,
304 suggesting that poor pseudotime computation was not at fault (**Supplementary Figure 4d**).
305 Finally, we hypothesized that decreased performance in the pseudotime-based methods
306 was largely driven by reconstruction on split trajectories. Namely, for pseudotime-based
307 methods, reconstruction of branched data was performed along each lineage separately and
308 resulting networks were aggregated. For example, HSC datasets represented four distinct
309 lineages (branches), and so the 2000 cell dataset was broken into roughly four 500 cell datasets
310 for reconstruction by pseudotime-based methods before aggregation. For non-pseudotime-
311 based methods, including GENIE3, GRNBoost2, and PIDC, reconstruction was done on the full
312 2000 cell dataset. To test the extent to which this impacted performance, we re-benchmarked
313 GENIE3, GRNBoost2, and PIDC splitting the reconstruction along each lineage before
314 aggregating, mirroring the pseudotime-based methods. The resulting performance was
315 substantially decreased, suggesting that splitting reconstruction is a factor contributing to
316 decreased performance (**Supplementary Figure 4e**). Ultimately, other factors, such as network
317 density and the presence of specific connectivity motifs, warrant further exploration, but was
318 unfortunately infeasible with the limited data.
319
320 *Epoch performs favorably on real world data*
321
322 While the results from assessment of networks reconstructed from synthetic data
323 demonstrated Epoch's favorable performance as a network inference tool, we acknowledge that
324 there are caveats associated with synthetic data, including limited stochasticity and reliance on
325 simulations that may not encompass the full extent of potential cell state responses seen in real
326 biological systems. Thus, we next turned our attention to benchmarking on real world data. To
327 assess Epoch's performance, we began by assessing the networks reconstructed by the
328 variations of Epoch, CLR and GENIE3 listed above from data of E12.5 mouse muscle
329 development (**Figure 3d**). For this dataset, we used Diffusion based pseudotime (DPT) to
330 compute pseudotime for Epoch reconstruction (Haghverdi et al., 2016). We used Chip-X data
331 from the Enrichr database, which includes ChIP-Seq, ChIP-ChIP, ChIP-PET, DamID used to

332 profile transcription factor binding to DNA, covering 220 TFs and >35,000 genes, as a gold
333 standard network (Lachmann et al., 2010). Based on precision recall, we found that all
334 variations of Epoch once again outperformed original versions of CLR and GENIE3.
335 Interestingly, we found that the two variations of GENIE3 embedded within the Epoch
336 framework performed best overall in this assessment, followed by the two variations of Epoch
337 using mutual information (with and without cross-weighting). It was again apparent that limiting
338 reconstruction to dynamically expressed genes and cross-weighting significantly improved
339 overall reconstruction (**Figure 3f, Supplementary Figure 1c**).
340 To determine if these results were consistent across other real world datasets, we turned
341 to single-cell transcriptomic data collected from day 4 in vitro mESC directed differentiation
342 (Spangler et al., 2018). We limited our reconstruction to cells in earlier stages of differentiation
343 that had not yet transitioned into any committed germ layer-like state, as determined by
344 pseudotemporal analysis, RNA velocity analysis, expression of Zfp42, marking naive pluripotent
345 cells, and expression of Fgf5, marking cells in a primed state (**Supplementary Figure 1d**). The
346 filtering ensured the trajectory remained linear, which, while absolutely not a requirement for
347 Epoch reconstruction, was employed to minimize performance variability of trajectory inference
348 methods in which branched structures may be more difficult to order. This allowed us to narrow
349 our focus on reconstruction performance while minimizing impact from potentially inaccurate
350 pseudotemporal ordering. Based on precision-recall, we found that Epoch variations using
351 cross-weighting performed best, followed by GENIE3 embedded within the Epoch framework
352 (**Supplementary Figure 1e**). Overall, these benchmarking results demonstrate Epoch's utility
353 as a reconstruction tool, and further demonstrate the usefulness of Epoch as a flexible
354 framework that can improve reconstruction of other methods.
355
356 *Single cell RNA-sequencing of early in vitro mouse ESC directed differentiation*
357
358 With the goal of exploring the dynamic GRN topology underlying lineage specification in
359 gastrulation, we collected scRNA-seq data from day 0 through day 4 *in vitro* mESC directed
360 differentiation guided by four separate treatments encouraging primitive streak formation
361 (**Figure 4a**). Briefly, cells were allowed to differentiate in serum-free differentiation media before
362 being treated with one of four treatments on day 2: Wnt3a and Activin A alone (WA), or with one
363 of Bmp4 (WAB), GSK inhibitor (WAG), or Noggin (WAN). Multiple rounds of differentiation were
364 staggered such that we could harvest samples representative of d0-d4 at one time for
365 sequencing using the MULTI-seq protocol (McGinnis et al., 2019). After barcode classification,

366 samples were preprocessed using the SCANPY pipeline (Wolf et al., 2018), and RNA velocity
367 analysis was performed (Bergen et al., 2019; La Manno et al., 2018) (**Figure 4b,c**).
368 We found the presence of three distinct lineages, which we confirmed to be
369 representative of neuroectoderm (lineage expressing Sox1), mesoderm (lineage expressing
370 Mesp1), and endoderm (lineage expressing Foxa2) based on gene expression and further
371 verified by singleCellNet (SCN) analysis (Tan and Cahan, 2019) (**Figure 4d, Supplementary**
372 **Figure 5, 6a**). RNA velocity additionally supported our cluster annotations. We found that the
373 majority of the differentiating cells transitioned toward the neuroectoderm (clusters labeled 0,2,
374 0,3, 4, 2, 5, 9) fate with smaller populations transitioning toward mesoderm (cluster labeled 8)
375 and endoderm fate (clusters labeled 7,1 and 7,0).
376 Undifferentiated cells populated cluster 1, which was positive for Zfp42 expression, a
377 pluripotency marker (Rogers et al., 1991). This population additionally classified as inner cell
378 mass, further supporting their pluripotent annotation. RNA velocity indicated these cells
379 transitioned into cluster 3, which marked the beginning of Fgf5 expression, an epiblast maker
380 (Haub and Goldfarb, 1991; Pelton et al., 2002). SCN revealed early ectoderm and epiblast
381 signature for cluster 3, indicating to us that it was representative of a primed cell state. Cells in
382 this cluster transitioned to cluster 0 and 0,4. Cells in cluster 0 were largely representative of
383 primitive streak, as determined by Brachyury expression, with some early ectoderm and residual
384 epiblast signature, as determined by SCN. Interestingly, cluster 0,4, which expressed a lower
385 level of Brachyury and exhibited some primitive streak and early ectoderm SCN signature, was
386 comprised of day 0 cells. It is possible that these cells, which had yet to undergo the
387 differentiation protocol, had escaped LIF-controlled naïve pluripotency and were already in a
388 primed early ectodermal state.
389 Cluster 0 cells expressing Mixl1, a regulator of mesoderm and endoderm (Hart et al.,
390 2002) further branched into two distinct lineages according to RNA velocity: mesoderm (cluster
391 8) and endoderm (clusters 7,1 and 7,0). Cluster 8 was largely enriched for Mesp1, and some
392 cells at later time (determined by RNA velocity) in this cluster also expressed Tbx6. SCN
393 analysis revealed that this cluster exhibited multiple mesoderm-related signatures including
394 primitive streak, anterior paraxial mesoderm, presomitic mesoderm, and somites, ultimately
395 supporting its mesoderm annotation. Along the endoderm path, cluster 7,1 transitioned from
396 cluster 0 and further transitioned into cluster 7,0. Both 7,1 and 7,0 are enriched for Foxa2 and
397 Sox17 expression. SCN analysis suggested an increasing endodermal signature down this
398 path, with cluster 7,1 classifying as anterior primitive streak and weaker as definitive endoderm
399 and gut endoderm, while cluster 7,0 more strongly classified as definitive and gut endoderm.

The neuroectodermal path begins from both cluster 0 and 0,4 according to RNA velocity results. We annotated clusters 0,3 and 4 as neuromesodermal progenitor (NMP) populations. SCN further verified cluster 0,3, which expresses T and Sox2, as early NMP and cluster 4, which expresses Sox2 and exhibits variable T expression, as late NMP. Cluster 7,2, which expresses Chordin, classified strongly as node. Interestingly, RNA velocity suggested the existence of two parallel paths along the neuroectodermal lineage, with cluster 0,2 transitioning into cluster 5, and cluster 4 transitioning into cluster 2. Along the first path, cluster 0,2, classified weakly as a number of ectodermal cell types including early ectoderm. Because RNA velocity indicated this cluster transitioned into the later neuroectoderm cluster 5, we annotated it as early ectoderm. Cluster 5 classified strongly as forebrain/midbrain, with some weaker future spinal cord classification. Given this, and it's Zic1 and En2 expression, we annotated this cluster as future brain. Cluster 9, which expresses Crabp1 and differentially expresses Tubb3 (suggesting a later neuronal identity compared to cluster 2 or 5), seems to transition from this cluster, and is thus annotated as future brain. Along the second neuroectodermal path, cells in cluster 2 classified more strongly as future spinal cord with a weaker forebrain/midbrain classification. Importantly this cluster expresses many patterning genes from the Hox family indicative of spinal cord fated cells, including Hoxd9 and Hoxb6 (Philippidou and Dasen, 2013). For this reason, we annotated this cluster as future spinal cord. A summary of our cluster labels can be found in the supplementary materials (**Supplementary Table 1**).

Interestingly, in annotating the data, it is apparent that there are differences between induction treatments in terms of the distribution of cells amongst the different populations (**Figure 4e,f, Supplementary Figure 6b**). Notably, cells treated with WAG exhibited a stunted trajectory toward neuroectodermal fate but a fuller trajectory toward mesodermal fate. This was in direct contrast to cells treated with the remaining three treatments (WAB, WAN, WA), in which very few cells differentiated toward mesodermal fate, but instead exhibited strong neuroectodermal or endodermal commitment. Further, while WAB and WA cells tended to transition into cluster 7,0 (furthest along endodermal development), WAN and WAG cells were more likely to stay in cluster 7,1.

Epoch elucidates regulatory networks driving lineage specification in early in vitro mouse ESC differentiation

To begin our network analysis exploring lineage specification, we applied Epoch to the day 0 through day 4 directed differentiation data, using latent time (Bergen et al., 2020) to order

434 cells, and reconstructing the networks underlying each of the three lineages. Latent time was
435 divided into three epochs, and a dynamic network was extracted for each lineage (**Figure 5,**
436 **Supplementary Figure 7**). In examining the Epoch-predicted top regulators and their top
437 targets, we observed noteworthy regulatory programs emerging over time along the three
438 lineages. For example, a module including the genes Gsc, Lhx1, Sox17, Foxa1, Foxa2, and
439 Gata6 emerges in the third epoch along the endoderm path. Sox17 and Foxa2 serve as
440 endoderm markers, as knockout of Sox17 has been shown to deplete definitive gut endoderm
441 and lack of Foxa2 results in failure to develop fore- and midgut endoderm (Dufort et al., 1998;
442 Kanai-Azuma et al., 2002). Foxa1 has also been implicated in the initiation and maintenance of
443 the endodermal lineage (Ang et al., 1993), while inactivation of Lhx1, which has been shown to
444 bind to the enhancer region of Foxa2, disrupts the development of definitive endoderm (Costello
445 et al., 2015). The regulator Sox11 and a collection of Hox genes emerge in the third epoch of
446 the neuroectoderm lineage, suggesting the activation of programs that pattern brain and spinal
447 cord (Philippidou and Dasen, 2013). Ultimately, these networks served as a foundation for the
448 remainder of the analyses in this study, representing TF-target regulation present along each
449 path of lineage specification.
450 In addition to directly extracting top regulators via PageRank and Betweenness-Degree
451 from the reconstructed lineage networks, we highlight a more nuanced methodology to resolve
452 influential TFs based on bagging, since the consensus of many reconstructed networks would
453 be less susceptible to noise. Specifically, we limited our scope to early time, corresponding to a
454 naïve to primed pluripotency transition, and bootstrapped the network reconstruction
455 (**Supplementary Figure 8**). For each of these sampled and reconstructed networks, we
456 predicted the top 10 regulators involved in the transition by both PageRank and Betweenness-
457 Degree. We then applied a consensus approach in which regulators were ranked by their
458 frequency as a top 10 regulator (based on PageRank) or average importance (based on
459 Betweenness-Degree) amongst the bootstrapped networks. The top regulators recovered by
460 both PageRank and Betweenness-Degree were largely overlapping, and included TFs such as
461 Zfp42, Klf2, Sox11, Pou3f1, and Klf4.
462 Of the top 10 regulators predicted through this consensus approach, Klf2 and Klf4 are
463 critical in maintaining ground state pluripotency (Yeo et al., 2014). For example, it has been
464 demonstrated that nuclear export of Klf4 causes rapid decline in Klf4 transcription, a trigger that
465 leads to the exit of naïve pluripotency, and the blocking of which prevents ESC differentiation
466 (Dhaliwal et al., 2018). Thus, it is unsurprising that they are predicted to have an influential role
467 in dictating network topology. Interestingly, a number of predicted top regulators, such as

468 Pou3f1 and Sox11, are known to promote neural fate (Barral et al., 2019; Wang et al., 2013;
469 Zhu et al., 2014). Knockdown of another predicted top regulator, Tcea3, has also been shown to
470 bias differentiation toward mesendodermal fates (Park et al., 2013). Taken together, this
471 suggests that the underlying network is primed for the neuroectodermal specification fate
472 choice, aligning with the default model of neural induction in mESCs (Muñoz-Sanjuán and
473 Brivanlou, 2002; Tropepe et al., 2001) and the apparent preference for neuroectoderm fate
474 amongst cells in this dataset.
475
476 *Peg3 is a central regulator in mesodermal WAG networks and may drive differences in gene*
477 *module expression amongst treatments*
478
479 We next focused our attention on mesodermal fate specification in mESC directed
480 differentiation. Specifically, in observing both the scarcity of the mesodermal population (in
481 comparison to neuroectodermal fate) as well as the discrepancy amongst treatments in
482 propensity for reaching mesodermal fate, we asked why WAG treated cells had the greatest
483 potential for reaching this population. We hypothesized that underlying these differences in fate
484 potential amongst treatments were treatment-specific GRNs. To this end, we reconstructed and
485 compared dynamic networks for each treatment along the mesodermal path (which we refer to
486 as the treatment-specific networks: WAG, WAB, WAN, and WA networks), and further
487 compared these against the full reconstructed mesoderm network described in the previous
488 section (which is reconstructed from all cells regardless of treatment, and which we refer to as
489 the mesoderm network). We then aimed to understand why WAG treated cells were able to
490 specify mesodermal fate to a greater extent than WAB, WAN, and WA treated cells.
491 We then sought to understand what regulators could be driving differences in mesoderm
492 reachability between the treatments. We expected treatment-driven differences in fate potential
493 to logically arise after cells undergo treatment on day 2, and would be most apparent toward
494 later latent time. We also reasoned that we could quantify and monitor differences in cell state
495 based on the activity of gene modules, defined as a community or unit of nodes that are highly
496 interconnected, within the network. Specifically, understanding the activity of these modules in
497 each treatment group would elucidate the extent to which the mesoderm state is established
498 and further aid in identifying regulators that fail to activate these regulatory programs. Thus, we
499 performed community detection on epoch 2, epoch 3, and their transition, of the mesoderm
500 network and identified distinct TF communities, or modules, within the topology (**Figure 6a,**
501 **Supplementary Figure 10**). We assessed the activity of each module by looking at the average

502 expression of member genes across latent time for each treatment (members predicted to be
503 repressed were not included in the average so as not to improperly depress this measure of
504 activity) (**Figure 6b, Supplementary Figure 11a**). Importantly, we found the existence of
505 certain modules that were strongly activated in the WAG treatment that failed to activate or were
506 weakly activated in the remaining three treatments. Three such modules (one activated in each
507 of the second epoch, third epoch, and transition) were particularly interesting as they exhibited
508 strong activity in the WAG treatment along not only the mesoderm path, but also the full dataset.
509 The TFs in these modules were Peg3, Lhx1, Hoxb2, Foxc1, Tshz1, Meis2, Mesp1, Tbx6, Foxc2,
510 Prrx2, Meox1, and Notch1. Upon extracting the differential network (which we define as the
511 network containing the interactions, or edges, that have large weight differences between two
512 treatments, and thus represent interactions most likely to be unique to a treatment network; see
513 methods) between WAG and WA, we recovered the same modules and further identified the top
514 differential regulators of these TFs themselves (**Figure 6c, Supplementary Figure 11c**).
515 Interestingly, in contrast to the WAG treatment, Peg3 was predicted to have a negligible role in
516 the WA treatment.
517 Peg3's central influence in the WAG network, however, implied a pathway linking GSK3
518 inhibition, Peg3 expression, and mesodermal gene expression. Indeed, previous reports have
519 demonstrated a role for GSK3 in maintaining DNA methylation at imprinted loci, including Peg3,
520 in mESCs (Meredith et al., 2015). Additional literature has demonstrated that methylation at
521 imprinted loci may be maintained by Dnmt3a2, which has been suggested to be regulated by
522 the GSK3-dependent transcription factor N-Myc (Popkie et al., 2010). Unfortunately, our data
523 was only able to capture Dnmt3a dynamics (representing composite Dnmt3a and Dnmt3a2
524 expression), and not specifically Dnmt3a2, which is transcribed from an alternative promoter
525 within the Dnmt3a locus. However, since Dnmt3a2 is the predominant isoform in ESCs (Chen et
526 al., 2002), we roughly compared Dnmt3a temporal dynamics and Peg3 expression between the
527 different treatments (**Supplementary Figure 11b**). Notably, Dnmt3a and Peg3 expression were
528 largely mutually exclusive, and there was low-to-no Dnmt3a expression in the WAG treated
529 cells. We then asked if this phenomenon occurs in *in vivo* gastrulation. In the single-cell mouse
530 gastrulation dataset from Grosswendt et al. (Grosswendt et al., 2020), we found relatively high
531 expression of Dnmt3a in epiblast cells which was tapered in primitive streak and mesodermal
532 cells (**Figure 6d**). In contrast, Peg3 expression was low in epiblast and increased in the
533 primitive streak, mirroring our *in vitro* data, and suggesting that Peg3 may have a role in
534 orchestrating the exit of pluripotency and specification of mesodermal fate *in vivo*.
535

536 *Tracing signaling cascades to germ layer transcriptional programs*
537
538 We next sought to trace pathways from signaling effectors to the activation of
539 mesodermal fate. To determine which signal transduction pathways were active at any given
540 point in latent time along the mesodermal lineage, we used ChIP-seq data from ChIP-Atlas (Oki
541 et al., 2018) to compile a list of binding targets for 18 signaling effector TFs (available as part of
542 the Epoch framework). We then computed average expression of these targets across latent
543 time broken down by treatment, and unsurprisingly found differences in the signaling pathways
544 that were activated in each treatment (**Figure 7a**). Of note, Notch signaling was activated in
545 WAB, WAN, and WA treatments, but not in the WAG treatment along the mesodermal lineage
546 (and weakly activated along the neuroectodermal lineage), consistent with literature
547 demonstrating that Notch signaling plays a role in specifying neuroectodermal fate in the
548 neuroectoderm-mesendoderm fate decision (Androutsellis-Theotokis et al., 2006; Aubert et al.,
549 2002).
550 Because Wnt signaling is essential for mesodermal fate, we looked for paths connecting
551 Wnt effectors to the TFs in the WAG-specific modules defined previously. Specifically, we
552 computed the shortest paths from targets of these effectors to the module TFs in each
553 treatment-specific dynamic network (using edge lengths inversely proportional to the cross-
554 weighted score) (**Figure 7b**). Paths were assigned infinite length if such a path did not exist. We
555 normalized these path lengths against the average path length in a given network, and found
556 that for the WAB, WAN, and WA treatments, no paths from Wnt to many of the module TFs
557 existed.
558 Our signaling effector target analysis also revealed increased Foxo1 activity in WAB,
559 WAN, and WA treated cells as compared to WAG treated cells, indicating the suppression of
560 PI3K signaling along the WAB, WAN, and WA trajectories (**Figure 7a**). Importantly, it is known
561 that the establishment of definitive endoderm (DE) requires suppression of PI3K signaling
562 (McLean et al., 2007; Yu et al., 2015). Further, it has been recently shown in hiPSC to DE
563 differentiation that Foxo1 binds to DE-formation-related genes and that inhibition of Foxo1
564 during DE induction impedes DE establishment (Nord et al., 2020). We therefore hypothesized
565 that a second fate choice between mesodermal and endodermal fates further exacerbated the
566 uneven mesodermal fate preference between the treatments. Indeed, our analysis indicates that
567 in the mesodermal-endodermal fate choice, the majority of WAG treated cells differentiate
568 toward mesodermal fate. This is in contrast to the WAN and WA treatment in which cells

569 preferentially differentiate toward definitive endoderm. WAB treated cells exhibited mixed
570 potential, and split roughly equally along the two paths.
571 We sought to elucidate a possible explanation for Foxo1's role in this fate choice by
572 searching for the shortest paths toward a set of endodermal genes. Specifically, similar to the
573 previous mesodermal analysis, we applied community detection to the full endodermal network
574 and identified the cluster containing Sox17 and Foxa2, known master regulators of endodermal
575 fate (**Figure 7c**). This cluster included the transcription factors Sox17, Foxa2, Bmp2, Cited1,
576 Foxa1, Gata6, Hhex, Lhx1, and Tcf7l2. For each treatment-specific network, we computed the
577 shortest paths from Foxo1 targets (as determined in the same manner as the previous Wnt
578 analysis) to these genes (**Figure 7d**). Importantly, we found that many of these regulators,
579 including both Sox17 and Foxa2, were not reachable from Foxo1 in the WAG network,
580 consistent with the observation that WAG treated cells preferentially differentiated toward
581 mesodermal fate over endodermal fate. Interestingly, Foxa2 was not reachable in the WAN
582 network, though Sox17 was. We believe this may explain the differences in distribution of cells
583 between the endodermal clusters 7,1 and 7,0. Namely, of the cells that specify endodermal fate,
584 WA and WAB treated cells more fully transitioned into cluster 7,0. In contrast, WAN treated cells
585 remained mostly in cluster 7,1 and were less likely to differentiate further into 7,0. Previous
586 studies in directed differentiation of human ESCs toward DE have implicated Sox17's regulatory
587 role in establishing DE to be upstream of Foxa2, the loss of which impairs foregut and
588 subsequent hepatic endoderm differentiation (Genga et al., 2019). This is consistent with our
589 cell type annotations of cluster 7,1 (definitive endoderm) and 7,0 (gut endoderm), and offers a
590 possible mechanism of the discrepancy in cell fate preferences between treatments. Taken
591 together, these results demonstrate that WAB, WAN, and WA networks do not allow for
592 activation of mesoderm programs from their cognate effectors, but instead assume topologies
593 that are preferential for endodermal fate, implying profound structural changes in the networks
594 that underlie the treatment-specific differences we see in cell fate. Further, this analysis
595 provides a basis for identifying which signaling pathways must be targeted for directing certain
596 fate transitions, for example through an exhaustive search of effector targets.
597
598 *Target gene differences amongst TFs confirm network topology restructuring dependent on*
599 *treatment*
600
601 Given the apparent restructuring of GRN topology upon modulation of signaling activity,
602 we aimed to understand the extent to which broad, network-wide topology changes were

603 responsible for differences in cell fate potential between treatments. To answer this, we
604 performed two distinct analyses focusing on differences in targets of transcription factors across
605 the four treatment networks.
606 First, we asked if transcription factors actively expressed in all four treatments regulated
607 the same set of target genes. To this end, we focused on the treatment-specific networks along
608 the mesodermal path. We narrowed our analysis to the 72 TFs that were active in all four
609 treatments during day 3 or day 4 along the mesodermal path. We quantified overlap between
610 targets of each TF in a pairwise comparison of the treatments using the Jaccard similarity
611 (**Figure 8a**). As a baseline, we implemented a bootstrapping method in which we reconstructed
612 10 networks for each treatment along the mesodermal path (using 400 sampled cells each); for
613 each TF we calculated the average Jaccard similarity of its targets amongst pairwise
614 comparisons of the reconstructed networks in a treatment. This gave us a baseline, or
615 expected, Jaccard similarity for each TF in each treatment. Overall, we found that
616 overwhelmingly, target differences between treatments were significantly greater than the
617 baselines, indicating vast network topology differences amongst the treatment networks.
618 Next, we asked if these differences in predicted targets had functional consequences in
619 impacting fate potential. To this end, we focused on the 13 TFs amongst the 72 mentioned
620 above that exhibited the largest differences in predicted targets between treatments (**Figure**
621 **8b**). For each treatment, we performed gene set enrichment analysis on the predicted targets of
622 these TFs (**Figure 8c**). Interestingly, we found enrichment for heart development and
623 mesoderm formation in only the WAG treatment, despite the fact that the networks we analyzed
624 were reconstructed along the mesodermal path. Of note, all treatments showed enrichment for
625 embryonic digestive tract morphogenesis. Importantly, prior literature has indeed hinted at
626 environment-based differences in fate potential. For example, in uncovering the regulatory
627 structure underpinning naïve pluripotency in mESCs, the effect of Esrrb/Nanog double
628 knockdown was shown to be dependent solely on culture environment with self-renewal
629 impeded in the presence of 2i alone, but not in the presence of both 2i and LIF (Dunn et al.,
630 2014). Taken together, these results support our hypothesis that manipulating signaling activity
631 results in a topological restructuring of the GRN, ultimately guiding cell fate potential.
632
633 *Patterning programs and residual neuroectoderm programs drive differences between in vivo*
634 *and in vitro gastrulation and mesoderm specification*
635

636 Finally, we aimed to understand the extent to which our *in vitro* mESC-derived
637 mesodermal cells established a GRN resembling that of their *in vivo* counterparts. To this end,
638 we turned to a mouse gastrulation dataset from Grosswendt et al., and sampled 250 cells from
639 each of four annotated populations that corresponded to our *in vitro* mesoderm lineage
640 populations: “Epiblast”, “Primitive streak early”, “Primitive streak late”, and “Mesoderm
641 presomitic”. We then used Epoch to reconstruct an *in vivo* dynamic network from this sampled
642 data. After reconstruction, we extracted the top regulators in each epoch by both PageRank and
643 Betweenness-Degree (**Figure 9a**). Interestingly, there was substantial difference between the
644 top regulators of the *in vivo* and *in vitro* networks, suggesting broader topology differences
645 between the two. Despite this, some key regulators were shared, including Peg3, which ranked
646 highly in the second epoch of the *in vivo* network in both PageRank and Betweenness-Degree.
647 This further supported our earlier results implicating a role for Peg3 in orchestrating the
648 pluripotent to mesodermal fate transition *in vitro* and *in vivo*.
649 Of the 22 unique TFs in the second and third epochs of our top regulator lists, at least 17
650 have known roles in guiding exit from pluripotency, mesoderm specification, or somitogenesis.
651 In particular, a number of top regulators in the second epoch are required for guiding the exit of
652 pluripotency, such as Nr6a1 and Snai1 (Galvagni et al., 2015; Gu et al., 2005). Others in this
653 epoch are components of the Wnt signaling pathway including Lef1, a Wnt effector, and Sp5,
654 which itself is directly activated by Wnt signals and further aids in activating Wnt target genes to
655 promote differentiation into multipotent mesodermal progenitors (Kennedy et al., 2016). Further,
656 TFs like brachyury and Lhx1 are necessary for primitive streak formation and normal
657 development of primitive streak-derived tissues (Shawlot et al., 1999; Wilson et al., 1995).
658 Spread across both the second and third epochs are a number TFs responsible for patterning
659 and promoting mesoderm fate. These include TFs like Hoxb1, Hoxb2, Hoxb9, Cdx1, Cdx2,
660 Mesp1, Meis2, and Id1 (Bernardo et al., 2011; Cecconi et al., 1997; Foley et al., 2019; Gouveia
661 et al., 2015; Malaguti et al., 2013; Roux et al., 2015; Takahashi et al., 2005, 2007). Of these,
662 many are also responsible for inhibiting alternative fates, such as Id1’s role in inhibiting neural
663 induction and Cdx2’s role in blocking cardiac differentiation (Mendjan et al., 2014; Zhang et al.,
664 2010). Finally, at least two TFs in the third epoch, Tbx6 and Hes7, are essential for specifying
665 and coordinating somitogenesis (Bessho et al., 2001; Chapman et al., 2003). Ultimately, the
666 predicted top regulators match well with prior literature describing the ESC to presomitic
667 mesoderm lineage trajectory from which the network was reconstructed. Additionally, this further
668 corroborates Epoch’s usefulness and ability in isolating important genes driving dynamic
669 processes.

670 We further applied the signaling cascade tracing analysis to the *in vivo* network.
671 Analogous to the *in vitro* MULTI-seq network, we looked for paths connecting Wnt effectors to
672 the same TFs in the *in vitro* WAG-specific modules (**Figure 9b**). As expected, all of the TFs
673 were reachable. Further, Wnt activation and these target TFs were highly connected, with paths
674 existing from almost every effector to every TF, implying the existence of tight and coordinated
675 control over this mesoderm module.
676 Finally, we sought to directly compare the topological and functional differences between
677 the *in vivo* and *in vitro* mesoderm networks. Because the data originates from separate
678 experiments, to directly compare topological differences we applied a threshold to both
679 networks, keeping the top 2% of non-zero-weighted edges in each. We then extracted the
680 differential network corresponding to *in vivo*-specific interactions and the differential network
681 corresponding to *in vitro*-specific interactions (**Supplementary Figure 12**). We performed
682 community detection on both differential networks and measured the activity of each resulting
683 module by assessing the average expression of member genes across time in the *in vivo* and *in*
684 *vitro* data (**Supplementary Figure 13a,b**).
685 Of the *in vivo*-specific modules, three were not activated or were insignificantly activated
686 in the *in vitro* data, despite being strongly activated in the *in vivo* data. To understand the
687 functional consequences of this, we applied GSEA to each of these modules (**Figure 9c,**
688 **Supplementary Figure 13c**). Two of these, one from the second epoch and one from the third
689 epoch, showed enrichment for multiple pathways related to patterning and axis specification,
690 including anterior/posterior axis specification, anterior/posterior pattern specification,
691 proximal/distal pattern formation, and embryonic axis specification, amongst others. Thus, a
692 large, but not unexpected, difference between the *in vivo* and *in vitro* mesoderm is the lack of
693 activation of patterning programs in the *in vitro* ESC-derived mesodermal cells.
694 Conversely, of the *in vitro*-specific modules, we isolated those that were not activated or
695 were insignificantly activated in the *in vivo* data but strongly activated in the *in vitro* data. Within
696 the first epoch, three communities satisfied this criterion. We hypothesized that differences in
697 this early epoch could drive fate differences between the two networks at later time. GSEA on
698 these modules revealed that one was enriched for positive regulation of stem cell proliferation
699 and regulation of mRNA splicing while another was enriched for terms related to fluid shear
700 stress, DNA methylation, and male gonad development (**Supplementary Figure 14**).
701 Meanwhile, GSEA on in vitro-specific modules from the second and third epochs revealed the
702 underlying activation of neural-related programs in the *in vitro* ESC-derived mesoderm (**Figure**
703 **9c, Supplementary Figure 13d**). Most of the modules were enriched for neuroectoderm

processes such as neuroepithelial cell differentiation, noradrenergic neuron differentiation, glial cell development, spinal cord development, and forebrain neuron differentiation, amongst others. Importantly, this implies that the *in vitro* differentiated cells failed to completely inhibit the default neuroectoderm lineage and instead retained a network topology capable of activating at least portions of neuroectoderm programs. This aligns with our observation that the vast majority of the *in vitro* differentiated cells tended toward the neuroectoderm lineage, with only a small percentage escaping this fate and specifying for mesoderm. Taken together, our results suggest that to produce more faithful mesodermal cells more efficiently, emphasis should be placed preventing or disrupting network module topologies responsible for neural programs.

Discussion

Methods of inferring regulatory network structures are essential for understanding cell identity transitions, uncovering mechanisms of disease progression due to dysfunctional gene regulation, and answering other regulatory questions in biology. Unfortunately, experimental methods are unscalable and existing computational methods suffer from poor performance or high computational burden. Additionally, these approaches typically infer static networks, which do not elucidate the network topology transitions that drive dynamic processes such as differentiation. Prior work addressing this has involved utilizing a combination of bulk RNA-Seq, TF ChIP-Seq, and Pol2-ChIA-PET data, with the aim of identifying differences in GRN activity or structure at discrete experimental time points during the shift from naïve to formative pluripotency (Kim et al., 2020). However, such an approach is limited in resolution and scale due to the discrete nature of the data and the sparsity of cell type-specific ChIP-Seq data, ultimately resulting in networks centered around just a handful of TFs. Thus, an approach that relies solely on single-cell transcriptomics is an attractive solution, as single-cell trajectory inference tools are capable of organizing individual cells along a continuum, improving resolution and accounting for asynchronous processes. For those reasons, we developed a novel GRN reconstruction tool, Epoch, which leverages single-cell transcriptomics and efficiently infers dynamic network structures. We demonstrate that Epoch outperforms CLR, GENIE3, and existing single-cell GRN reconstruction tools in both synthetically generated and real-world datasets. Furthermore, Epoch's relative efficiency allows it to be easily applied iteratively for applications requiring fine-tuning of network topology or iterative simulations of changes in network structure.

Epoch's utility is additionally enhanced by its flexibility. There are no strict requirements on pseudotemporal input as we demonstrate here using synthetic simulation time, diffusion

pseudotime, and RNA velocity-based latent time. We further validate on the *in vivo* muscle development dataset that precision-recall is largely comparable for different pseudotime methods (**Supplementary Figure 1f,g**). Additionally, Epoch's workflow is structured in discrete steps allowing users to pick-and-choose as well as substitute portions of the workflow. We anticipate that this flexibility will also be useful as advances in sequencing technology, such as multi-modal methods, and analysis techniques, such as novel cell ordering or reconstruction methods, can be easily adapted into Epoch's framework. Importantly, because of single-cell transcriptomic data's inherent noisiness, we also asked if smoothing gene expression over time could alleviate noise-related drops in reconstruction performance. We compared performance between unsmoothed and kernel-smoothed data and found that the there was no significant difference (**Supplementary Figure 1h**). However, smoothing functions remain in Epoch's code to aid in cleaner visualizations of gene dynamics.

Finally, we applied Epoch to scRNA-seq data from day 0 through day 4 *in vitro* mESC directed differentiation to uncover underlying dynamic networks driving mesodermal lineage specification. Our data consisted of cells transitioning into all three germ layers, and Epoch was able to recover a number of key lineage drivers. Because our data consists of cells undergoing four different treatments (WAG, WAB, WAN, WA), we were additionally able to reconstruct treatment-specific GRNs. Our analysis uncovered significant treatment-induced topological restructuring that altered the lineage specification landscape, resulting in treatment-based differences in neuroectoderm, mesoderm, and endoderm reachability. Specifically, in direct contrast to the cells in the WAB, WAN, and WA treatment groups, the cells in the WAG treatment group had higher mesodermal fate potential, exhibited a relatively stunted neuroectodermal trajectory, and had decreased potential for endodermal fate. Importantly, we uncovered three sets of topological differences that may play a role in specifying mesodermal fate.

First, we identified a set of TF modules that were preferentially activated in WAG treated cells compared to cells undergoing the other three treatments along the mesodermal fate. Specifically, these modules encompassed the transcription factors Peg3, Lhx1, Hoxb2, Foxc1, Tshz1, Meis2, Mesp1, Tbx6, Foxc2, Prrx2, Meox1, and Notch1. Upon further analysis, we observed that the WAG network developed a topology that promoted Peg3 activity, which was predicted by Epoch to have a role in regulating a large fraction of these mesodermal TFs. This influence was again specific to WAG treated-cells, and indeed, prior studies have implicated a GSK3-dependent pathway for the epigenetic regulation of imprinted loci including Peg3 (Meredith et al., 2015). Peg3 expression has been detected in early somites and other

772 mesodermal tissues (Kuroiwa et al., 1996). Interestingly, it has been separately demonstrated
773 that knockdown of Peg3 in mouse embryonic fibroblasts and neural stem cells increases
774 expression of pluripotency genes and enhances overall reprogramming efficiency (Theka et al.,
775 2017). Taken together these results suggest a role for Peg3 in modulating the exit of
776 pluripotency and mesodermal lineage specification. If so, this finding could paint Peg3 as a
777 highly enticing transcription factor to target with the goal of improving efficiency of directed
778 differentiation protocols toward certain mesodermal fates such as somites.
779 Next, we compared topological differences in the treatment-specific networks by
780 examining the existence of, and computing the length of, shortest paths. Specifically, we sought
781 to trace paths from signaling effectors to the activation of mesodermal genes within these
782 dynamic networks, thereby providing possible mechanisms of how signal transduction pathways
783 not only directly regulate targets corresponding to distinct genetic programs, but also restructure
784 network topology to alter accessibility to targets, which hones the capacity and potential for
785 distinct fates. A number of studies have pointed to the influence of "Wntch" signaling on the
786 neuroectoderm-mesendoderm cell fate decision in gastrulation (Hayward et al., 2008). Our data
787 was consistent with these reports: WAB, WAN, WA treated cells exhibited activated Notch
788 pathways and exhibited full trajectories toward neuroectoderm fate; WAG treated cells exhibited
789 markedly diminished or non-existent Notch signaling and reached mesodermal fates while
790 seemingly displaying a stunted capacity for neuroectodermal fate. Beyond this, we
791 demonstrated that WAG treated cells established a GRN topology that allowed for Wnt-
792 dependent mesoderm specification. Specifically, our analysis indicated the existence of paths
793 from Wnt signaling effectors to the aforementioned mesodermal TFs within the WAG network.
794 Analogous paths were markedly sparser in WAB, WAN, and WA networks, and some
795 mesodermal TFs were entirely unreachable from Wnt effectors. This further supported our
796 hypothesis that signaling-induced topological differences altered the cell fate landscape,
797 resulting in distinct propensities for specific fates, though the nature of the emergence of these
798 topological differences remains unclear. One possibility is that the network structures are
799 dynamically altered by epigenetic events initiated through the various signaling pathways
800 activated in treating the cells. We point to GSK3's reported effect over Peg3 methylation as an
801 example of such a phenomenon. Further studies to elucidate differences in chromatin
802 accessibility between mESCs undergoing directed differentiation by way of distinct treatments,
803 or activation of distinct signaling pathways, will aid in clarifying if such a mechanism is at play.
804 We then focused our analysis on cells specifying mesendoderm fate, and outlined
805 topological differences that could lead to differences in mesoderm vs. endoderm fate potential in

806 cells undergoing different treatments. We applied an analogous shortest path analysis along the
807 endodermal fated path to identify the link between suppression of PI3K signaling, subsequent
808 Foxo1 activation, and endoderm specification. We again found topological differences between
809 WAG and the remaining three treatments, with no paths from Foxo1 to essential endodermal
810 regulators such as Sox17 and Foxa2 in the WAG network, explaining the preference of these
811 cells to transition into mesodermal rather than endodermal fates. Interestingly, we found that
812 Foxa2 was not reachable in the WAN network, which was consistent with our finding that of the
813 WAN treated cells that specified endodermal fate, the majority tended to remain in earlier
814 endodermal stages based on RNA velocity. This was in contrast to WAB and WA treated cells,
815 which tended to transition more fully into a later endodermal stage, thereby explaining the
816 observed differences in mesodermal vs. endodermal fate potential between the treatments.
817 Finally, we compared the network driving *in vitro* directed differentiation toward
818 mesoderm fate against the network driving the analogous *in vivo* cell identity transition. Direct
819 comparison of the two networks based on predicted top regulators and the extraction of edge-
820 level differential networks suggested broad differences in the topologies of the established
821 networks. Importantly, community detection and GSEA revealed two major differences. First,
822 the *in vivo* network established modules related to patterning and axis specification programs
823 that were not established in the *in vitro* network. This is unsurprising given that while embryoid
824 bodies exhibit basic self-organization, they do not fully recapitulate the self-organization present
825 in *in vivo* gastrulation (ten Berge et al., 2008; Glykofrydis et al., 2021). It is further possible that
826 failing to establish these patterning modules hindered the *in vitro* cells from establishing network
827 topologies conducive for mesoderm fate (or specific downstream mesodermal fates), limiting
828 their differentiation potential. Second, the *in vitro* network retained a topology at least partially
829 favorable for neuroectoderm development, as there were multiple modules enriched for neural-
830 related processes in the *in vitro* network. This suggests that the cells undergoing *in vitro*
831 directed differentiation incompletely suppressed the neuroectoderm fate, and further
832 corroborates our observation and provides explanation for why the *in vitro* differentiating cells
833 overwhelmingly specified for the neuroectoderm path. Overall, this analysis suggests that
834 guiding cells toward a more faithful mesodermal fate at a higher rate will likely require steps to
835 disrupt formation or retention of neuroectoderm-favoring network topologies while possibly
836 promoting the establishment of patterning-related programs.
837 Our results ultimately suggest a model of differentiation that is driven by activation of
838 genetic programs, but honed by network topology changes. In other words, it is likely that the
839 signaling-induced restructuring of the GRNs alters the fate potential landscape which allows for

840 independent control of multiple genetic programs, increasing the diversity of reachable cell
841 states. In the case of our mESC directed differentiation, GRN topology clearly restricted the
842 potential of cells toward specific fates, resulting in different propensities for mesoderm,
843 endoderm, and neuroectoderm depending on treatment. Finally, while it may be the case that
844 both signaling activities described (i.e. the effector regulation of distinct targets and the
845 restructuring of network topology) occur concurrently, it is ultimately difficult to resolve their
846 relative timing.
847 We believe the single-cell directed differentiation dataset collected in this study will be a
848 useful resource for further analysis of decision-making in early gastrulation. Furthermore, the
849 methodologies presented here, available in the R package Epoch, are broadly applicable to any
850 biological question that may benefit from uncovering dynamic regulatory network structures and
851 the comparison of such networks. In particular, we can apply Epoch to understand cell fate
852 transitions and decisions at branch points in lineage trajectories, uncover key regulators driving
853 these decisions, and identify paths from the signal transduction level to the transcriptional
854 regulation level. Such an approach provides a powerful strategy to not only elucidate dynamic,
855 multi-scale processes in development, but also to identify signaling pathways to dysregulate for
856 the purposes of directing cell identity transitions *in vitro*.
857
858
859 **Acknowledgements**
860
861 We would like to thank Yuqi Tan, Ray Cheng, Eric Kernfeld, and David Johanson for helpful
862 discussions and testing Epoch code. We also thank Chris McGinnis and the Gartner Lab for
863 their help implementing the MULTI-seq protocol and for providing the required reagents. This
864 work was supported by the National Institutes of Health under grant R35GM124725 to PC and
865 by the National Science Foundation Graduate Research Fellowship under Grant No. DGE-
866 1746891 to EYS.
867
868
869 **Figure legends**
870
871 **Figure 1.** Effector activity on static and dynamic networks. Given a static GRN, manipulating
872 signaling activity may result in an effector guiding cell state via two possibilities: directly, the
873 effector may regulate a set of fate-specific genes, or indirectly, the effector may regulate a set of

874 TFs that further regulate the same fate-specific genes. Both cases result in the activation of the
875 same program. Alternatively, given a dynamic network, the state space of possible cell fates
876 increases since the result of effector activity is dependent on a changing network topology. As a
877 result, multiple sets of genetic programs may be regulated through the same signaling
878 mechanism. Further, these shifts in GRN topology maybe be induced by the signaling activity
879 itself.
880
881 **Figure 2.** Epoch workflow. Epoch relies on a three-step process to reconstruct dynamic network
882 structures: (1) extraction of dynamic genes and CLR, (2) application of cross-weighting, and (3)
883 extraction of the dynamic network.
884
885 **Figure 3.** Benchmarking Epoch. (A) Synthetic dataset generation via Dyngen, reconstruction,
886 and assessment. (B) Fold improvement in AUPR over random of three versions of Epoch
887 (Pearson, MI, and MI with cross-weighting) against CLR and GENIE3 on GRN reconstruction
888 from Dyngen-generated synthetic data; Kruskal-Wallis $p=4.26\times10^{-8}$. (C) BEELINE benchmarking
889 on synthetic data. Epoch using MI and Pearson denoted with “MI” and “P” respectively. “X”
890 indicates use of cross-weighting. Red line indicates the median AUPR of the best performing
891 method, Epoch using MI+cross-weighting on size 5000 cell datasets. Kruskal-Wallis $p<2.2\times10^{-}$
892 ^{16}. (D) Clustering and diffusion pseudotime for E12.5 muscle development data used in
893 benchmarking. (E) Runtimes for reconstruction on muscle development data. (Runtimes were
894 measured on a MacBook Pro laptop with 2.9 GHz Intel Core i7 processor, 16GB 2133 MHz
895 DDR3 of RAM). (F) Precision-recall curves for three versions of Epoch (Pearson, MI, and MI
896 with cross-weighting), CLR, and GENIE3 based on reconstruction from muscle development
897 dataset.
898
899 **Figure 4.** mESC in vitro directed differentiation. (A) Directed differentiation protocol. Cells were
900 harvested from d0 through d4 samples for MULTI-seq. (B) Clustering for MULTI-seq data. (C)
901 RNA velocity for MULTI-seq data. (D) Select marker gene expression. (E) Cell populations by
902 treatment. (F) Quantification of cell fate distribution based on treatment comparing:
903 mesendoderm vs. neuroectoderm, endoderm vs. mesoderm, cluster 7,0 vs. 7,1 along endoderm
904 fate, and cluster distribution along neuroectoderm fate.
905
906 **Figure 5.** MULTI-seq directed differentiation network reconstruction. (A) Latent time annotation
907 for MULTI-seq data. (B) Population breakdown by cluster of epoch assignment along each germ

908 layer path. (C) Reconstructed dynamic networks along mesoderm, endoderm, and
909 neuroectoderm paths, with top 5 regulators colored purple and their top targets in gray as
910 determined by PageRank. (D) Top regulators as predicted by Epoch via betweenness and
911 degree for the third epochs along each germ layer path.
912
913 **Figure 6.** Mesodermal network analysis. (A) The epoch 3 subnetwork of the mesodermal
914 dynamic network. TFs are colored by community and faded by betweenness. Blue and red
915 edges represent activating and repressive edges respectively. (B) Average community
916 expression over time by treatment along the mesodermal path. Communities shown (each row)
917 are from the epoch 2 subnetwork (yellow), transition (green), and epoch 3 subnetworks (aqua).
918 (C) The epoch 3 differential network between WAG (on) and WA (off). Interactions in this
919 network represent edges present in the WAG mesodermal network that are not present in the
920 WA mesodermal network. TFs are colored by community and faded by betweenness. Blue and
921 red edges represent activating and repressive edges respectively. (D) Peg3 and Dnmt3a
922 expression in a sampled portion of relevant cell types in gastrulation data from Grosswendt et
923 al. Peg3 ANOVA $p<2x10^{-16}$, Dnmt3a ANOVA $p<2x10^{-16}$.
924
925 **Figure 7.** Integrating signaling effectors and tracing paths to target genes. (A) Average
926 expression of targets of signaling effectors by treatment over time. Pathway and effector are
927 labeled on each row. (B) Shortest path analysis showing length of shortest paths from Wnt
928 effector targets (each row) to mesodermal target genes (each column) within treatment-specific
929 networks. Path lengths are normalized against average path length within a network. Blue and
930 red indicate paths that activate and repress the target gene respectively. If such a path does not
931 exist, it has length of infinity and is therefore white. (C) The epoch 3 subnetwork of the
932 endodermal dynamic network. TFs are colored by community and faded by betweenness. Blue
933 and red edges represent activating and repressive edges respectively. (D) Shortest path
934 analysis showing length of shortest paths from PI3K suppression (targets of Foxo1 activation)
935 (each row) to endodermal genes (each column) within treatment-specific networks. As before,
936 path lengths are normalized against average path length within a network. Blue and red indicate
937 activation and repression of the target gene respectively. If a path does not exist, it has length of
938 infinity and is therefore white.
939
940 **Figure 8.** Similarity of targets of TFs in different treatments. (A) Jaccard similarity of targets of
941 72 TFs. The targets of each TF in a treatment are compared to those in the other three

942 treatments (light blue). As a baseline (turquoise), targets of each TF in bootstrapped
943 reconstructed networks within a treatment are pairwise compared. All pairs $p<2x10^{-16}$. (B) The
944 13 TFs selected for GSEA and their average pairwise Jaccard similarity amongst the treatment-
945 specific networks. (C) Summarized results of performing GSEA on targets of TFs in B. Heatmap
946 shows rankings (top 10 shown) based on frequency a term is considered enriched amongst the
947 13 TFs (1 = most frequent enriched term).
948
949 **Figure 9.** Comparison to *in vivo* gastrulation and mesoderm specification. (A) Top regulators of
950 each epoch in the *in vivo* mesoderm network as predicted by PageRank and Betweenness-
951 Degree. (B) Shortest path analysis showing length of shortest paths from Wnt effector targets
952 (each row) to mesodermal target genes (each column) in the *in vivo* network. Path lengths are
953 normalized against average path length in the network. Blue and red indicate paths that activate
954 and repress the target gene respectively. If such a path does not exist, it has length of infinity
955 and is white. (C) Top ten enriched terms for *in vivo*- and *in vitro*-specific modules based on the
956 Combined Score from Enrichr GSEA analysis.
957
958
959 **Methods**
960
961 **mESC maintenance and differentiation**
962
963 GFP-Brychyury mESC cells (Gadue et al., 2006) were maintained and differentiated through
964 day 2 of the directed differentiation protocol according to Spangler et al. (Spangler et al., 2018).
965 At day 2, four different primitive-streak induction treatments were established by adding growth
966 factors Wnt3a (25ng/mL) and Activin A (WA; 9ng/mL) along with one of the following additional
967 growth factors: Noggin (150ng/mL), Gsk inhibitor (10mM), or BMP4 (0.5ng/mL). On the day of
968 sequencing, EBs and monolayers were dissociated to a single cell suspension through the use
969 of TrypLE and 40uM cell strainers.
970
971 **Multi-Seq protocol**
972
973 We utilized the MULTI-seq sample barcoding and library preparation protocol from the McGinnis
974 lab (McGinnis et al., 2019) in order to sequence 27 samples in two 10x capture runs. In short,
975 the protocol involved tagging cell membranes with sample specific barcodes using a lipid-

976 modified oligonucleotide (LMO). The LMOs (reagents obtained from the McGinnis lab) anchor
977 into the cell membrane and allow for the attachment of a normal ssDNA oligonucleotide (MULTI-
978 Seq barcode). A unique MULTI-seq barcode was added to each sample after which, all samples
979 were pooled and sequenced as if they were one sample. An equal number of cells from each
980 sample were combined to make up the pooled samples and ensure equal representation of
981 each sample after down-stream sequencing. MULTI-Seq barcodes were used down-stream to
982 identify which cells were from which samples.
983
984 **Library preparation and sequencing**
985
986 After cells were successfully tagged and pooled, they were submitted to the sequencing core
987 facility for 10x capture and library preparation. A Truseq library preparation was performed with
988 the necessary adjustments made to accommodate the MULTI-Seq platform. Libraries were
989 sequenced on Illumina NovaSeq.
990
991 **Single-cell data processing**
992
993 Sequencing alignment to the mm10 reference genome was performed using CellRanger
994 (version 3.1), and spliced, unspliced, and ambiguous read counts were extracted using
995 Velocyto. Sample barcode classification was performed using the deMULTIplex R package
996 (https://github.com/chris-mcginnis-ucsf/MULTI-seq). Subsequent quality control filtering,
997 normalization, clustering, and differential gene expression analysis was performed using
998 Scanpy (version 1.4.5) (Wolf et al., 2018). Specifically, doublets and negatives from the sample
999 barcode classification were removed, along with 271 cells we identified as residual fibroblasts
1000 (Thy1+). Next, genes were excluded if they were detected in less than 5 cells; cells were
1001 excluded if their mitochondrial gene content exceeded 10% of their total reads or if they had
1002 fewer than 500 unique genes. This left us with 5530 cells and 17528 genes. The data was then
1003 normalized and log transformed before highly variable genes were identified (1938 genes). The
1004 data was scaled and PCA was performed. Leiden clustering was performed and visualized on a
1005 UMAP embedding. We further removed a cluster of possible dying cells expressing relatively
1006 high mitochondrial gene content and low total read count, leaving a dataset with 5228 cells and
1007 1938 variable genes. Leiden clustering was refined, and RNA velocity was computed using
1008 scvelo (version 0.2.2) (Bergen et al., 2020). Latent time was computed with scvelo, using root
1009 and end states that were computed through CellRank (version 1.0.0-rc.0). Cell type

classification was performed via SingleCellNet (Tan and Cahan, 2019), using complied embryo data for training the classifier. For the E12.5 muscle development data and day 4 early directed differentiation data, diffusion maps and diffusion pseudotime were computed through Scanpy.

Synthetic benchmarking

15 synthetic datasets were generated using the Dyngen package in R (Cannoodt et al., 2020). Specifically networks were generated with 100-420 genes (including 20-70 TFs), containing varied topological motifs, and cell trajectories were simulated over time. Simulated single-cell sequencing was performed, resulting in datasets that included up to 1000 cells. CLR was implemented with the minet package in R (Meyer et al., 2008), and GENIE3 was implemented with the GENIE3 package in R (Aibar et al., 2017; Huynh-Thu et al., 2010). Variations of these two methods were carried out using the Epoch framework. Performance (AUPR) was compared against sets of 5 random networks generated for each reconstructed network via the random permutation of edge weights across targets.

BEELINE benchmarking

The BEELINE benchmarking tool (Pratapa et al., 2020) was used to compare Epoch against the following single-cell reconstruction methods (using the pre-built Docker images from BEELINE): GENIE3, GRISLI, GRNBoost2, GRNVBEM, LEAP, PIDC, PPCOR, SCODE, SCRIBE, SINCERITIES, and SINGE. We added the four versions of Epoch into the BEELINE framework for benchmarking. The synthetic and curated datasets (including simulation time and pseudotime) on which we did the benchmarking were the same as those used in the BEELINE publication, and downloaded from https://doi.org/10.5281/zenodo.3378975. Briefly, for synthetic datasets, each trajectory type included 5 dataset sizes (100 cells, 200 cells, 500 cells, and 2000 cells), and each dataset size included 10 distinct datasets (for a total of 50 datasets for each trajectory type). Curated datasets were simulated from four literature derived networks (GSD: gonadal sex determination, HSC: hematopoietic stem cell differentiation, VSC: ventral spinal cord, mCAD: mammalian cortical area development). 10 datasets were simulated for each network at 3 different dropout levels (0%, 50%, 70%), for a total of 30 datasets per network. AUPR, early precision, and runtimes were evaluated. BoolODE (Pratapa et al., 2020) was used to re-simulate the curated datasets for the purposes of extracting the true simulation time.

1044 **Bootstrapped network reconstruction of early MULTI-seq data**

1045

1046 We isolated early latent time clusters 1 and 3 and uniformly sampled 400 cells, 10 times to
1047 reconstruct 10 networks. For each reconstructed network, we extracted top regulators by
1048 PageRank and identified TFs that were most frequently ranked in the top 10 regulators. We
1049 further computed the average normalized betweenness and average normalized degree across
1050 the 10 reconstructed networks to identify top regulators.

1051

1052 **Differential network analysis and assessment**

1053

1054 As one method of network comparison, we used a naïve edge weight-based approach to extract
1055 the most differentially weighted edges between networks. Briefly, this involves computing edge
1056 weight differences for each possible edge in the two networks. Edges are then considered
1057 "differential" and specific to a given network if the edge weight difference is greater than a given
1058 threshold (in the case of both the treatment difference analysis and the in vivo vs. in vitro
1059 comparison, this threshold was set to 2). Such an approach resulted in "differential networks"
1060 which are representative of unique topological features existing in each treatment-specific
1061 network. To assess the feasibility of this simple method in extracting real and important
1062 topological differences between networks, we first applied the same method to compare the
1063 three lineage networks in the dataset. The ground truth on which we assessed these differential
1064 networks was a set of lineage-unique "pseudo-ChIP-seq" networks we compiled similar to TF-
1065 promoter binding predictions generated by (Lu and Mar, 2020) (**Supplementary Figure 6a**). In
1066 short, TF-target interactions were acquired by mapping the PWM of a TF (Weirauch et al., 2014)
1067 to the promoter region sequence of potential target genes using the Find Individual Motif
1068 Occurrences (FIMO) software (described in more detail below). These ground truth networks
1069 were filtered for dynamically expressed genes along given paths (for lineage-specificity), and
1070 further filtered for unique edges to mimic extraction of unique topological features (lineage-
1071 unique). Using this set of networks, we compared AUPR of our path-differential networks
1072 against random networks (generated by shuffling edge weights of targets of each TF in the
1073 differential networks). On average the differential networks had a 1.7 fold improvement over
1074 random AUPR, with many comparisons falling in the 1.8-3.0 range (**Supplementary Figure 6b**).

1075

1076 **Construction of path-unique TF-target pseudo-gold standard**

1077

1078 Transcription star site (TSS) annotations were downloaded from the USCS Genome Browser
1079 (mouse GRCm38/mm10 genome assembly) (Haeussler et al., 2019). Promoter regions were
1080 defined as -750 to +250 around the TSSs. We then acquired position weight matrices (PWMs)
1081 of transcription factors from the Catalog of Inferred Sequence Binding Preferences (CIS-BP
1082 Database build version 2.00) (Weirauch et al., 2014). We used the Find Individual Motif
1083 Occurrences tool (Grant et al., 2011) to obtain potential TF-promoter binding pairs for 648 TFs.
1084 We kept all interactions for which p-value < 5 $x10^{-5}$. To generate path-unique gold standards, for
1085 each lineage (mesoderm, endoderm, neuroectoderm) we filtered interactions for dynamically
1086 expressed genes along each path as computed by Epoch. Further, when assessing the
1087 "differential network" pairwise comparisons, we filtered out interactions that were redundant
1088 between the gold standards, and only kept interactions unique to each path.
1089
1090 **Targets of TFs by treatment comparison**
1091
1092 To quantify the extent of topology differences between treatments along the mesodermal path,
1093 we performed pairwise comparison on the four treatment-specific networks and computed
1094 Jaccard similarity between predicted targets of TFs. The comparison was carried out on 72 TFs
1095 that were selected based on their active expression on day 3 or day 4 (i.e. after induction
1096 treatments). We computed baseline similarities for each TF in each treatment by bootstrapping
1097 the network reconstruction (10 network reconstructions per treatment, 400 sampled cells per
1098 network reconstruction) and averaging their pairwise Jaccard similarities. We selected the 13
1099 TFs exhibiting the greatest differences in targets amongst the treatments and performed gene
1100 set enrichment analysis using the Enrichr R package (Chen et al., 2013; Kuleshov et al., 2016)
1101 and the GO Consortium Biological Processes database (Ashburner et al., 2000; Gene Ontology
1102 Consortium, 2021) on the targets of each TF. We further filtered out terms that did not meet the
1103 criteria of adjusted p-value<0.05. Finally, we summarized the results between the 13 TFs by
1104 counting the frequency (out of 13) that a term was considered enriched and ranked the results
1105 accordingly.
1106
1107 **Comprehensive signaling effector TF targets list**
1108
1109 We acquired binding score (MACS2) data for 18 signaling effector TFs from the ChIP-Atlas (Oki
1110 et al., 2018), and processed each accordingly: target genes were ranked by maximum binding
1111 score and the top 2000 targets were retained (or all retained, if less than 2000 targets). To

compute average effector activity, target lists were filtered for those appearing in the MULTI-seq directed differentiation data, and not considered in the analysis if the effector had less than 10 targets after filtering.

In Vivo Comparison

To create a comparable in vivo dataset, 250 cells were randomly sampled from each of the following annotated populations in the Grosswendt et al. gastrulation dataset: “Primitive streak anterior”, “Endoderm”, “Ectoderm early 1”, “Ectoderm early 2”, “Epiblast”, “Fore_midbrain”, “Future spinal cord”, “Endoderm gut”, “Neural crest”, “Ectoderm neural anterior”, “Ecotderm neural posterior”, “Neuromesodermal progenitor late”, “Node”, “Notochord”, “Mesoderm pharyngeal arch”, “Mesoderm presomitic”, “Primitive streak late”, “Primitive streak early”, “Somites”, “Neuromesodermal progenitor early.” The resulting dataset spanned E6.5 to E8.5. Quality control filtering, normalization, and Diffusion Pseudotime trajectory inference was performed using Scanpy (version 1.4.5) (Wolf et al., 2018), analogous to the processing of the MULTI-Seq data described above. Further comparison was limited to the mesodermal lineage – this included populations labeled “Epiblast”, “Primitive streak early”, “Primitive streak late”, and “Mesoderm presomitic”.

Epoch was employed to reconstruct the in vivo dynamic network corresponding to this data. To compare the *in vivo* network to the *in vitro* network, both networks were thresholded such that the top 2% of non-zero edges were kept. Network comparison including differential network extraction and community detection were performed using Epoch. Average module expression was analyzed by computing mean expression of predicted activated members over time if the module included at least 8 such members (members predicted to be repressed were not included in the average so as not to improperly depress this measure of activity). GSEA was performed using the Enrichr R package (Chen et al., 2013; Kuleshov et al., 2016) and the GO Consortium Biological Processes database (Ashburner et al., 2000; Gene Ontology Consortium, 2021). Both the 2021 and 2018 versions of this database were used for enrichment analyses. Figures shown here show results using the 2021 version of this database for all enrichment analyses except for epoch3, community 3. This community was not enriched for any terms in the 2021 database, but was enriched for multiple terms in the 2018 pathway.

Epoch Workflow

Epoch takes as input processed (normalized and log-transformed) single-cell transcriptomic data and accompanying pseudotime (or equivalent) annotation. The Epoch workflow is based in three strategies: (1) the extraction of dynamically expressed genes and subsequent static reconstruction with CLR, (2) network refinement using a cross-correlation based strategy termed "cross-weighting," (3) the extraction of a dynamic network and subsequent identification of top regulators. Epoch is available as a package in R, and code and tutorials can be found at https://github.com/pcahan1/epoch.

Identification of dynamically expressed genes

Limiting network reconstruction to dynamically expressed genes serves two purposes. Importantly, it focuses the network on interactions that are more likely playing a role in the observed biological process. Second, it reduces the instances of false positive interactions and improves precision by limiting possible edges between temporally-variable genes. To select for such genes, Epoch models individual genes across the annotated pseudotime using a generalized additive model (GAM). Specifically, Epoch uses the 'gam' package (gaussian family, loess smooth pseudotime) to fit a model for each gene using the backfitting algorithm. Genes are considered dynamic based on significance of the smooth term (pseudotime). Alternatively, users can specify to find dynamic genes via TradeSeq (Van den Berge et al., 2020), a recently developed tool that identifies dynamic changes in gene expression via a GAM based on the negative binomial distribution.

CLR

The Context Likelihood of Relatedness (CLR) algorithm was first proposed in 2007 by Faith et al. as a method for inferring gene regulatory networks from expression data. In short, CLR computes the mutual information (MI) between expression levels of every potential transcription factor and target gene. From here the method scores the MI values in the context of the network by computing a z-score relying on (1) the distribution of MI values for all potential regulators of the target gene, z_i, and on (2) the distribution of MI values for all potential targets of the transcription factor, z_j:

$$z_{ij} = \sqrt{z_i^2 + z_j^2}$$

The result is a weighted adjacency matrix describing the likelihood of TF-target gene interactions that can be thresholded to derive a network structure. For Epoch, a version of CLR is applied to dynamically expressed genes to reconstruct an initial static network via the 'minet' package in R. Users can choose between implementing the MI version or a version using Pearson correlation in place of MI. In either case, Epoch at this step will return a GRN table. Each row outlines an interaction in the initial network identifying the transcription factor, target gene, correlation, and CLR-based z-score.

Cross-weighting

After inferring an initial network structure, Epoch can apply a network refinement step we call cross-weighting. The objective of this step is to negatively weight edges in the initial network that are unlikely to be true interactions, that may, for example, be representative of indirect interactions. To this end, for every TF-target pair in the initial network, Epoch computes cross-correlation across a given lag time (defaults to a fifth of total pseudotime). After ordering the lag times by decreasing correlation, Epoch computes an offset value where maximum correlation is achieved, defined by default as the top third of the ranked lag times. Finally, Epoch scores the offset values of each interaction:

$$weight = \begin{cases} 1 & x \leq w_{min} \\ 0 & x \geq w_{max} \\ -x/(w_{max} - w_{min}) + 1 & else \end{cases}$$

where the offset, x, is computed as described, and maximum and minimum windows can be altered by the user if desired. Z-scores from the initial network are weighted accordingly, ultimately filtering out false positives. Epoch, at this step will return an appended GRN table, including for each interaction, the offset value and new weighted score.

Default parameters for cross-weighting are specified within Epoch, and were chosen based on empirical improvements in performance across synthetic and real datasets (ranging in number of genes, number of cells, and simple trajectory types). For example, we found that optimal lag time varied to some extent with dataset size, with larger datasets requiring a larger lag time to catch target response to regulator expression changes (**Supplementary Figure 15a**). Smaller lag times tended to correlate with decreased AUPR, likely because the lag time was not sufficient to catch the point of maximum cross-correlation. AUPR also begins to gradually decrease at larger lag times, though this effect is much less pronounced. We found that our

default lag (set to 1/5 of the dataset size) resulted in high AUPR across various datasets. Similarly, we also examined various minimum and maximum windows, and found that our default values resulted in optimal AUPR (**Supplementary Figure 15b**) across datasets of varying sizes. However, users may want to modify these parameters to increase or decrease the leniency of the weighting for a number of reasons, such as when applying Epoch to more complex trajectories with large numbers or more complex state changes (and correspondingly, a large number of epochs). In this case, we would recommend finding optimal lag and window in an analogous method. Specifically, this would entail designing a modular network (and corresponding GRN) representative of the more complex trajectory, using this network to simulate synthetic datasets, and performing a parameter sweep to optimize reconstruction AUPR. Synthetic network design and simulation for both simple and complex trajectories can be done via platforms such as Dyngen.

Dynamic Network Extraction

Epoch will extract a dynamic network from the reconstructed static network. Specifically, the process begins by breaking pseudotime into “epochs,” or time periods. A number of options are available to users to accomplish this. Briefly, Epoch can define the epochs based on pseudotime, equal cell ordering (resulting in equal number of cells per epoch), k-means or hierarchical clustering, sliding window similarity, or user-defined manual assignment. With the exception of user-defined assignment and sliding window similarity, the number of epochs is specified by the user, and can be determined by examining the heatmap of gene expression across pseudotime and estimating the rough number of expression states represented in the data. We recommend smoothing the data to aid in heatmap visualization, which can be done through the Epoch. Alternatively, it is unnecessary to supply the number of epochs if using the similarity method, which will automatically detect epochs based on correlation between groups of cells along a sliding window across pseudotime. After epochs are defined, Epoch will assign genes to epochs, based on their activity along pseudotime. In brief, this is either based on activity (i.e. genes active in any epochs will be assigned to those epochs), or based on differential expression (i.e. genes are assigned based on if they are differentially expressed in an epoch). Specifically, if genes are assigned by activity, Epoch will compute, for each gene, a threshold against which average expression of the gene in an epoch is compared. This threshold can be modified by user input. If instead genes are assigned by differential expression, a p-value threshold is used to determine assignments. Finally, “orphan genes,”

which we define as dynamically expressed genes that do not get assigned to any epoch, are assigned to the epoch in which their average expression is maximum.
Based on these assignments, Epoch will fracture the static network into a dynamic one composed of “epoch networks” and “transition networks”. Specifically, an edge between regulator and target gene appears in an epoch network if the regulator is assigned to that epoch. Further, an edge will appear in a transition subnetwork under two conditions: (1) For an activating edge, the target is not active in the source epoch, is active in the subsequent epoch, and regulator is active or (2) For a repressive edge, the target is active in the source epoch, is not active in the subsequent epoch, and the regulator is active. Following this step, Epoch will return a dynamic network represented by a list of individual GRN tables. This includes the epoch networks or essentially the dynamic network, as well as transition networks that describe how an epoch network may transition into a subsequent epoch network.

Top Regulator Prediction

Epoch employs two graph theoretic methods to predict “top regulators,” the transcription factors that appear to have the most influence in driving changes in or maintaining topology. First, Epoch will rank regulators by weighted PageRank. In brief, the PageRank centrality measures the importance of nodes in a network based on the number and quality of links of which a node is a part. In essence, the most influential nodes are likely to interact with many influential nodes. Second, Epoch will rank regulators by the product of normalized betweenness and normalized degree. Here, the assumption is that the most influential nodes are likely to be traversed by many shortest paths (and thus have high betweenness) and interact with many other nodes (and thus have high degree). In Epoch, PageRank, betweenness, and degree centralities are implemented through the ‘igraph’ package. By default, cross-weighted edge weights are used, but can be further specified by the user. In both top regulator prediction methods Epoch will return ranked lists of nodes, and further specify their corresponding PageRank or normalized betweenness, normalized degree, and betweenness-degree product.

Supplementary materials

Supplementary Figure 1. Epoch benchmarking continued. (A) An example from GRN reconstruction on a synthetic dataset showing the difference in number of false positives based

1279 on whether or not cross-weighting is performed. (B) Full results of benchmarking reconstruction
1280 of synthetic data. Four versions of CLR (Pearson vs. MI, cross-weighting vs. no cross-
1281 weighting), four versions of Epoch (same as CLR), and three versions of GENIE3 (original,
1282 limited to dynamic genes, and with cross-weighting) are compared. Kruskal-Wallis $p=1.75x10^{-11}$.
1283 (C) Full results of benchmarking reconstruction of the muscle development data. Methods are
1284 the same as in A. (D) Early mESC directed differentiation data (subsetted from Spangler et al.
1285 2018). Zfp42 expression, Fgf5 expression, and velocity pseudotime are shown. (E) Full results
1286 of benchmarking reconstruction of the early Spangler et al. data. Methods are the same as in A.
1287 (F) Clustering, diffusion pseudotime, velocity pseudotime, and latent time of the E12.5 muscle
1288 development data. (G) Precision recall curves of four variations of Epoch using three different
1289 pseudotime annotations. (H) Effect of smoothing vs. unsmoothing on AUPR of reconstruction
1290 using various methods.
1291
1292 **Supplementary Figure 2.** BEELINE synthetic data benchmarking. AUPR of reconstruction on
1293 synthetic data using the four versions of Epoch (MI = mutual information, P = Pearson
1294 correlation, X = with cross-weighting) and 11 other single-cell GRN reconstruction tools. Results
1295 are faceted by trajectory type (LI = linear, LL = long linear, BF = bifurcating, BFC = bifurcating
1296 converging, CY = cycle) and colored by number of cells in the dataset.
1297
1298 **Supplementary Figure 3.** BEELINE synthetic data runtimes. Runtimes (in seconds) are plotted
1299 for each method, faceted by magnitude of runtime. Four versions of Epoch are shown (MI =
1300 mutual information, P = Pearson correlation, X = with cross-weighting), along with 11 other
1301 single-cell GRN reconstruction tools. Data is colored based on number of cells in the dataset.
1302
1303 **Supplementary Figure 4.** BEELINE curated data benchmarking. AUPR of reconstruction on
1304 curated data (as described in Pratapa et al. 2020), using the four versions of Epoch (MI =
1305 mutual information, P = Pearson correlation, X = with cross-weighting) and 11 other single-cell
1306 GRN reconstruction tools. Panel (A) summarizes the results from all curated datasets. Panel (B)
1307 shows results from reconstruction on the GSD datasets using BEELINE-provided Slingshot
1308 pseudotime. Panel (C) shows results from reconstruction on the HSC datasets using BEELINE-
1309 provided Slingshot pseudotime. Panel (D) shows results from reconstruction on re-simulated
1310 HSC datasets using true simulation time from BoolODE (Pratapa et al., 2020). Panel (E) shows
1311 results from reconstruction on re-simulated HSC datasets using true simulation time, comparing
1312 the results of reconstructing using GENIE3, GRNBoost2, and PIDC with no splitting vs. splitting

1313 along each lineage before compiling (SPLIT = with splitting and compiling).
1314
1315 **Supplementary Figure 5.** MULTI-seq directed differentiation cell typing. (A) timepoint,
1316 treatment, total counts, and percent mitochondrial transcripts content of the MULTI-seq data. (B)
1317 Select marker gene expression of the MULTI-seq data. (C) Differential expression analysis of
1318 the MULTI-seq data by cluster.
1319
1320 **Supplementary Figure 6.** MULTI-seq cell type classification and cluster transitions. (A)
1321 SingleCellNet classification results. The classifier was trained from mouse embryo data found in
1322 literature, curated by members in the lab. (B) Sankey diagrams depicting cluster transitions (and
1323 cell fate transition proportions) as broken down by treatment.
1324
1325 **Supplementary Figure 7.** MULTI-seq network reconstruction and top regulators. Heatmaps
1326 depicting TF expression across time and Epoch definitions along the (A) mesoderm path, (B)
1327 endoderm path, and (C) neuroectoderm path. (D) Top 10 regulators in each epoch network
1328 along each germ layer path as predicted by Epoch via PageRank.
1329
1330 **Supplementary Figure 8.** Bootstrapped top regulator prediction for inner cell mass to epiblast-
1331 like transition. (A) Workflow for bootstrapping network reconstruction in order to predict top
1332 regulators. (B) Only cells from early time were used. Clusters used and corresponding diffusion
1333 pseudotime shown here. (C) Top regulators for this early fate transition as predicted using
1334 PageRank and Betweenness-Degree.
1335
1336 **Supplementary Figure 9.** Proof of concept for differential network analysis. (A) Path-unique
1337 gold standard creation. (B) Performance (AUPR) over random of differential network in
1338 recovering path-unique gold standard edges. Each row is a comparison between two paths.
1339 Each column represents unique edges recovered for a given path. As an example, the top left
1340 box indicates that in the endoderm vs. neuroectoderm comparison, in the first epoch the
1341 endoderm differential network is 1.82 times better than a shuffled network in recovering edges
1342 that are specific to endoderm (and not present in neuroectoderm).
1343
1344 **Supplementary Figure 10.** Mesodermal network and differential networks. The left column
1345 ("Full Reconstruction") depicts the dynamic mesodermal network. The middle and right columns
1346 depict the WAG vs. WA differential network. Middle is the network unique to WAG, right is the

network unique to WA. TFs are colored by community. Blue and red edges represent activating and repressive edges respectively.

Supplementary Figure 11. Mesodermal network analysis continued. (A) Average community expression over time by treatment along the full dataset. Communities shown (each row) are from the epoch 2 subnetwork (yellow), transition (green), and epoch 3 subnetworks (aqua) of the mesodermal network. (B) Peg3 and Dnmt3a expression across time along the mesodermal path of the MULTI-seq data. (C) Top differential regulators of mesodermal genes. Blue and red represent activators and repressors respectively. Y-axis is plotting difference in edge weights between the WAG and WA networks. Thus, TFs appearing above the 0-line are more unique to the WAG network, and those below are more unique to the WA network.

Supplementary Figure 12. *In vivo* vs. *in vitro* mesodermal differential network. (Left) The differential network containing edges unique to the *in vivo* network. (Right) The differential network containing edges unique to the *in vitro* network.

Supplementary Figure 13. *In vivo* vs. *in vitro* mesodermal network comparison continued. (A) Average *in vivo* community expression over time along the mesodermal path for the *in vivo*, *in vitro* WAG, *in vitro* WAB, *in vitro* WAN, and *in vitro* WA data. (B) Average *in vitro* community expression over time along the mesodermal path for the *in vivo*, *in vitro* WAG, *in vitro* WAB, *in vitro* WAN, and *in vitro* WA data. (C) Top ten enriched terms for *in vivo*-specific modules based on the Combined Score from Enrichr GSEA analysis. The three modules included are activated in the *in vivo* data but not (or weakly activated) in the *in vitro* data (see panel A). (D) Top ten enriched terms for *in vitro*-specific modules based on the Combined Score from Enrichr GSEA analysis. The six modules included are activated in the *in vitro* data but not (or weakly activated) in the *in vivo* data (see panel B).

Supplementary Figure 14. Early functional differences in *in vitro* vs. *in vivo* networks. Enriched terms for *in vitro*-specific modules based on the Combined Score from Enrichr GSEA analysis, specific to the first epoch. These three communities belong to the first epoch and are activated in the *in vitro* data but not (or weakly activated) in the *in vivo* data (see Supplementary Figure 3b).

Supplementary Figure 15. Optimal default parameter settings for synthetic linear trajectories.

(A) Average AUPR of reconstruction using different cross-weighting lag times across datasets of varying sizes, taken from BEELINE linear datasets. Each dataset size contains 10 distinct datasets, Default lag time is plotted as the orange triangle, and is computed as one-fifth of the number of cells in the data. (B) Average AUPR of reconstruction using different minimum and maximum windows in cross-weighting. Data shown is reconstruction from BEELINE linear datasets. Each dataset size contains 10 distinct datasets. Default minimum and maximum is indicated by the triangle, and is defined as 1/50 and 1/12 of total cells respectively. High average AUPR is indicated by the darker red colors.

Supplementary Table 1. Cell type annotation by cluster.

Bibliography

Aibar, S., González-Blas, C.B., Moerman, T., Huynh-Thu, V.A., Imrichova, H., Hulselmans, G., Rambow, F., Marine, J.-C., Geurts, P., Aerts, J., et al. (2017). SCENIC: single-cell regulatory network inference and clustering. Nat. Methods *14*, 1083–1086.

Androutsellis-Theotokis, A., Leker, R.R., Soldner, F., Hoeppner, D.J., Ravin, R., Poser, S.W., Rueger, M.A., Bae, S.-K., Kittappa, R., and McKay, R.D.G. (2006). Notch signalling regulates stem cell numbers in vitro and in vivo. Nature *442*, 823–826.

Ang, S.L., Wierda, A., Wong, D., Stevens, K.A., Cascio, S., Rossant, J., and Zaret, K.S. (1993). The formation and maintenance of the definitive endoderm lineage in the mouse: involvement of HNF3/forkhead proteins. Development *119*, 1301–1315.

Ashburner, M., Ball, C.A., Blake, J.A., Botstein, D., Butler, H., Cherry, J.M., Davis, A.P., Dolinski, K., Dwight, S.S., Eppig, J.T., et al. (2000). Gene Ontology: tool for the unification of biology. Nat. Genet. *25*, 25–29.

Aubert, J., Dunstan, H., Chambers, I., and Smith, A. (2002). Functional gene screening in embryonic stem cells implicates Wnt antagonism in neural differentiation. Nat. Biotechnol. *20*, 1240–1245.

Barral, A., Rollan, I., Sanchez-Iranzo, H., Jawaid, W., Badia-Careaga, C., Menchero, S., Gomez, M.J., Torroja, C., Sanchez-Cabo, F., Göttgens, B., et al. (2019). Nanog regulates Pou3f1 expression at the exit from pluripotency during gastrulation. Biol. Open *8*.

ten Berge, D., Koole, W., Fuerer, C., Fish, M., Eroglu, E., and Nusse, R. (2008). Wnt signaling mediates self-organization and axis formation in embryoid bodies. Cell Stem Cell *3*, 508–518.

Bergen, V., Lange, M., Peidli, S., Wolf, F.A., and Theis, F.J. (2019). Generalizing RNA velocity to transient cell states through dynamical modeling. BioRxiv.

Bergen, V., Lange, M., Peidli, S., Wolf, F.A., and Theis, F.J. (2020). Generalizing RNA velocity to transient cell states through dynamical modeling. Nat. Biotechnol. *38*, 1408–1414.

Bernardo, A.S., Faial, T., Gardner, L., Niakan, K.K., Ortmann, D., Senner, C.E., Callery, E.M., Trotter, M.W., Hemberger, M., Smith, J.C., et al. (2011). BRACHYURY and CDX2 mediate BMP-induced differentiation of human and mouse pluripotent stem cells into embryonic and extraembryonic lineages. Cell Stem Cell *9*, 144–155.

di Bernardo, D., Thompson, M.J., Gardner, T.S., Chobot, S.E., Eastwood, E.L., Wojtovich, A.P., Elliott, S.J., Schaus, S.E., and Collins, J.J. (2005). Chemogenomic profiling on a genome-wide scale using reverse-engineered gene networks. Nat. Biotechnol. *23*, 377–383.

Bessho, Y., Sakata, R., Komatsu, S., Shiota, K., Yamada, S., and Kageyama, R. (2001). Dynamic expression and essential functions of Hes7 in somite segmentation. Genes Dev. *15*, 2642–2647.

Bonnaffoux, A., Herbach, U., Richard, A., Guillemin, A., Gonin-Giraud, S., Gros, P.-A., and Gandrillon, O. (2019). WASABI: a dynamic iterative framework for gene regulatory network inference. BMC Bioinformatics *20*, 220.

Brennan, J., Lu, C.C., Norris, D.P., Rodriguez, T.A., Beddington, R.S., and Robertson, E.J. (2001). Nodal signalling in the epiblast patterns the early mouse embryo. Nature *411*, 965–969.

Brin, S., and Page, L. (1998). The anatomy of a large-scale hypertextual Web search engine. Computer Networks and ISDN Systems *30*, 107–117.

Buenrostro, J.D., Giresi, P.G., Zaba, L.C., Chang, H.Y., and Greenleaf, W.J. (2013). Transposition of native chromatin for fast and sensitive epigenomic profiling of open chromatin, DNA-binding proteins and nucleosome position. Nat. Methods *10*, 1213–1218.

Cahan, P., Cacchiarelli, D., Dunn, S.-J., Hemberg, M., de Sousa Lopes, S.M.C., Morris, S.A., Rackham, O.J.L., Del Sol, A., and Wells, C.A. (2021). Computational stem cell biology: open

1441 questions and guiding principles. Cell Stem Cell *28*, 20–32.
1442 Cannoodt, R., Saelens, W., Deconinck, L., and Saeys, Y. (2020). dyngen: a multi-modal
1443 simulator for spearheading new single-cell omics analyses. BioRxiv.
1444 Carro, M.S., Lim, W.K., Alvarez, M.J., Bollo, R.J., Zhao, X., Snyder, E.Y., Sulman, E.P., Anne,
1445 S.L., Doetsch, F., Colman, H., et al. (2010). The transcriptional network for mesenchymal
1446 transformation of brain tumours. Nature *463*, 318–325.
1447 Cecconi, F., Proetzel, G., Alvarez-Bolado, G., Jay, D., and Gruss, P. (1997). Expression of
1448 Meis2, a Knotted-related murine homeobox gene, indicates a role in the differentiation of the
1449 forebrain and the somitic mesoderm. Dev. Dyn. *210*, 184–190.
1450 Chapman, D.L., Cooper-Morgan, A., Harrelson, Z., and Papaioannou, V.E. (2003). Critical role
1451 for Tbx6 in mesoderm specification in the mouse embryo. Mech. Dev. *120*, 837–847.
1452 Chen, S., and Mar, J.C. (2018). Evaluating methods of inferring gene regulatory networks
1453 highlights their lack of performance for single cell gene expression data. BMC Bioinformatics
1454 *19*, 232.
1455 Chen, E.Y., Tan, C.M., Kou, Y., Duan, Q., Wang, Z., Meirelles, G.V., Clark, N.R., and Ma'ayan,
1456 A. (2013). Enrichr: interactive and collaborative HTML5 gene list enrichment analysis tool.
1457 BMC Bioinformatics *14*, 128.
1458 Chen, J., Schlitzer, A., Chakarov, S., Ginhoux, F., and Poidinger, M. (2016). Mpath maps multi-
1459 branching single-cell trajectories revealing progenitor cell progression during development. Nat.
1460 Commun. *7*, 11988.
1461 Chen, T., Ueda, Y., Xie, S., and Li, E. (2002). A novel Dnmt3a isoform produced from an
1462 alternative promoter localizes to euchromatin and its expression correlates with active de novo
1463 methylation. J. Biol. Chem. *277*, 38746–38754.
1464 Costello, I., Nowotschin, S., Sun, X., Mould, A.W., Hadjantonakis, A.-K., Bikoff, E.K., and
1465 Robertson, E.J. (2015). Lhx1 functions together with Otx2, Foxa2, and Ldb1 to govern anterior
1466 mesendoderm, node, and midline development. Genes Dev. *29*, 2108–2122.
1467 Davidson, E.H., and Erwin, D.H. (2006). Gene regulatory networks and the evolution of animal
1468 body plans. Science *311*, 796–800.
1469 Dhaliwal, N.K., Miri, K., Davidson, S., Tamim El Jarkass, H., and Mitchell, J.A. (2018). KLF4
1470 Nuclear Export Requires ERK Activation and Initiates Exit from Naive Pluripotency. Stem Cell
1471 Rep. *10*, 1308–1323.
1472 Dufort, D., Schwartz, L., Harpal, K., and Rossant, J. (1998). The transcription factor HNF3beta
1473 is required in visceral endoderm for normal primitive streak morphogenesis. Development *125*,
1474 3015–3025.
1475 Dunn, S.J., Martello, G., Yordanov, B., Emmott, S., and Smith, A.G. (2014). Defining an
1476 essential transcription factor program for naïve pluripotency. Science *344*, 1156–1160.
1477 Fagnocchi, L., Mazzoleni, S., and Zippo, A. (2016). Integration of Signaling Pathways with the
1478 Epigenetic Machinery in the Maintenance of Stem Cells. Stem Cells Int. *2016*, 8652748.
1479 Faith, J.J., Hayete, B., Thaden, J.T., Mogno, I., Wierzbowski, J., Cottarel, G., Kasif, S., Collins,
1480 J.J., and Gardner, T.S. (2007). Large-scale mapping and validation of Escherichia coli
1481 transcriptional regulation from a compendium of expression profiles. PLoS Biol. *5*, e8.
1482 Foley, T.E., Hess, B., Savory, J.G.A., Ringuette, R., and Lohnes, D. (2019). Role of Cdx factors
1483 in early mesodermal fate decisions. Development *146*.
1484 Gadue, P., Huber, T.L., Paddison, P.J., and Keller, G.M. (2006). Wnt and TGF-beta signaling are
1485 required for the induction of an in vitro model of primitive streak formation using embryonic
1486 stem cells. Proc. Natl. Acad. Sci. USA *103*, 16806–16811.

1487 Galvagni, F., Lentucci, C., Neri, F., Dettori, D., De Clemente, C., Orlandini, M., Anselmi, F.,
1488 Rapelli, S., Grillo, M., Borghi, S., et al. (2015). Snai1 promotes ESC exit from the pluripotency
1489 by direct repression of self-renewal genes. Stem Cells *33*, 742–750.
1490 Gene Ontology Consortium (2021). The Gene Ontology resource: enriching a GOld mine.
1491 Nucleic Acids Res. *49*, D325–D334.
1492 Genga, R.M.J., Kernfeld, E.M., Parsi, K.M., Parsons, T.J., Ziller, M.J., and Maehr, R. (2019).
1493 Single-Cell RNA-Sequencing-Based CRISPRi Screening Resolves Molecular Drivers of Early
1494 Human Endoderm Development. Cell Rep. *27*, 708–718.e10.
1495 Glykofrydis, F., Cachat, E., Berzanskyte, I., Dzierzak, E., and Davies, J.A. (2021).
1496 Bioengineering Self-Organizing Signaling Centers to Control Embryoid Body Pattern
1497 Elaboration. ACS Synth. Biol. *10*, 1465–1480.
1498 Gouveia, A., Marcelino, H.M., Gonçalves, L., Palmeirim, I., and Andrade, R.P. (2015).
1499 Patterning in time and space: HoxB cluster gene expression in the developing chick embryo. Cell
1500 Cycle *14*, 135–145.
1501 Grant, C.E., Bailey, T.L., and Noble, W.S. (2011). FIMO: scanning for occurrences of a given
1502 motif. Bioinformatics *27*, 1017–1018.
1503 Grosswendt, S., Kretzmer, H., Smith, Z.D., Kumar, A.S., Hetzel, S., Wittler, L., Klages, S.,
1504 Timmermann, B., Mukherji, S., and Meissner, A. (2020). Epigenetic regulator function through
1505 mouse gastrulation. Nature *584*, 102–108.
1506 Gu, P., LeMenuet, D., Chung, A.C.-K., Mancini, M., Wheeler, D.A., and Cooney, A.J. (2005).
1507 Orphan nuclear receptor GCNF is required for the repression of pluripotency genes during
1508 retinoic acid-induced embryonic stem cell differentiation. Mol. Cell. Biol. *25*, 8507–8519.
1509 Haeussler, M., Zweig, A.S., Tyner, C., Speir, M.L., Rosenbloom, K.R., Raney, B.J., Lee, C.M.,
1510 Lee, B.T., Hinrichs, A.S., Gonzalez, J.N., et al. (2019). The UCSC Genome Browser database:
1511 2019 update. Nucleic Acids Res. *47*, D853–D858.
1512 Haghverdi, L., Büttner, M., Wolf, F.A., Buettner, F., and Theis, F.J. (2016). Diffusion
1513 pseudotime robustly reconstructs lineage branching. Nat. Methods *13*, 845–848.
1514 Hart, A.H., Hartley, L., Sourris, K., Stadler, E.S., Li, R., Stanley, E.G., Tam, P.P.L., Elefanty,
1515 A.G., and Robb, L. (2002). *Mixl1* is required for axial mesendoderm morphogenesis and
1516 patterning in the murine embryo. Development *129*, 3597–3608.
1517 Hartemink, A.J. (2005). Reverse engineering gene regulatory networks. Nat. Biotechnol. *23*,
1518 554–555.
1519 Haub, O., and Goldfarb, M. (1991). Expression of the fibroblast growth factor-5 gene in the
1520 mouse embryo. Development *112*, 397–406.
1521 Hayward, P., Kalmar, T., and Arias, A.M. (2008). Wnt/Notch signalling and information
1522 processing during development. Development *135*, 411–424.
1523 Huynh-Thu, V.A., Irrthum, A., Wehenkel, L., and Geurts, P. (2010). Inferring regulatory
1524 networks from expression data using tree-based methods. PLoS One *5*.
1525 Kanai-Azuma, M., Kanai, Y., Gad, J.M., Tajima, Y., Taya, C., Kurohmaru, M., Sanai, Y.,
1526 Yonekawa, H., Yazaki, K., Tam, P.P.L., et al. (2002). Depletion of definitive gut endoderm in
1527 Sox17-null mutant mice. Development *129*, 2367–2379.
1528 Karlebach, G., and Shamir, R. (2008). Modelling and analysis of gene regulatory networks. Nat.
1529 Rev. Mol. Cell Biol. *9*, 770–780.
1530 Kennedy, M.W., Chalamalasetty, R.B., Thomas, S., Garriock, R.J., Jailwala, P., and Yamaguchi,
1531 T.P. (2016). Sp5 and Sp8 recruit β-catenin and Tcf1-Lef1 to select enhancers to activate Wnt
1532 target gene transcription. Proc. Natl. Acad. Sci. USA *113*, 3545–3550.

1533 Kim, H.J., Osteil, P., Humphrey, S.J., Cinghu, S., Oldfield, A.J., Patrick, E., Wilkie, E.E., Peng,
1534 G., Suo, S., Jothi, R., et al. (2020). Transcriptional network dynamics during the progression of
1535 pluripotency revealed by integrative statistical learning. Nucleic Acids Res. *48*, 1828–1842.
1536 Klein, A.M., Mazutis, L., Akartuna, I., Tallapragada, N., Veres, A., Li, V., Peshkin, L., Weitz,
1537 D.A., and Kirschner, M.W. (2015). Droplet barcoding for single-cell transcriptomics applied to
1538 embryonic stem cells. Cell *161*, 1187–1201.
1539 Kuleshov, M.V., Jones, M.R., Rouillard, A.D., Fernandez, N.F., Duan, Q., Wang, Z., Koplev, S.,
1540 Jenkins, S.L., Jagodnik, K.M., Lachmann, A., et al. (2016). Enrichr: a comprehensive gene set
1541 enrichment analysis web server 2016 update. Nucleic Acids Res. *44*, W90-7.
1542 Kuroiwa, Y., Kaneko-Ishino, T., Kagitani, F., Kohda, T., Li, L.L., Tada, M., Suzuki, R.,
1543 Yokoyama, M., Shiroishi, T., Wakana, S., et al. (1996). Peg3 imprinted gene on proximal
1544 chromosome 7 encodes for a zinc finger protein. Nat. Genet. *12*, 186–190.
1545 La Manno, G., Soldatov, R., Zeisel, A., Braun, E., Hochgerner, H., Petukhov, V., Lidschreiber,
1546 K., Kastriti, M.E., Lönnerberg, P., Furlan, A., et al. (2018). RNA velocity of single cells. Nature
1547 *560*, 494–498.
1548 Lachmann, A., Xu, H., Krishnan, J., Berger, S.I., Mazloom, A.R., and Ma'ayan, A. (2010).
1549 ChEA: transcription factor regulation inferred from integrating genome-wide ChIP-X
1550 experiments. Bioinformatics *26*, 2438–2444.
1551 Le Novère, N. (2015). Quantitative and logic modelling of molecular and gene networks. Nat.
1552 Rev. Genet. *16*, 146–158.
1553 Letsou, W., and Cai, L. (2016). Noncommutative biology: sequential regulation of complex
1554 networks. PLoS Comput. Biol. *12*, e1005089.
1555 Lu, T., and Mar, J.C. (2020). Investigating transcriptome-wide sex dimorphism by multi-level
1556 analysis of single-cell RNA sequencing data in ten mouse cell types. Biol. Sex Differ. *11*, 61.
1557 Macosko, E.Z., Basu, A., Satija, R., Nemesh, J., Shekhar, K., Goldman, M., Tirosh, I., Bialas,
1558 A.R., Kamitaki, N., Martersteck, E.M., et al. (2015). Highly Parallel Genome-wide Expression
1559 Profiling of Individual Cells Using Nanoliter Droplets. Cell *161*, 1202–1214.
1560 Malaguti, M., Nistor, P.A., Blin, G., Pegg, A., Zhou, X., and Lowell, S. (2013). Bone
1561 morphogenic protein signalling suppresses differentiation of pluripotent cells by maintaining
1562 expression of E-Cadherin. Elife *2*, e01197.
1563 Marbach, D., Prill, R.J., Schaffter, T., Mattiussi, C., Floreano, D., and Stolovitzky, G. (2010).
1564 Revealing strengths and weaknesses of methods for gene network inference. Proc. Natl. Acad.
1565 Sci. USA *107*, 6286–6291.
1566 Marbach, D., Costello, J.C., Küffner, R., Vega, N.M., Prill, R.J., Camacho, D.M., Allison, K.R.,
1567 DREAM5 Consortium, Kellis, M., Collins, J.J., et al. (2012). Wisdom of crowds for robust gene
1568 network inference. Nat. Methods *9*, 796–804.
1569 Margolin, A.A., Nemenman, I., Basso, K., Wiggins, C., Stolovitzky, G., Dalla Favera, R., and
1570 Califano, A. (2006). ARACNE: an algorithm for the reconstruction of gene regulatory networks
1571 in a mammalian cellular context. BMC Bioinformatics *7 Suppl 1*, S7.
1572 Matsumoto, H., Kiryu, H., Furusawa, C., Ko, M.S.H., Ko, S.B.H., Gouda, N., Hayashi, T., and
1573 Nikaido, I. (2017). SCODE: an efficient regulatory network inference algorithm from single-cell
1574 RNA-Seq during differentiation. Bioinformatics *33*, 2314–2321.
1575 McGinnis, C.S., Patterson, D.M., Winkler, J., Conrad, D.N., Hein, M.Y., Srivastava, V., Hu,
1576 J.L., Murrow, L.M., Weissman, J.S., Werb, Z., et al. (2019). MULTI-seq: sample multiplexing
1577 for single-cell RNA sequencing using lipid-tagged indices. Nat. Methods *16*, 619–626.
1578 McLean, A.B., D'Amour, K.A., Jones, K.L., Krishnamoorthy, M., Kulik, M.J., Reynolds, D.M.,

1579 Sheppard, A.M., Liu, H., Xu, Y., Baetge, E.E., et al. (2007). Activin a efficiently specifies
1580 definitive endoderm from human embryonic stem cells only when phosphatidylinositol 3-kinase
1581 signaling is suppressed. Stem Cells *25*, 29–38.
1582 Mendjan, S., Mascetti, V.L., Ortmann, D., Ortiz, M., Karjosukarso, D.W., Ng, Y., Moreau, T.,
1583 and Pedersen, R.A. (2014). NANOG and CDX2 pattern distinct subtypes of human mesoderm
1584 during exit from pluripotency. Cell Stem Cell *15*, 310–325.
1585 Meredith, G.D., D'Ippolito, A., Dudas, M., Zeidner, L.C., Hostetter, L., Faulds, K., Arnold, T.H.,
1586 Popkie, A.P., Doble, B.W., Marnellos, G., et al. (2015). Glycogen synthase kinase-3 (Gsk-3)
1587 plays a fundamental role in maintaining DNA methylation at imprinted loci in mouse embryonic
1588 stem cells. Mol. Biol. Cell *26*, 2139–2150.
1589 Meyer, P.E., Kontos, K., Lafitte, F., and Bontempi, G. (2007). Information-theoretic inference of
1590 large transcriptional regulatory networks. EURASIP J. Bioinform. Syst. Biol. 79879.
1591 Meyer, P.E., Lafitte, F., and Bontempi, G. (2008). minet: A R/Bioconductor package for
1592 inferring large transcriptional networks using mutual information. BMC Bioinformatics *9*, 461.
1593 Mohammad, H.P., and Baylin, S.B. (2010). Linking cell signaling and the epigenetic machinery.
1594 Nat. Biotechnol. *28*, 1033–1038.
1595 Morgan, D., Studham, M., Tjärnberg, A., Weishaupt, H., Swartling, F.J., Nordling, T.E.M., and
1596 Sonnhammer, E.L.L. (2020). Perturbation-based gene regulatory network inference to unravel
1597 oncogenic mechanisms. Sci. Rep. *10*, 14149.
1598 Muñoz-Sanjuán, I., and Brivanlou, A.H. (2002). Neural induction, the default model and
1599 embryonic stem cells. Nat. Rev. Neurosci. *3*, 271–280.
1600 Nord, J., Schill, D., Pulakanti, K., Rao, S., and Cirillo, L.A. (2020). The transcription factor
1601 FoxO1 is required for the establishment of the human definitive endoderm. BioRxiv.
1602 Oki, S., Ohta, T., Shioi, G., Hatanaka, H., Ogasawara, O., Okuda, Y., Kawaji, H., Nakaki, R.,
1603 Sese, J., and Meno, C. (2018). ChIP-Atlas: a data-mining suite powered by full integration of
1604 public ChIP-seq data. EMBO Rep. *19*.
1605 Park, K.-S., Cha, Y., Kim, C.-H., Ahn, H.-J., Kim, D., Ko, S., Kim, K.-H., Chang, M.-Y., Ko, J.-
1606 H., Noh, Y.-S., et al. (2013). Transcription elongation factor Tcea3 regulates the pluripotent
1607 differentiation potential of mouse embryonic stem cells via the Lefty1-Nodal-Smad2 pathway.
1608 Stem Cells *31*, 282–292.
1609 Pelton, T.A., Sharma, S., Schulz, T.C., Rathjen, J., and Rathjen, P.D. (2002). Transient
1610 pluripotent cell populations during primitive ectoderm formation: correlation of in vivo and in
1611 vitro pluripotent cell development. J. Cell Sci. *115*, 329–339.
1612 Perea-Gomez, A., Vella, F.D.J., Shawlot, W., Oulad-Abdelghani, M., Chazaud, C., Meno, C.,
1613 Pfister, V., Chen, L., Robertson, E., Hamada, H., et al. (2002). Nodal antagonists in the anterior
1614 visceral endoderm prevent the formation of multiple primitive streaks. Dev. Cell *3*, 745–756.
1615 Philippidou, P., and Dasen, J.S. (2013). Hox genes: choreographers in neural development,
1616 architects of circuit organization. Neuron *80*, 12–34.
1617 Popkie, A.P., Zeidner, L.C., Albrecht, A.M., D'Ippolito, A., Eckardt, S., Newsom, D.E., Groden,
1618 J., Doble, B.W., Aronow, B., McLaughlin, K.J., et al. (2010). Phosphatidylinositol 3-kinase
1619 (PI3K) signaling via glycogen synthase kinase-3 (Gsk-3) regulates DNA methylation of
1620 imprinted loci. J. Biol. Chem. *285*, 41337–41347.
1621 Pratapa, A., Jalihal, A.P., Law, J.N., Bharadwaj, A., and Murali, T.M. (2020). Benchmarking
1622 algorithms for gene regulatory network inference from single-cell transcriptomic data. Nat.
1623 Methods *17*, 147–154.
1624 Qin, G., Yang, L., Ma, Y., Liu, J., and Huo, Q. (2019). The exploration of disease-specific gene

1625 regulatory networks in esophageal carcinoma and stomach adenocarcinoma. BMC
1626 Bioinformatics *20*, 717.
1627 Qiu, P., Simonds, E.F., Bendall, S.C., Gibbs, K.D., Bruggner, R.V., Linderman, M.D., Sachs, K.,
1628 Nolan, G.P., and Plevritis, S.K. (2011). Extracting a cellular hierarchy from high-dimensional
1629 cytometry data with SPADE. Nat. Biotechnol. *29*, 886–891.
1630 Qiu, X., Rahimzamani, A., Wang, L., Ren, B., Mao, Q., Durham, T., McFaline-Figueroa, J.L.,
1631 Saunders, L., Trapnell, C., and Kannan, S. (2020). Inferring Causal Gene Regulatory Networks
1632 from Coupled Single-Cell Expression Dynamics Using Scribe. Cell Syst. *10*, 265–274.e11.
1633 Rackham, O.J.L., Firas, J., Fang, H., Oates, M.E., Holmes, M.L., Knaupp, A.S., FANTOM
1634 Consortium, Suzuki, H., Nefzger, C.M., Daub, C.O., et al. (2016). A predictive computational
1635 framework for direct reprogramming between human cell types. Nat. Genet. *48*, 331–335.
1636 Rogers, M.B., Hosler, B.A., and Gudas, L.J. (1991). Specific expression of a retinoic acid-
1637 regulated, zinc-finger gene, Rex-1, in preimplantation embryos, trophoblast and spermatocytes.
1638 Development *113*, 815–824.
1639 Roux, M., Laforest, B., Capecchi, M., Bertrand, N., and Zaffran, S. (2015). Hoxb1 regulates
1640 proliferation and differentiation of second heart field progenitors in pharyngeal mesoderm and
1641 genetically interacts with Hoxa1 during cardiac outflow tract development. Dev. Biol. *406*, 247–
1642 258.
1643 Shawlot, W., Wakamiya, M., Kwan, K.M., Kania, A., Jessell, T.M., and Behringer, R.R. (1999).
1644 Lim1 is required in both primitive streak-derived tissues and visceral endoderm for head
1645 formation in the mouse. Development *126*, 4925–4932.
1646 Spangler, A., Su, E.Y., Craft, A.M., and Cahan, P. (2018). A single cell transcriptional portrait of
1647 embryoid body differentiation and comparison to progenitors of the developing embryo. Stem
1648 Cell Res. *31*, 201–215.
1649 Stark, J., Brewer, D., Barenco, M., Tomescu, D., Callard, R., and Hubank, M. (2003).
1650 Reconstructing gene networks: what are the limits? Biochem. Soc. Trans. *31*, 1519–1525.
1651 Street, K., Risso, D., Fletcher, R.B., Das, D., Ngai, J., Yosef, N., Purdom, E., and Dudoit, S.
1652 (2018). Slingshot: cell lineage and pseudotime inference for single-cell transcriptomics. BMC
1653 Genomics *19*, 477.
1654 Sun, X., Meyers, E.N., Lewandoski, M., and Martin, G.R. (1999). Targeted disruption of Fgf8
1655 causes failure of cell migration in the gastrulating mouse embryo. Genes Dev. *13*, 1834–1846.
1656 Takahashi, Y., Hiraoka, S., Kitajima, S., Inoue, T., Kanno, J., and Saga, Y. (2005). Differential
1657 contributions of Mesp1 and Mesp2 to the epithelialization and rostro-caudal patterning of
1658 somites. Development *132*, 787–796.
1659 Takahashi, Y., Yasuhiko, Y., Kitajima, S., Kanno, J., and Saga, Y. (2007). Appropriate
1660 suppression of Notch signaling by Mesp factors is essential for stripe pattern formation leading
1661 to segment boundary formation. Dev. Biol. *304*, 593–603.
1662 Tan, Y., and Cahan, P. (2019). SingleCellNet: A Computational Tool to Classify Single Cell
1663 RNA-Seq Data Across Platforms and Across Species. Cell Syst. *9*, 207–213.e2.
1664 Theka, I., Sottile, F., Aulicino, F., Garcia, A.C., and Cosma, M.P. (2017). Reduced expression of
1665 Paternally Expressed Gene-3 enhances somatic cell reprogramming through mitochondrial
1666 activity perturbation. Sci. Rep. *7*, 9705.
1667 Trapnell, C. (2015). Defining cell types and states with single-cell genomics. Genome Res. *25*,
1668 1491–1498.
1669 Trapnell, C., Cacchiarelli, D., Grimsby, J., Pokharel, P., Li, S., Morse, M., Lennon, N.J., Livak,
1670 K.J., Mikkelsen, T.S., and Rinn, J.L. (2014). The dynamics and regulators of cell fate decisions

1671 are revealed by pseudotemporal ordering of single cells. Nat. Biotechnol. *32*, 381–386.
1672 Treutlein, B., Brownfield, D.G., Wu, A.R., Neff, N.F., Mantalas, G.L., Espinoza, F.H., Desai,
1673 T.J., Krasnow, M.A., and Quake, S.R. (2014). Reconstructing lineage hierarchies of the distal
1674 lung epithelium using single-cell RNA-seq. Nature *509*, 371–375.
1675 Tropepe, V., Hitoshi, S., Sirard, C., Mak, T.W., Rossant, J., and van der Kooy, D. (2001). Direct
1676 neural fate specification from embryonic stem cells: a primitive mammalian neural stem cell
1677 stage acquired through a default mechanism. Neuron *30*, 65–78.
1678 Van den Berge, K., Roux de Bézieux, H., Street, K., Saelens, W., Cannoodt, R., Saeys, Y.,
1679 Dudoit, S., and Clement, L. (2020). Trajectory-based differential expression analysis for single-
1680 cell sequencing data. Nat. Commun. *11*, 1201.
1681 Velten, L., Haas, S.F., Raffel, S., Blaszkiewicz, S., Islam, S., Hennig, B.P., Hirche, C., Lutz, C.,
1682 Buss, E.C., Nowak, D., et al. (2017). Human haematopoietic stem cell lineage commitment is a
1683 continuous process. Nat. Cell Biol. *19*, 271–281.
1684 Villani, A.-C., Satija, R., Reynolds, G., Sarkizova, S., Shekhar, K., Fletcher, J., Griesbeck, M.,
1685 Butler, A., Zheng, S., Lazo, S., et al. (2017). Single-cell RNA-seq reveals new types of human
1686 blood dendritic cells, monocytes, and progenitors. Science *356*.
1687 Wang, Y., Lin, L., Lai, H., Parada, L.F., and Lei, L. (2013). Transcription factor Sox11 is
1688 essential for both embryonic and adult neurogenesis. Dev. Dyn. *242*, 638–653.
1689 Weirauch, M.T., Yang, A., Albu, M., Cote, A.G., Montenegro-Montero, A., Drewe, P.,
1690 Najafabadi, H.S., Lambert, S.A., Mann, I., Cook, K., et al. (2014). Determination and inference
1691 of eukaryotic transcription factor sequence specificity. Cell *158*, 1431–1443.
1692 Wilson, V., Manson, L., Skarnes, W.C., and Beddington, R.S. (1995). The T gene is necessary
1693 for normal mesodermal morphogenetic cell movements during gastrulation. Development *121*,
1694 877–886.
1695 Wolf, F.A., Angerer, P., and Theis, F.J. (2018). SCANPY: large-scale single-cell gene
1696 expression data analysis. Genome Biol. *19*, 15.
1697 Yamamoto, M., Saijoh, Y., Perea-Gomez, A., Shawlot, W., Behringer, R.R., Ang, S.-L.,
1698 Hamada, H., and Meno, C. (2004). Nodal antagonists regulate formation of the anteroposterior
1699 axis of the mouse embryo. Nature *428*, 387–392.
1700 Yeo, J.-C., Jiang, J., Tan, Z.-Y., Yim, G.-R., Ng, J.-H., Göke, J., Kraus, P., Liang, H., Gonzales,
1701 K.A.U., Chong, H.-C., et al. (2014). Klf2 is an essential factor that sustains ground state
1702 pluripotency. Cell Stem Cell *14*, 864–872.
1703 Yu, J., Smith, V.A., Wang, P.P., Hartemink, A.J., and Jarvis, E.D. (2004). Advances to Bayesian
1704 network inference for generating causal networks from observational biological data.
1705 Bioinformatics *20*, 3594–3603.
1706 Yu, J.S.L., Ramasamy, T.S., Murphy, N., Holt, M.K., Czapiewski, R., Wei, S.-K., and Cui, W.
1707 (2015). PI3K/mTORC2 regulates TGF-β/Activin signalling by modulating Smad2/3 activity via
1708 linker phosphorylation. Nat. Commun. *6*, 7212.
1709 Zhang, K., Li, L., Huang, C., Shen, C., Tan, F., Xia, C., Liu, P., Rossant, J., and Jing, N. (2010).
1710 Distinct functions of BMP4 during different stages of mouse ES cell neural commitment.
1711 Development *137*, 2095–2105.
1712 Zheng, G.X.Y., Terry, J.M., Belgrader, P., Ryvkin, P., Bent, Z.W., Wilson, R., Ziraldo, S.B.,
1713 Wheeler, T.D., McDermott, G.P., Zhu, J., et al. (2017). Massively parallel digital transcriptional
1714 profiling of single cells. Nat. Commun. *8*, 14049.
1715 Zhu, Q., Song, L., Peng, G., Sun, N., Chen, J., Zhang, T., Sheng, N., Tang, W., Qian, C., Qiao,
1716 Y., et al. (2014). The transcription factor Pou3f1 promotes neural fate commitment via activation

of neural lineage genes and inhibition of external signaling pathways. Elife *3*.

Figure 1

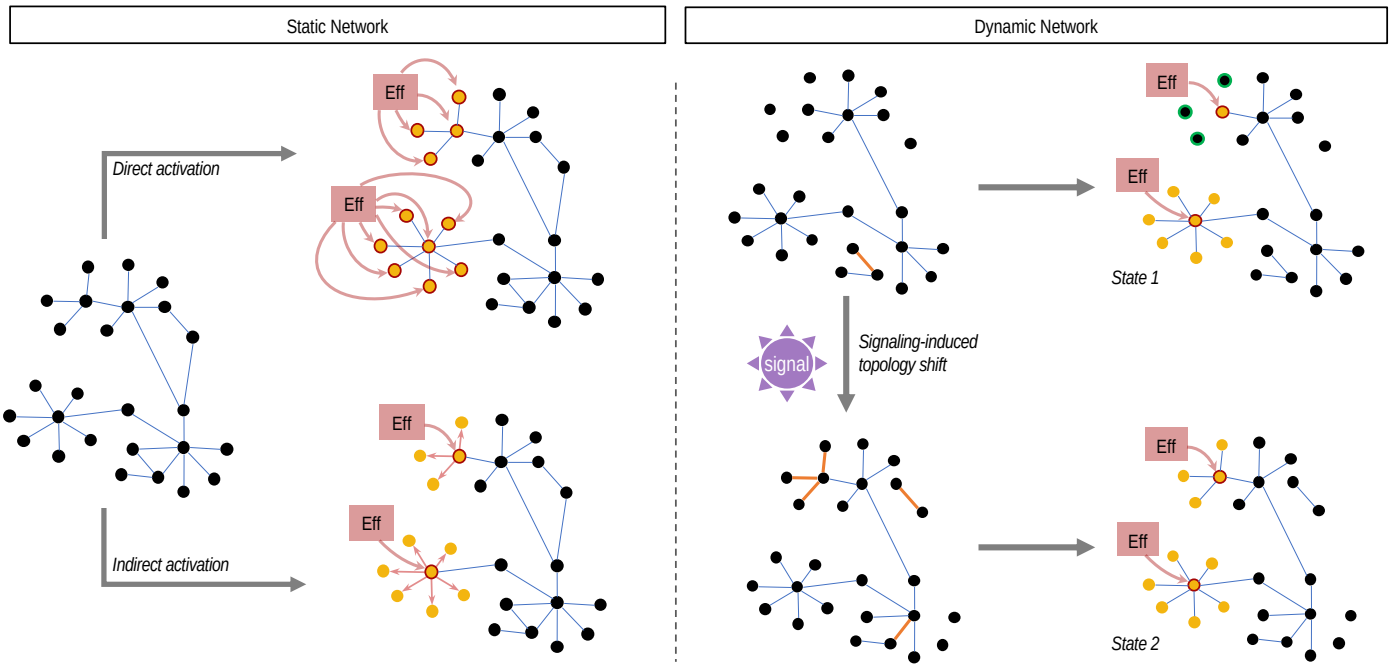
Static Network
Dynamic Network
Direct activation
Indirect activation
Eff
Eff
Eff
Eff
signal
Signaling-induced
topology shift
Eff
Eff
State 1
Eff
Eff
State 2

Figure 2

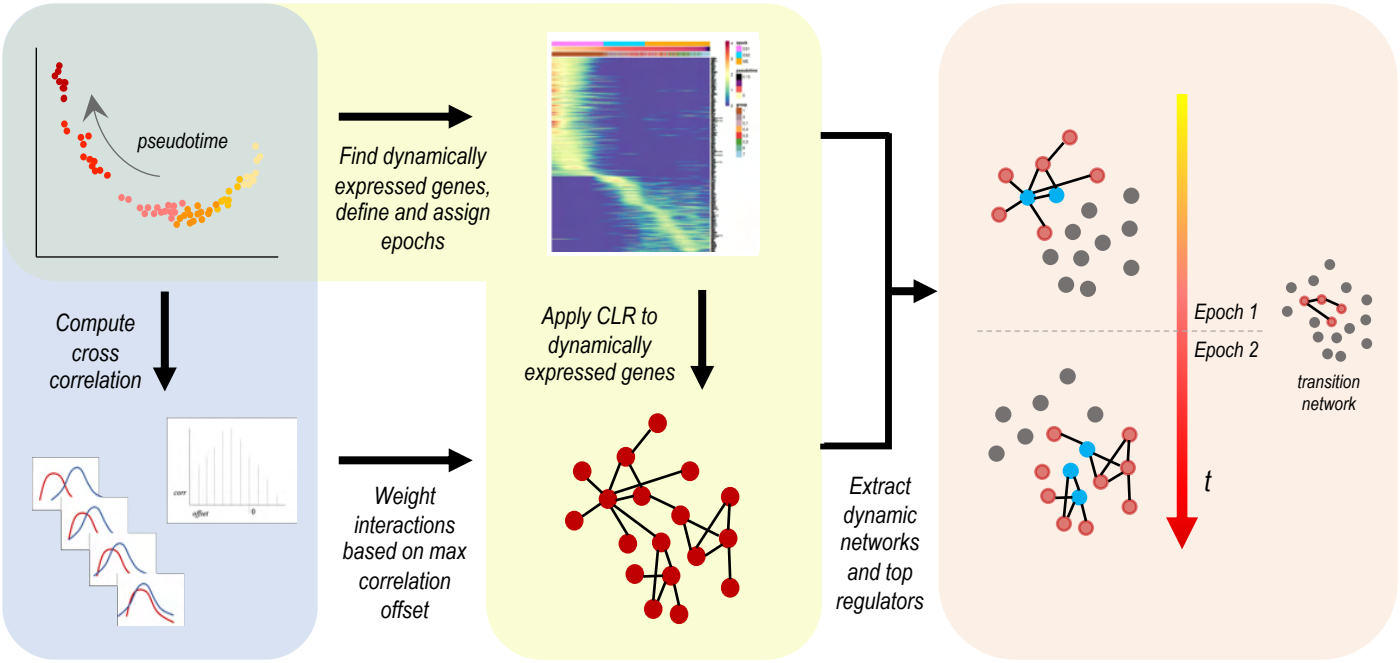
pseudotime
Find dynamically expressed genes, define and assign epochs
Compute cross correlation
Apply CLR to dynamically expressed genes
Weight interactions based on max correlation offset
Extract dynamic networks and top regulators
Epoch 1
Epoch 2
transition network
t

Figure 3

A

Dyngen

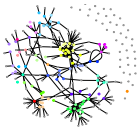

Generate:

- *15 synthetic datasets*
- *100 – 420 genes*
- *20 – 70 TFs*
- *Up to 1000 cells*

Reconstruct

CLR
MI, PCC, MI+crossweight, PCC+crossweight

GENIE3
original, +dynamic gene selection, +crossweight

Epoch
MI, PCC, MI+crossweight, PCC+crossweight

Assess

1. *Generate random networks*
2. *Compute Area under Precision-Recall Curve (AUPR)*
3. *Compare fold improvement of reconstruction over random*

B

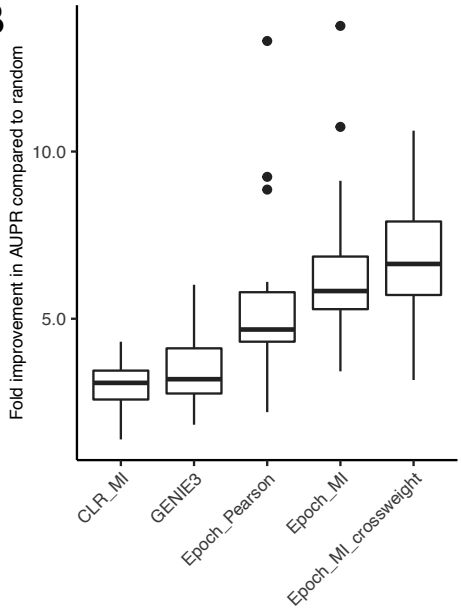

C

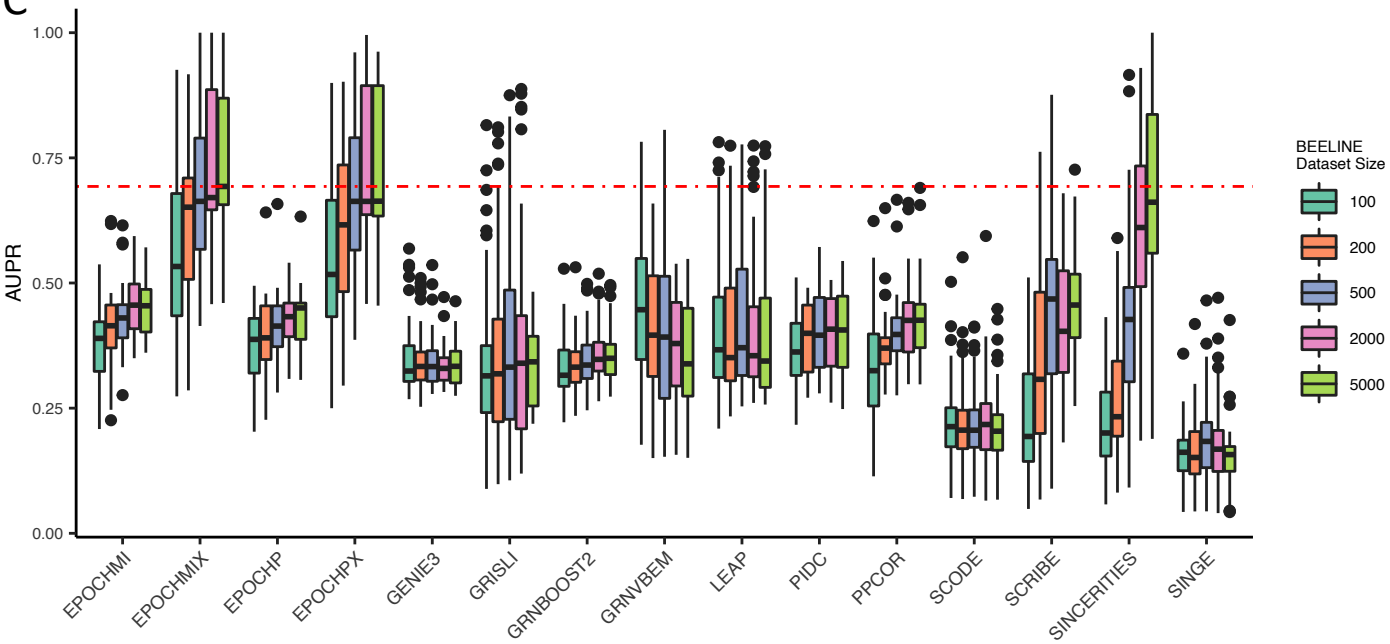

D

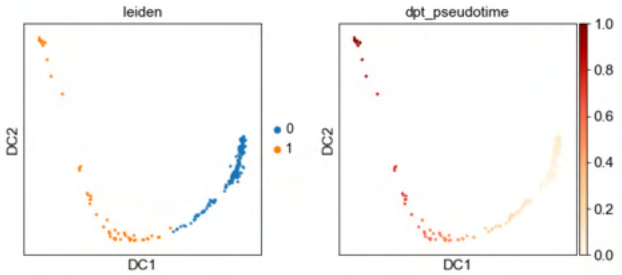

E

Method	Time
GENIE3	21.4 min
Epoch--Pearson	16.8 sec
Epoch--MI	1.4 min
Epoch--MI + cross-weighting	2.5 min

F

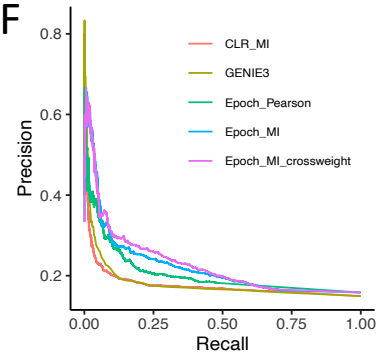

Figure 4

A

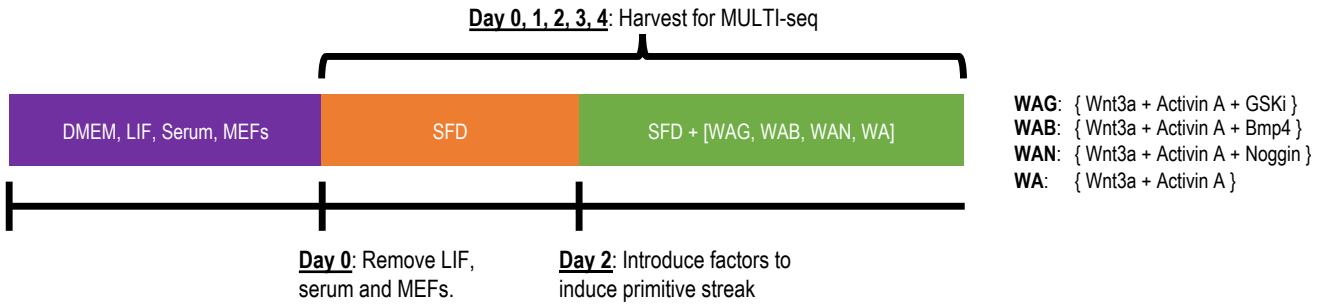

B

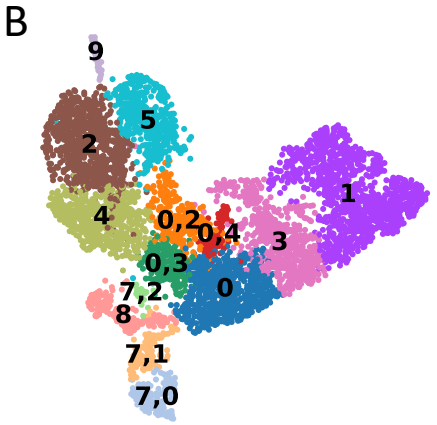

C

D

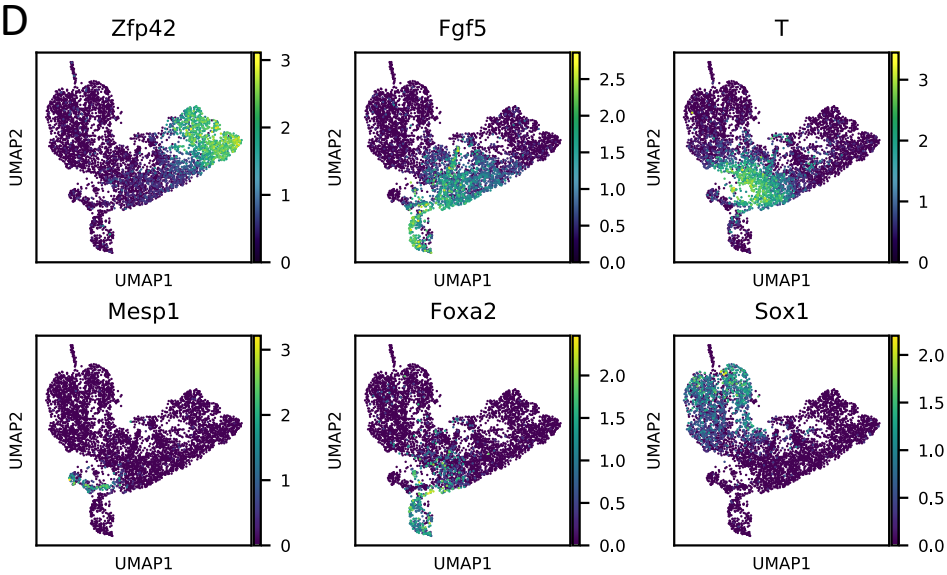

E

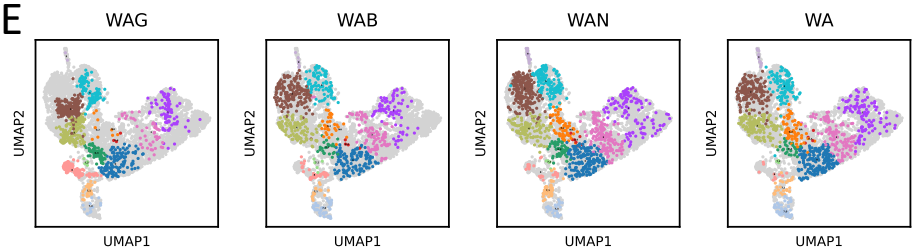

F

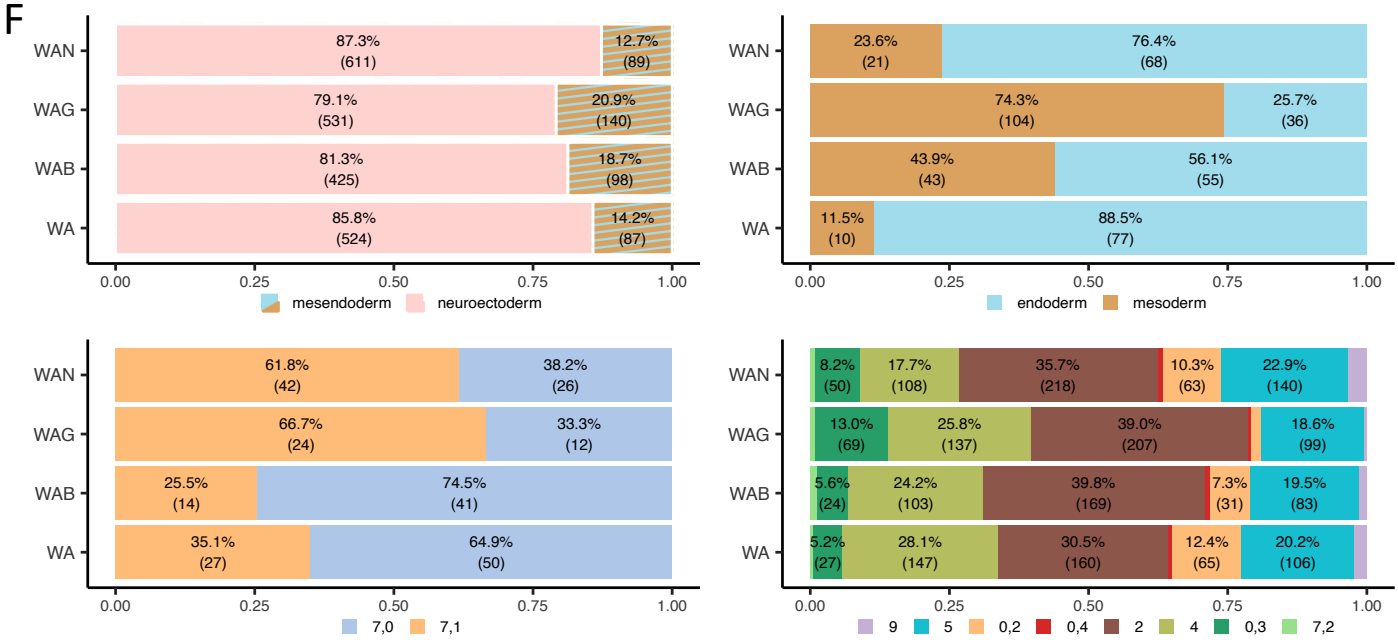

Figure 5

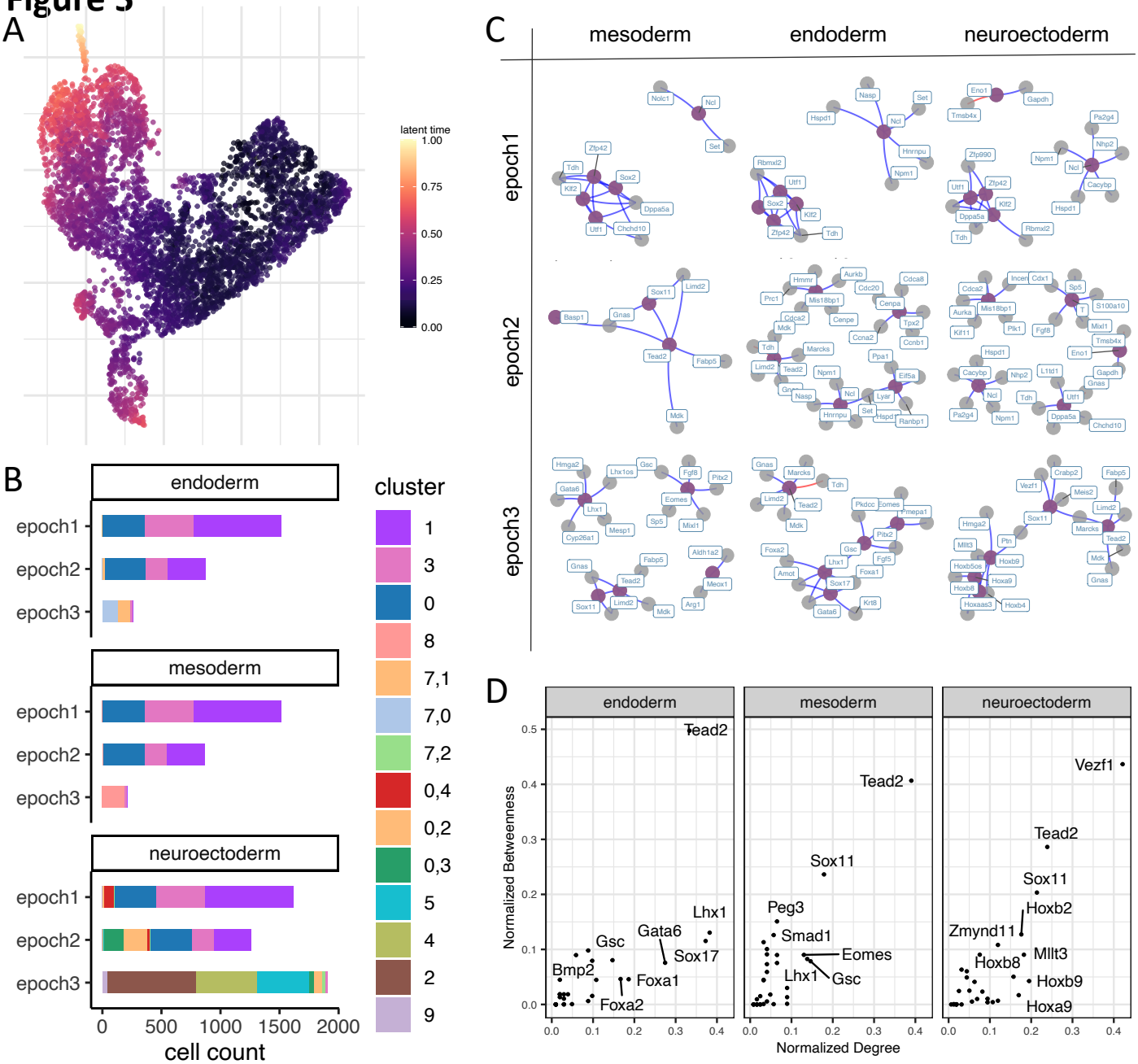
A
latent time
1.00
0.75
0.50
0.25
0.00
B
endoderm
mesoderm
neuroectoderm
epoch1
epoch2
epoch3
0
500
1000
1500
2000
cell count
cluster
1
3
0
8
7,1
7,0
7,2
0,4
0,2
0,3
5
4
2
9
C
mesoderm
endoderm
neuroectoderm
epoch1
epoch2
epoch3
D
endoderm
mesoderm
neuroectoderm
Normalized Betweenness
Normalized Degree
Tead2
Lhx1
Gata6
Gsc
Sox17
Bmp2
Foxa1
Foxa2
Sox11
Peg3
Smad1
Eomes
Vezf1
Hoxb2
Zmynd11
Mllt3
Hoxb8
Hoxb9
Hoxa9

Figure 6

A

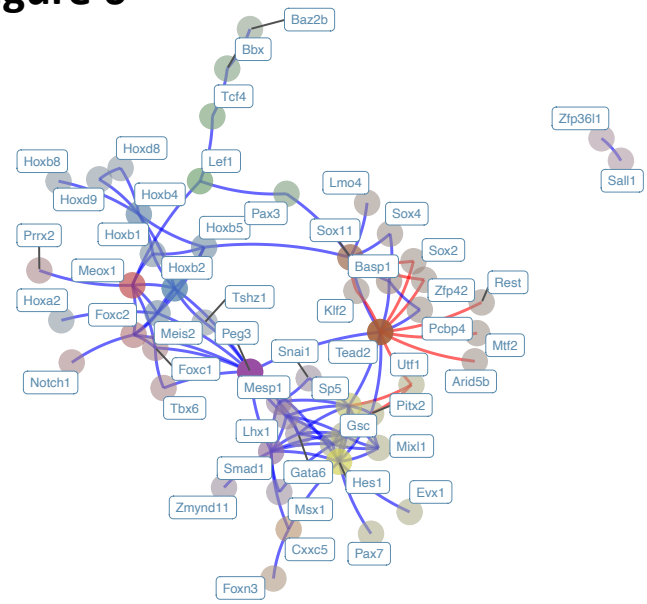

C

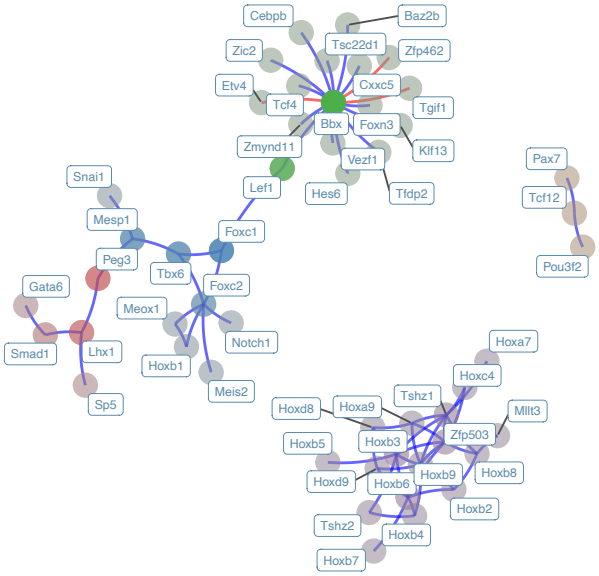

B

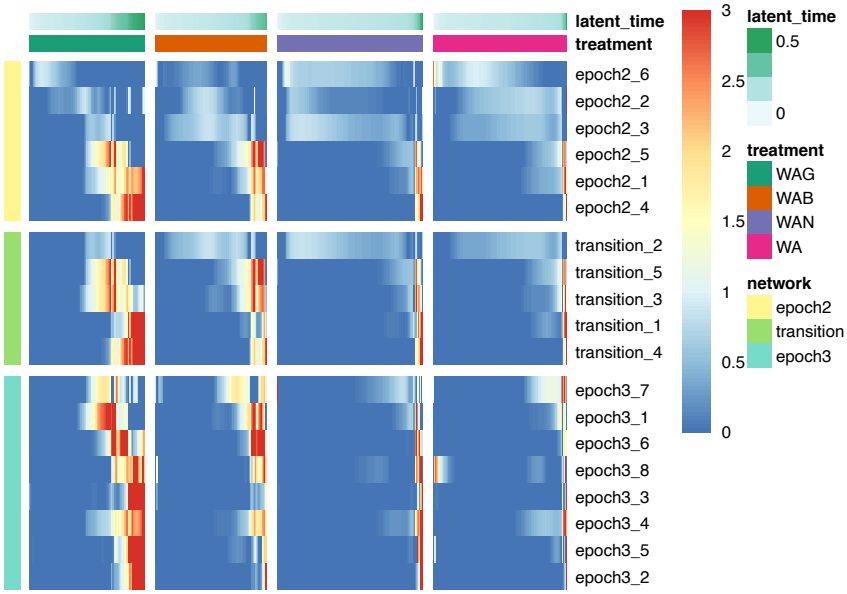

D

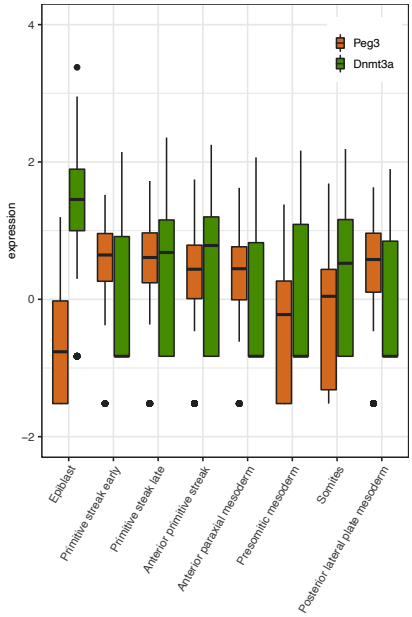

Figure 7

A

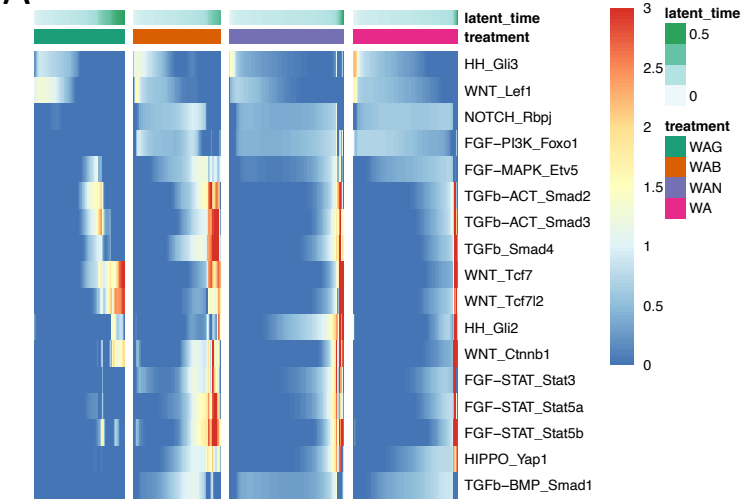

C

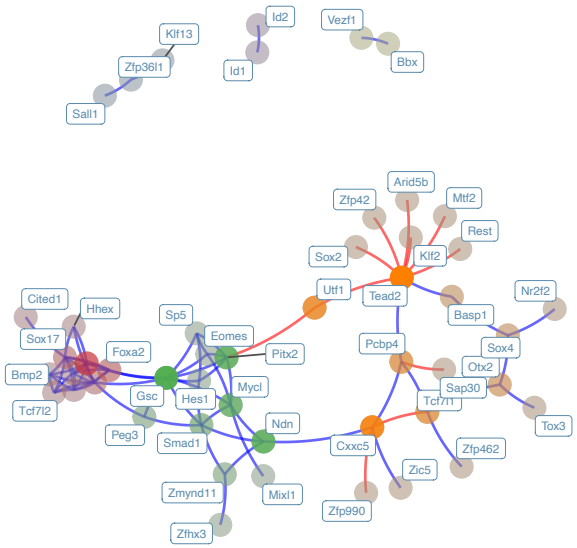

B

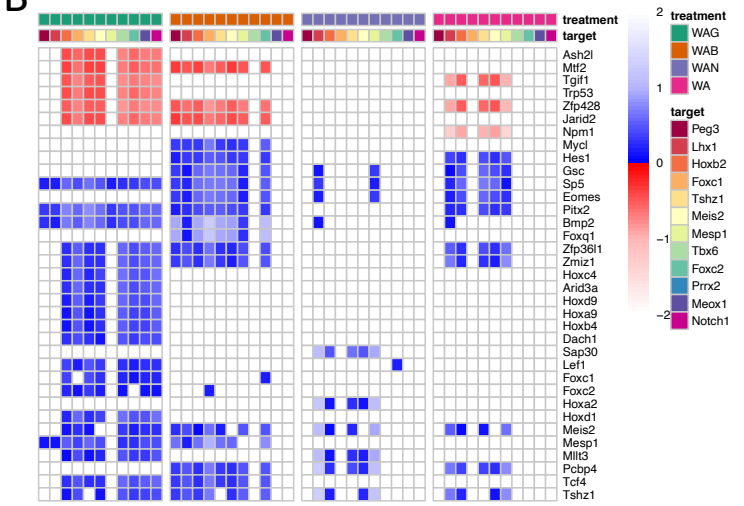

D

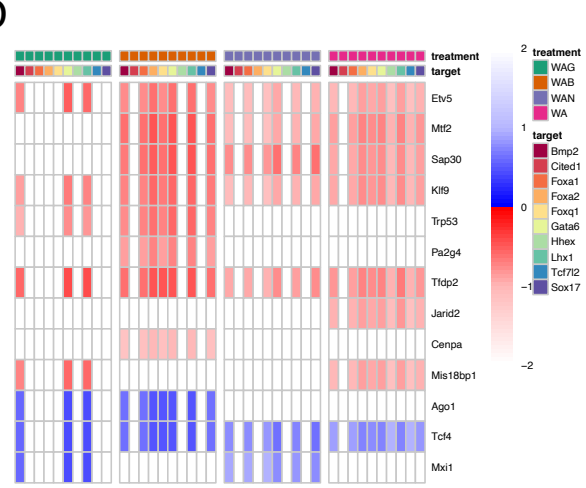

Figure 8

A

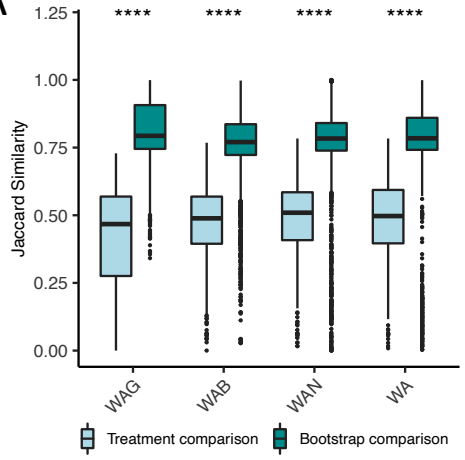

B

TF	avg(JS)	Hes7	0.124	Lmo2	0.260
Prrx2	0.061	Cited1	0.130	Mixl1	0.280
Tbx6	0.068	Gata6	0.192	Lhx1	0.283
Mesp1	0.099	Isl1	0.203	Ets1	0.297
Gata4	0.114	Hey1	0.213		

C

Figure 9

A

in vivo top regulators by PageRank			
	epoch1	epoch2	epoch3
1	Utf1	Lef1	Cited1
2	Pou3f1	Hoxb1	Lef1
3	Pou5f1	Nr6a1	Snai1
4	Otx2	Peg3	Hoxb1
5	Hes1	Snai1	Lmo4
6	Sox2	Lmo4	Nr6a1
7	Id3	Pou5f1	Cdx2
8	Eomes	Meis2	Cdx1
9	Jund	Sp5	Tbx6
10	Foxa2	Tsc22d1	Hoxb2
11	Hopx	Mesp1	Sp5
12	Npm1	T	Meis2
13	Dnmt3b	Id1	Tsc22d1
14	Foxd3	Lhx1	Hes7
15	Rbpms2	Id3	Hoxb9

in vivo top regulators by Betweenness & Degree			
	epoch1	epoch2	epoch3
1	Utf1	Lef1	Lef1
2	Pou3f1	Hoxb1	Cited1
3	Pou5f1	Peg3	Snai1
4	Otx2	Nr6a1	Hoxb1
5	Hes1	Snai1	Nr6a1
6	Sox2	Lmo4	Lmo4
7	Eomes	Pou5f1	Cdx2
8	Dnmt3b	Meis2	Hoxb2
9	Jund	Sp5	Sp5
10	Id3	T	Tbx6
11	Rbpms2	Tsc22d1	Cdx1
12	Hopx	Id1	Hes7
13	Npm1	Mesp1	Hoxa9
14	Foxa2	Lhx1	Meis2
15	Snrpn	Id3	Id1

B

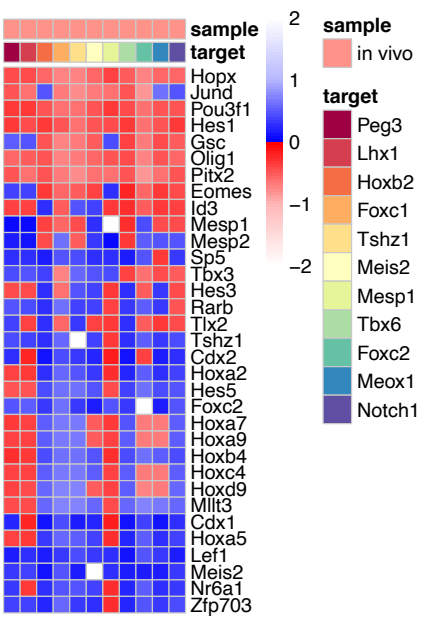

C

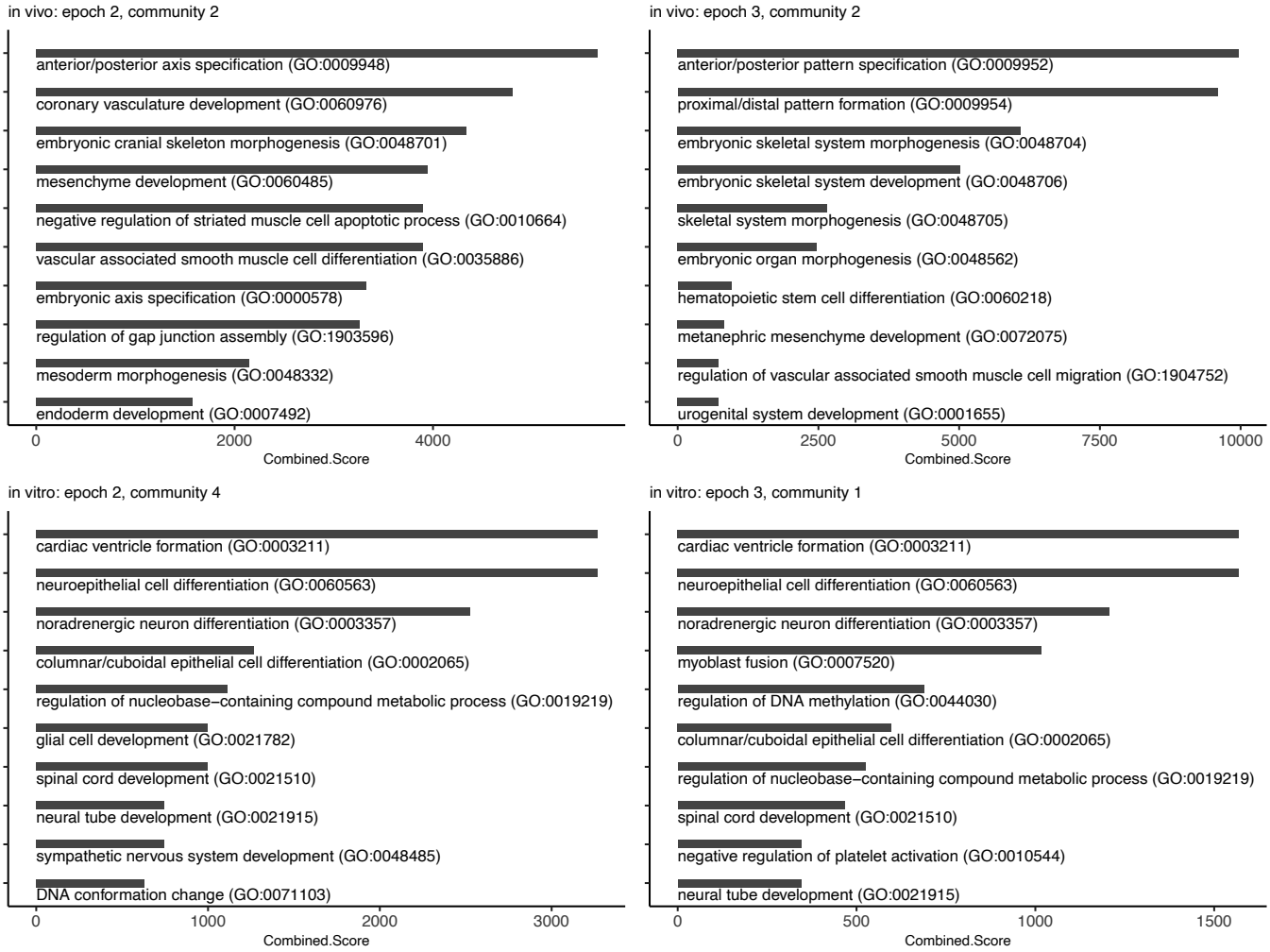

Supplementary Figure 1

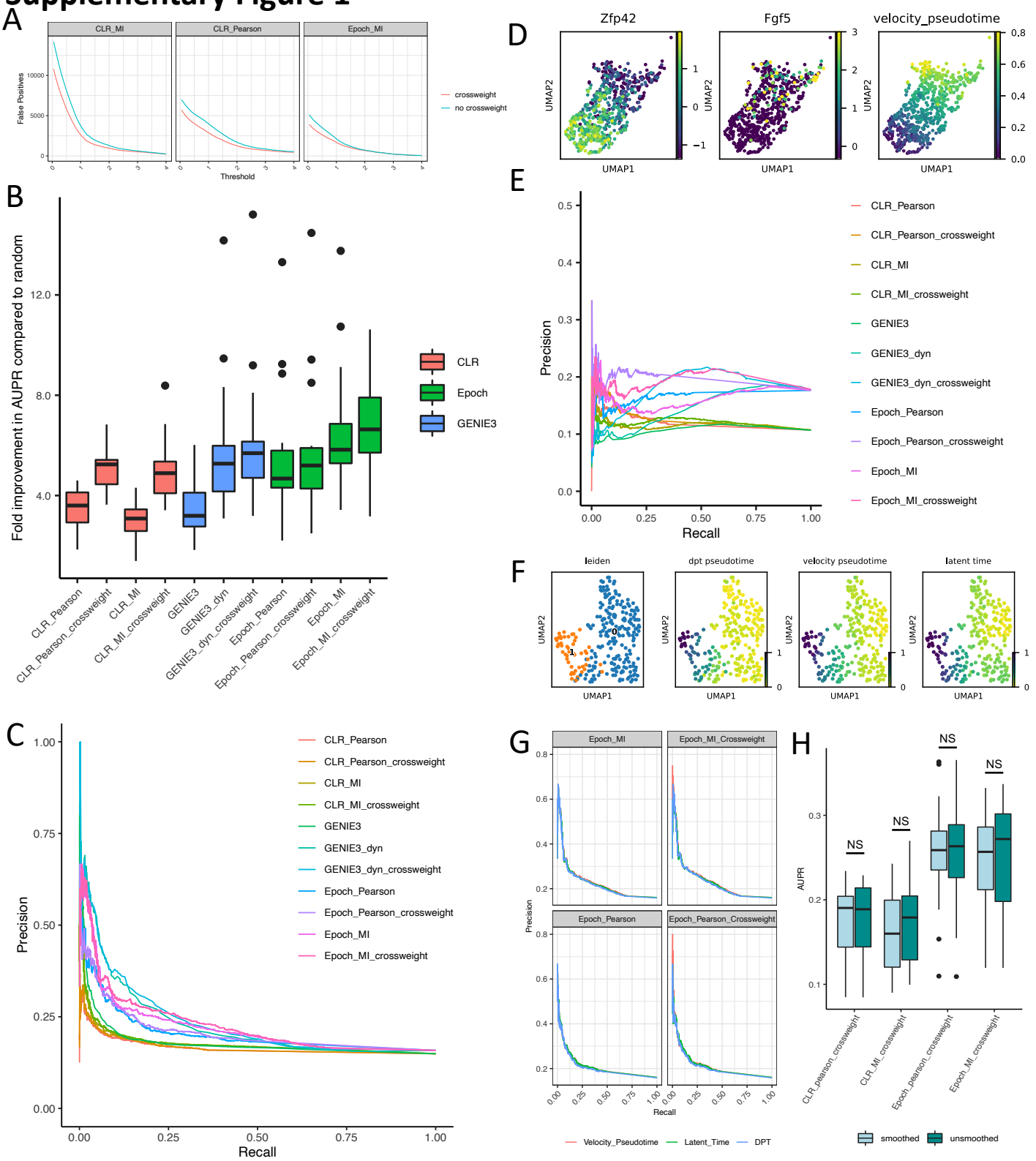

Supplementary Figure 2

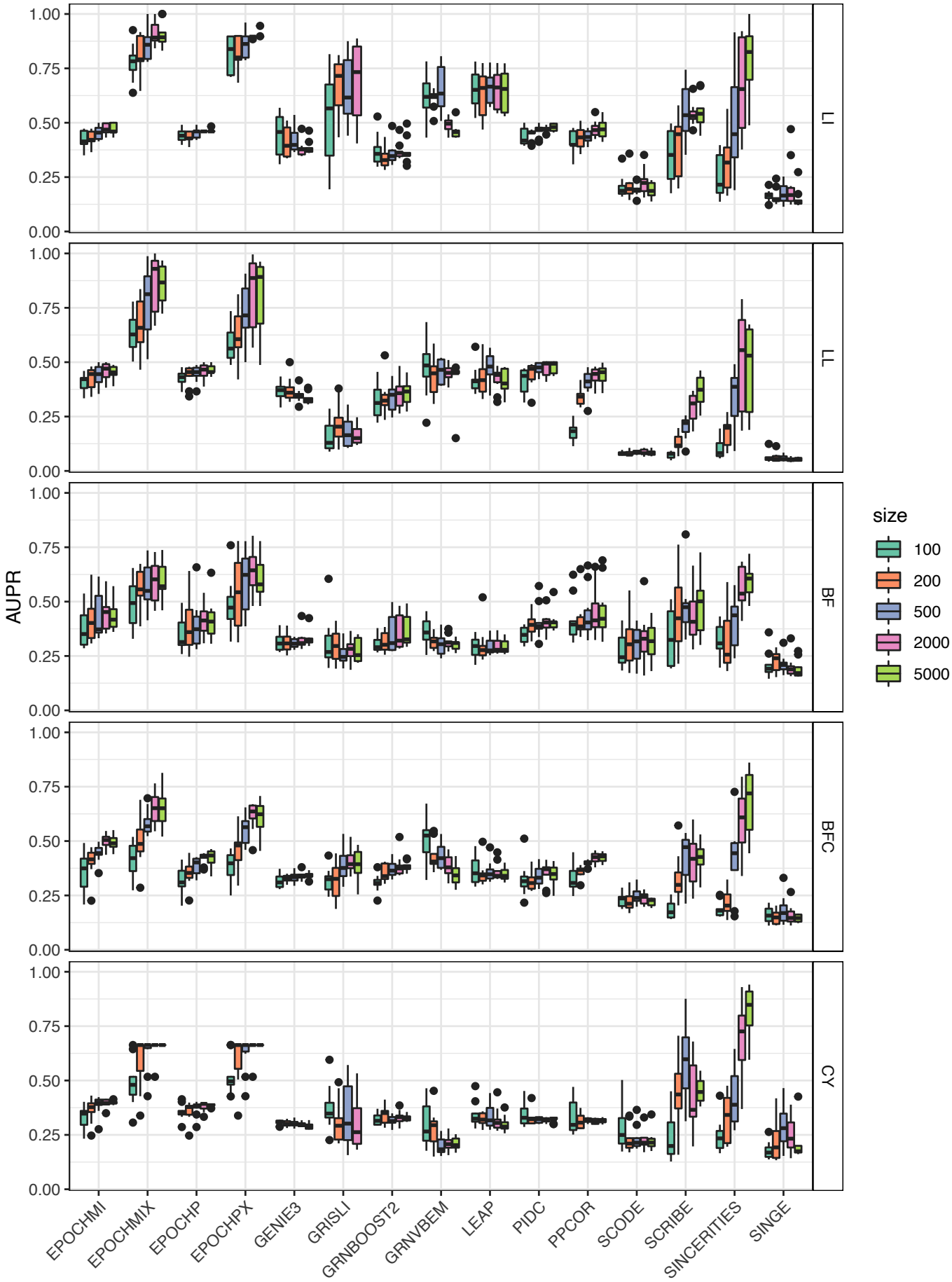

Supplementary Figure 3

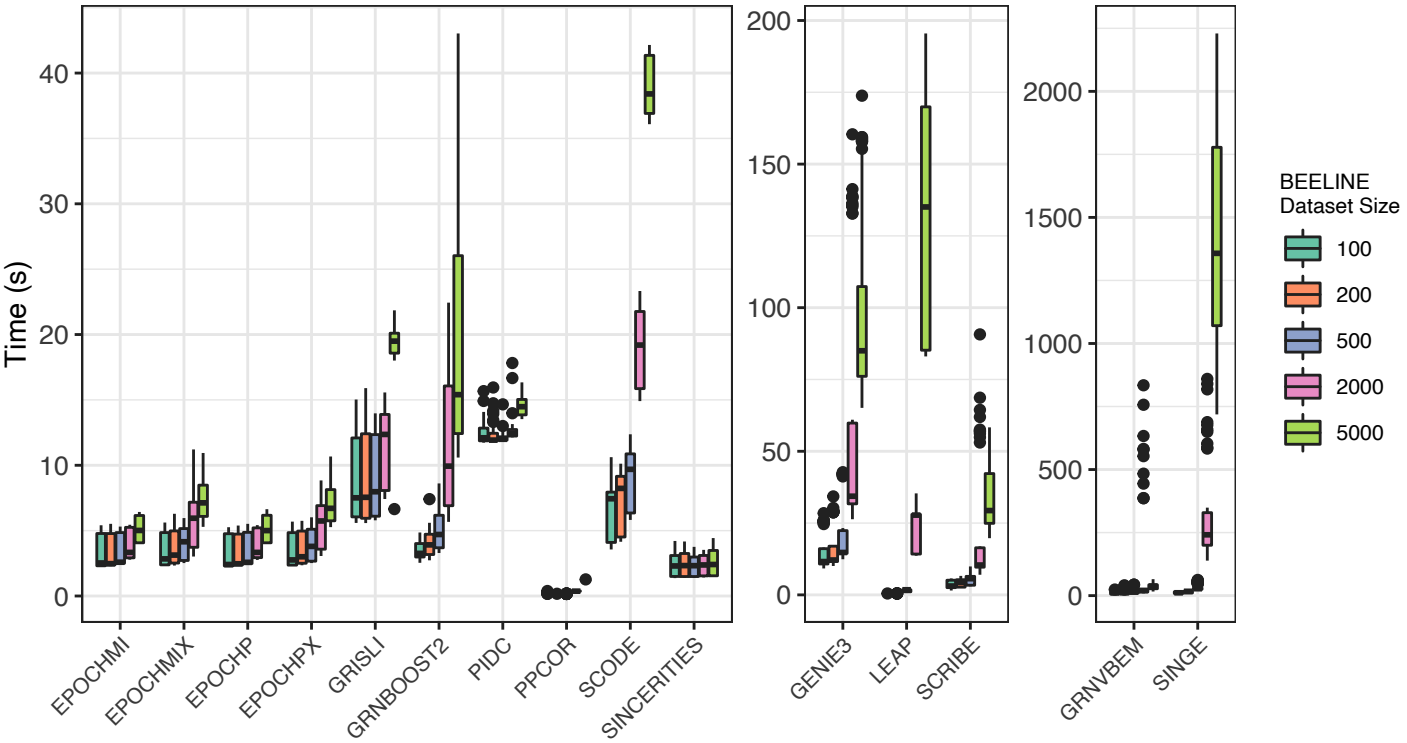

Supplementary Figure 4

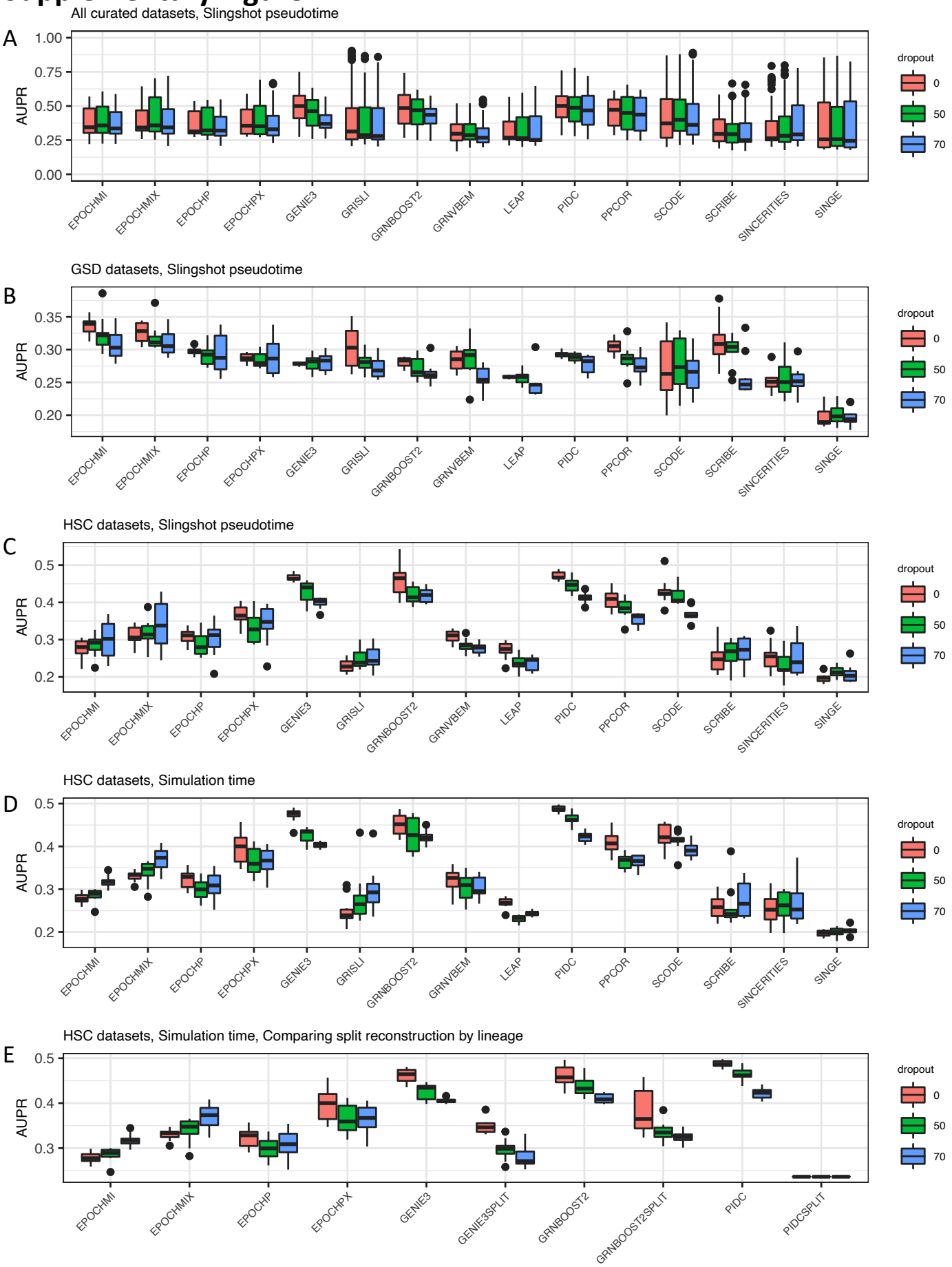

Supplementary Figure 5

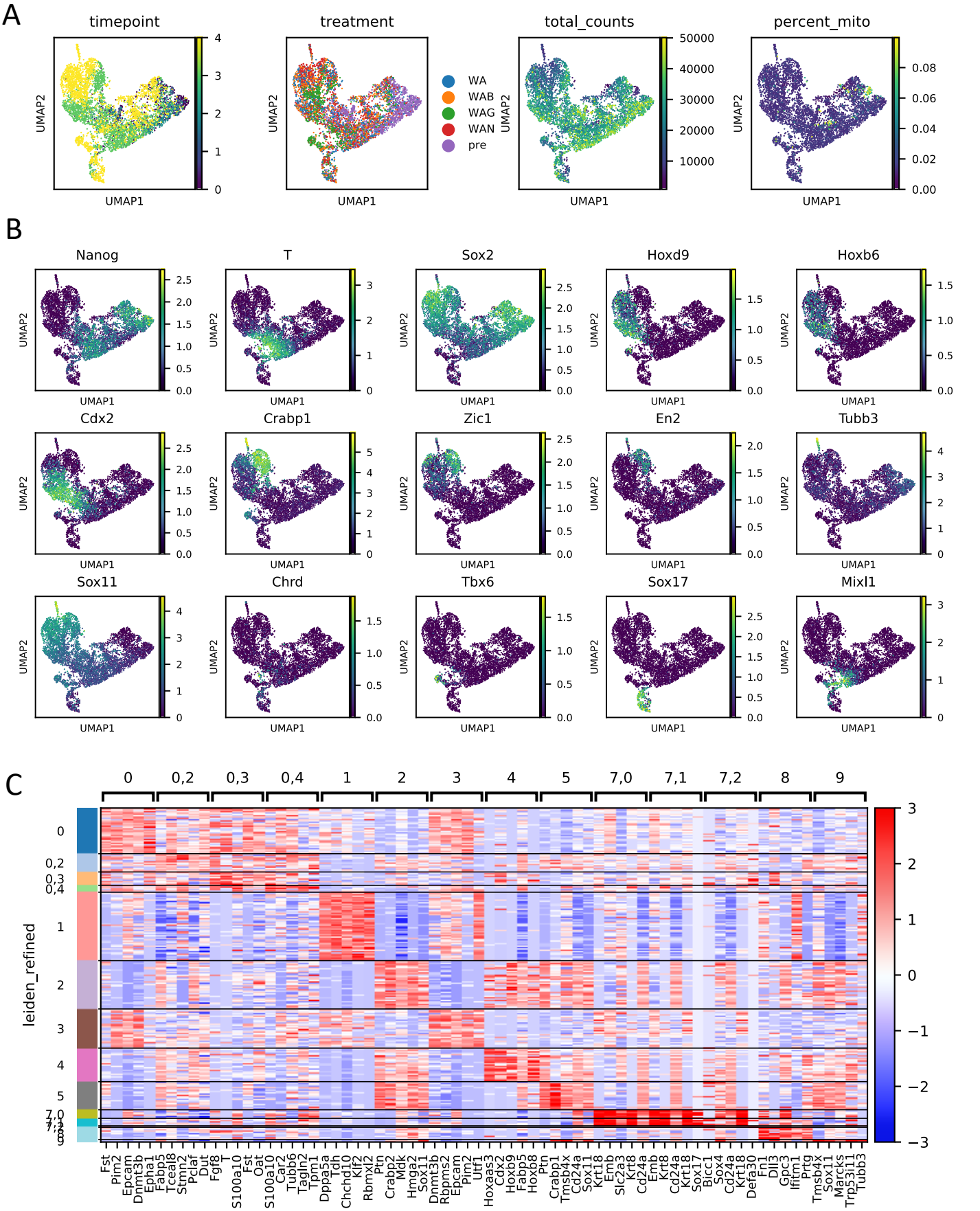

Supplementary Figure 6

A

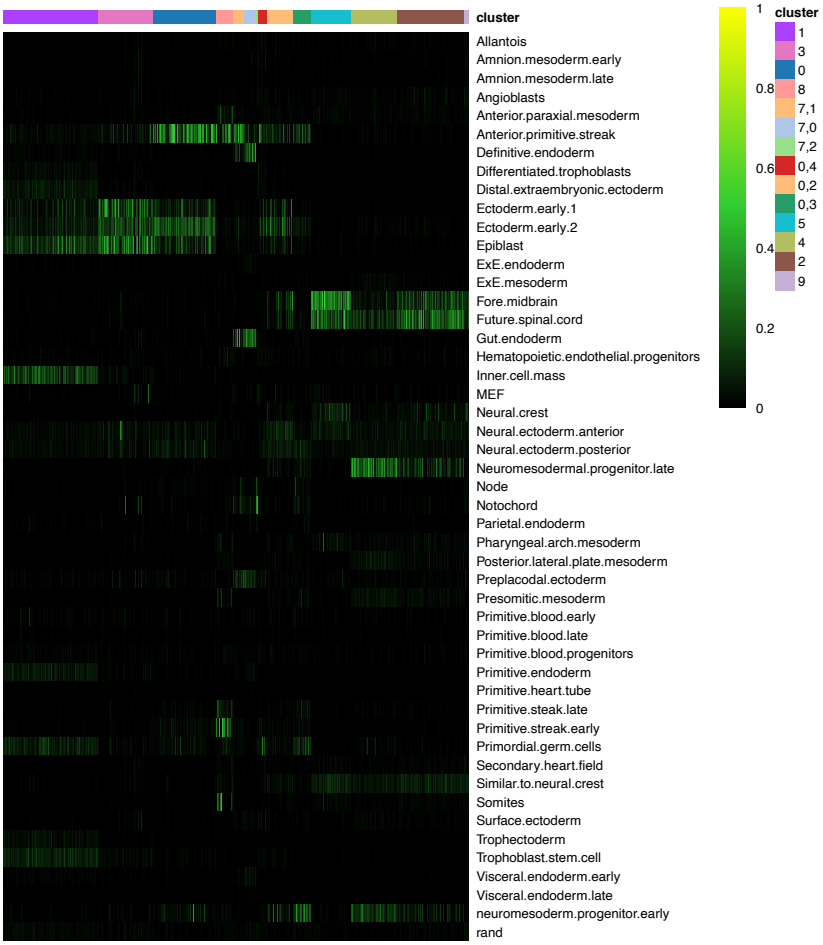

B

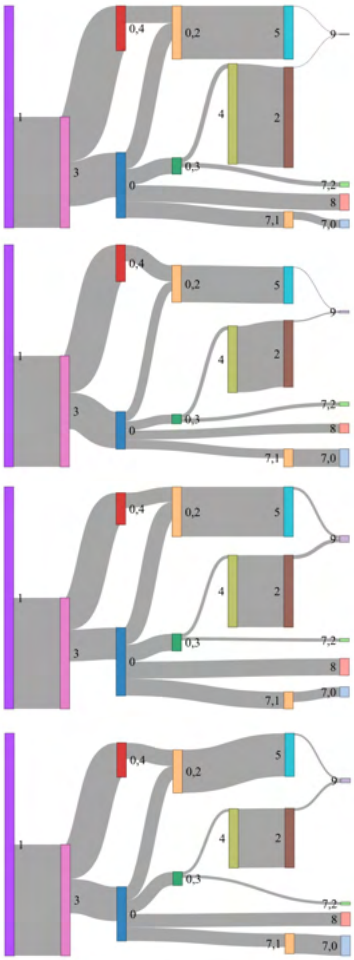

Supplementary Figure 7

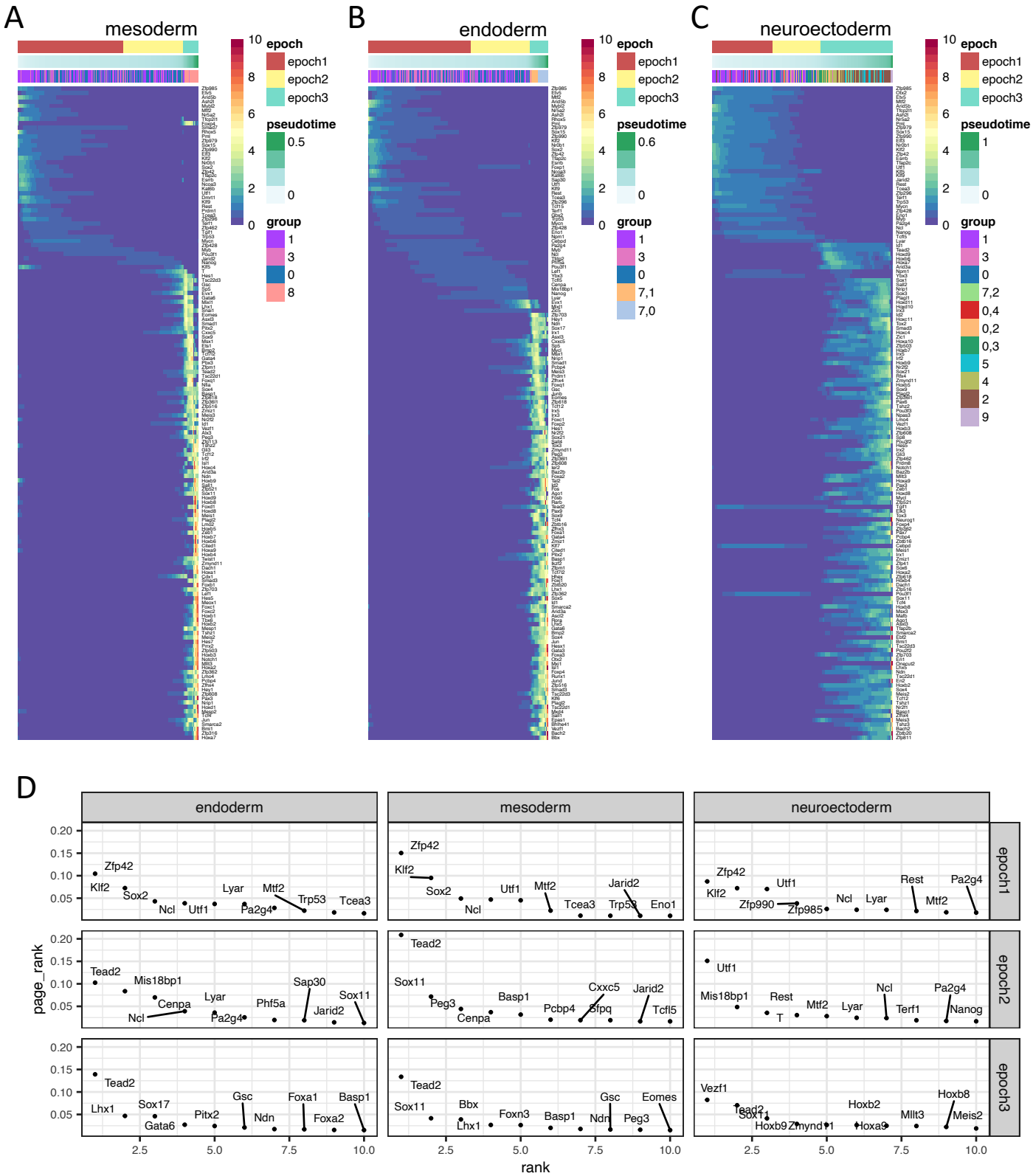

Supplementary Figure 8

A

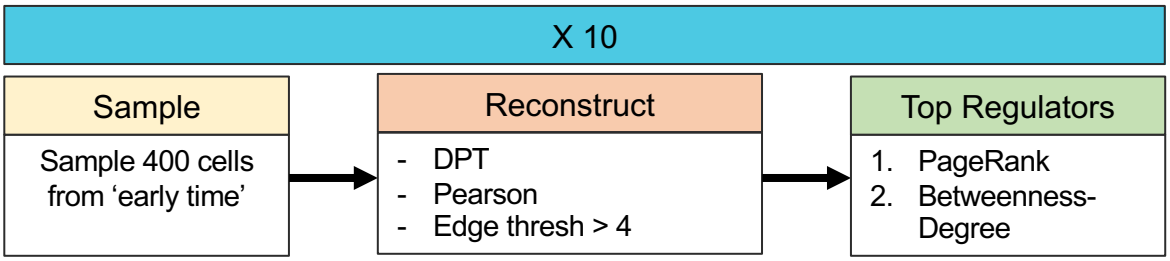

B

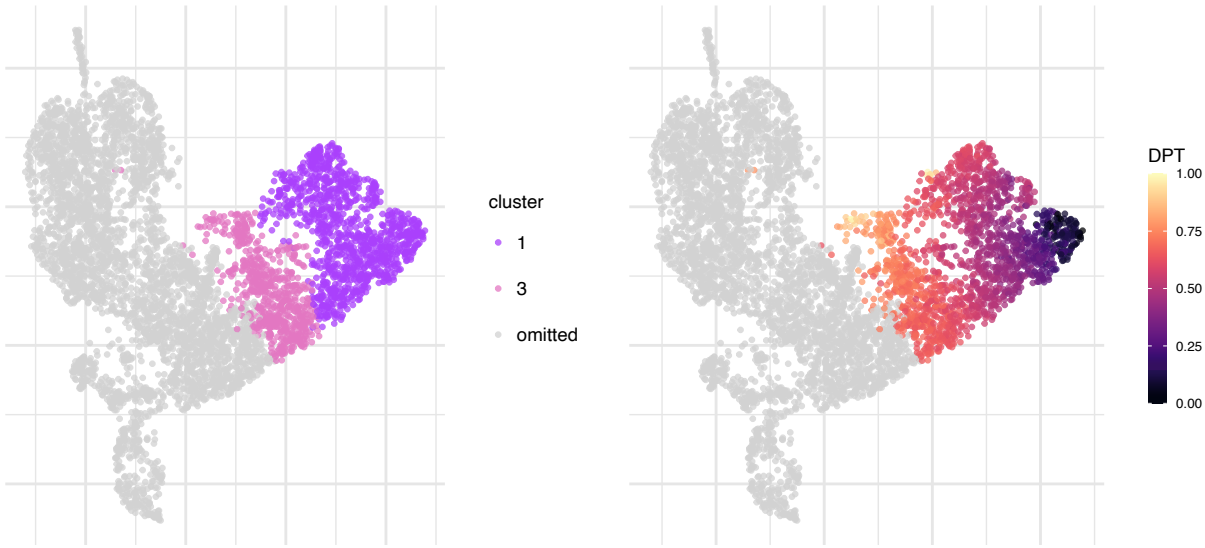

C

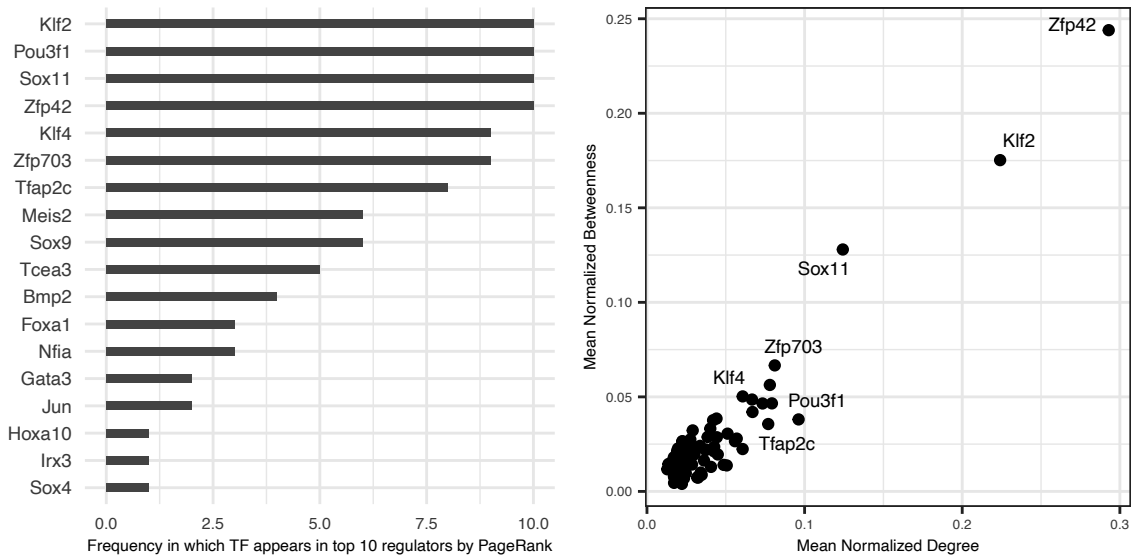

Supplementary Figure 9

A

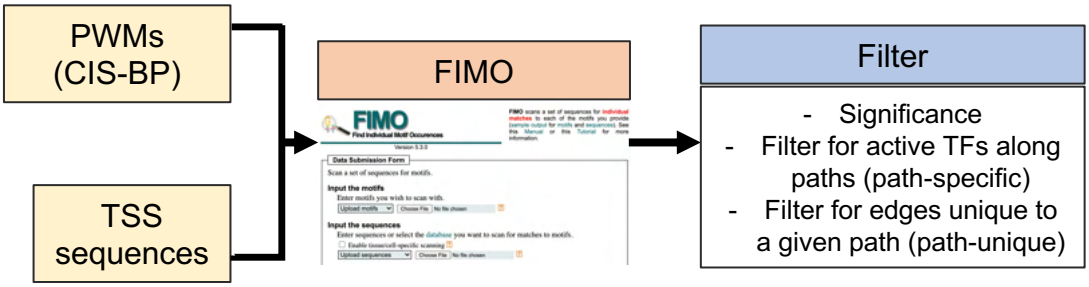

B

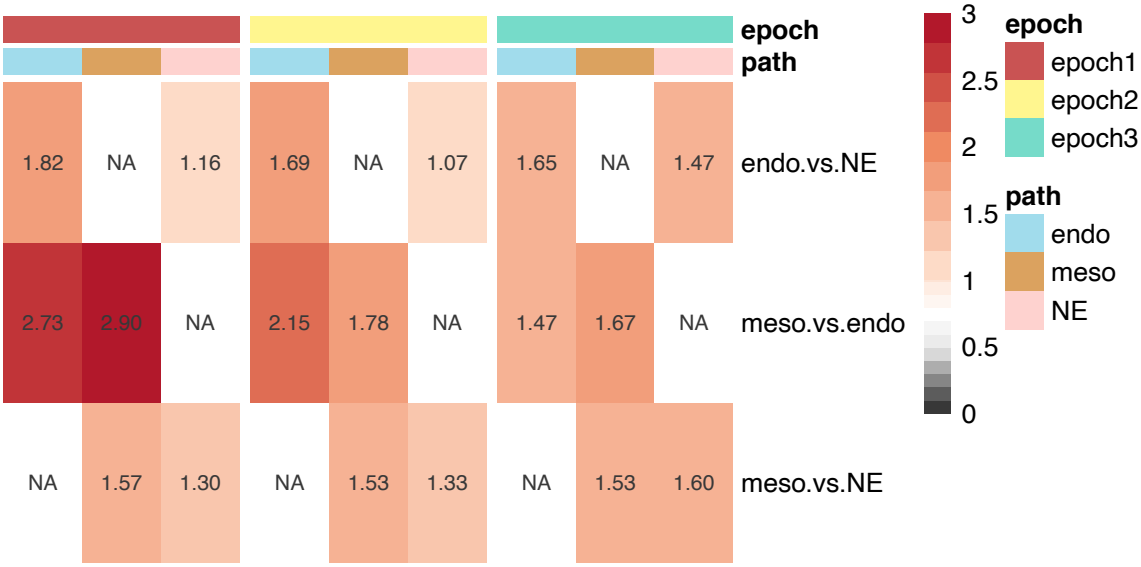

Supplementary Figure 10

Full Reconstruction

epoch1..epoch1

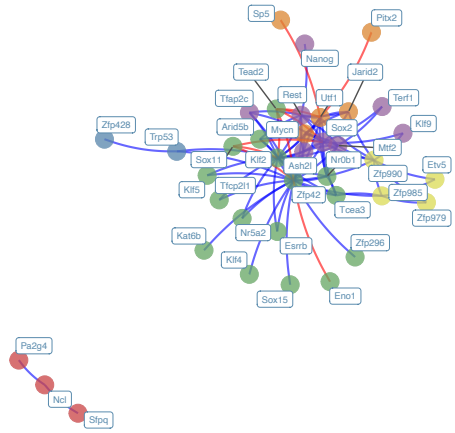

epoch2..epoch2

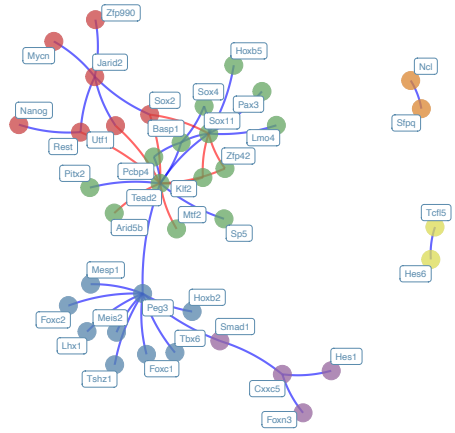

epoch3..epoch3

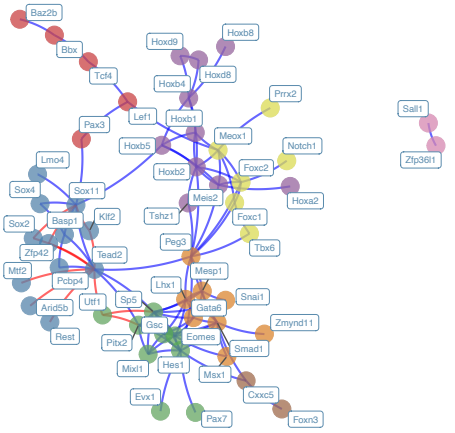

Unique to WAG (vs. WA)

epoch1

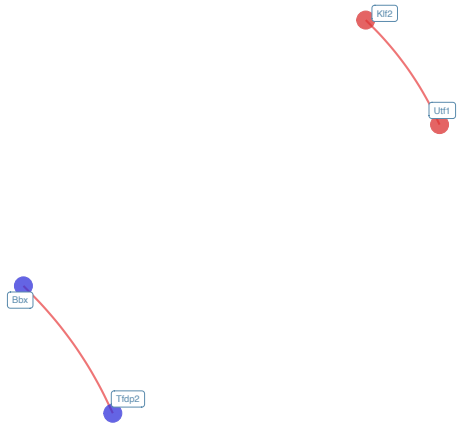

epoch2

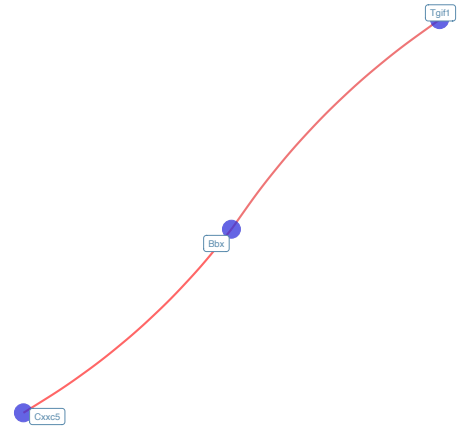

epoch3

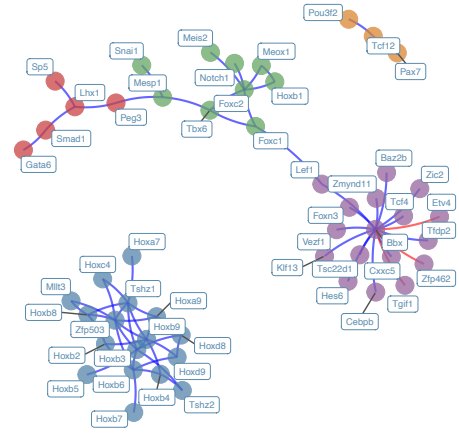

Unique to WA (vs. WAG)

epoch1

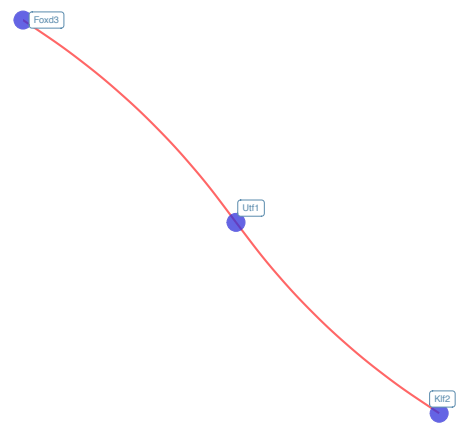

epoch2

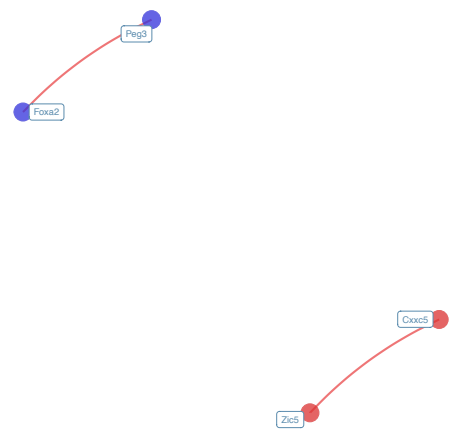

epoch3

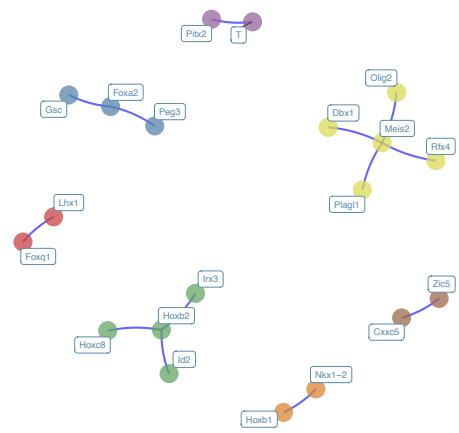

Supplementary Figure 11

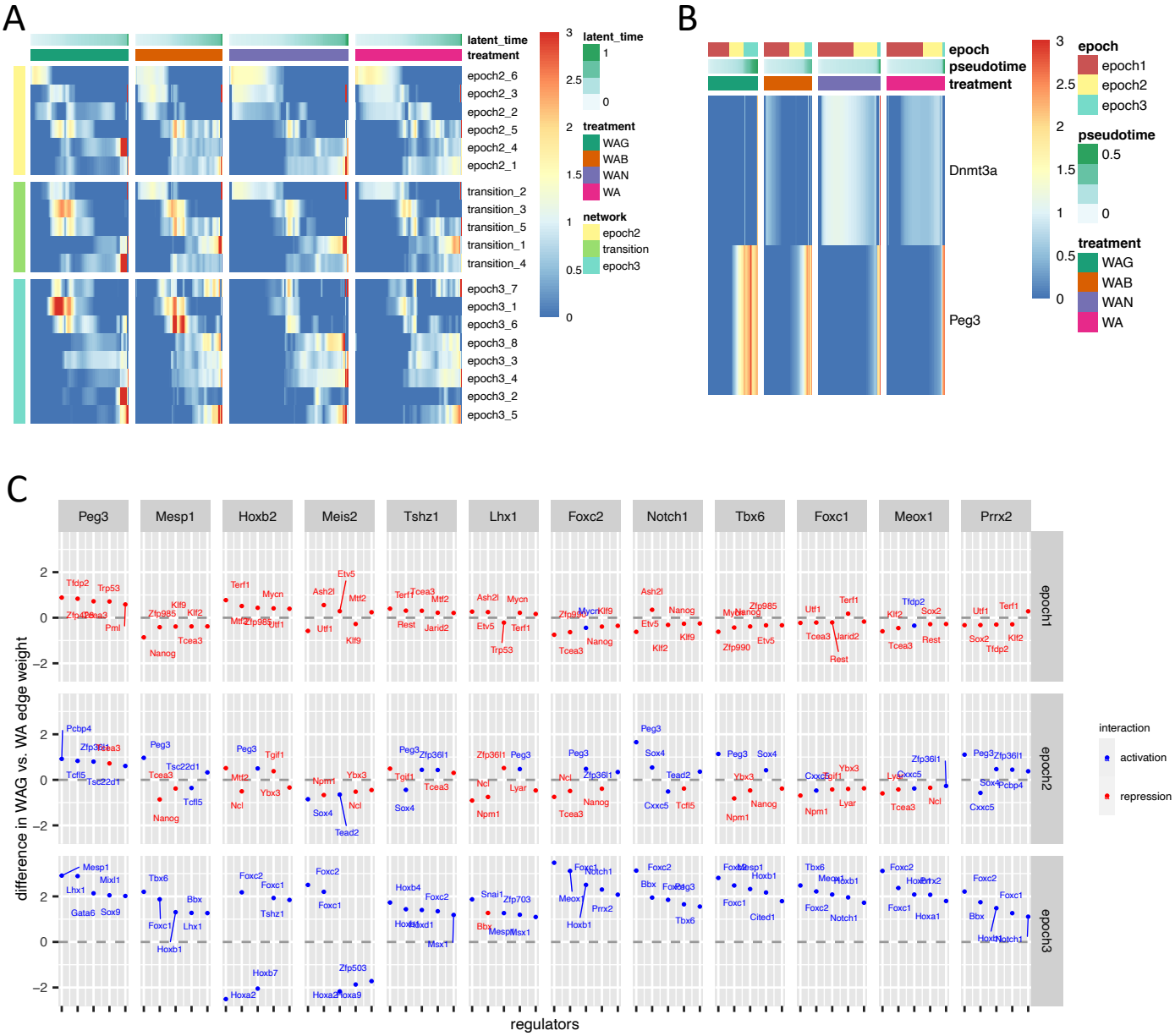

Supplementary Figure 12

Unique to in vivo (vs. in vitro)

epoch1

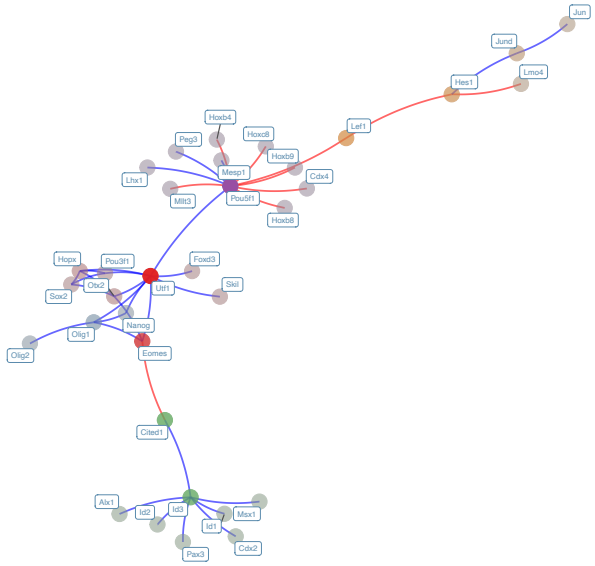

epoch2

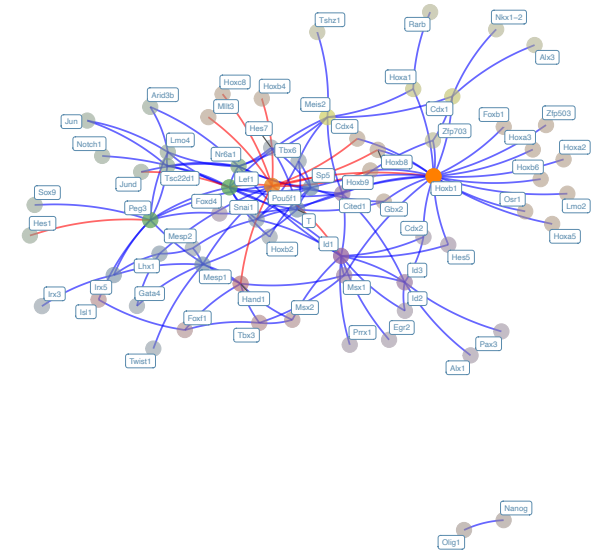

epoch3

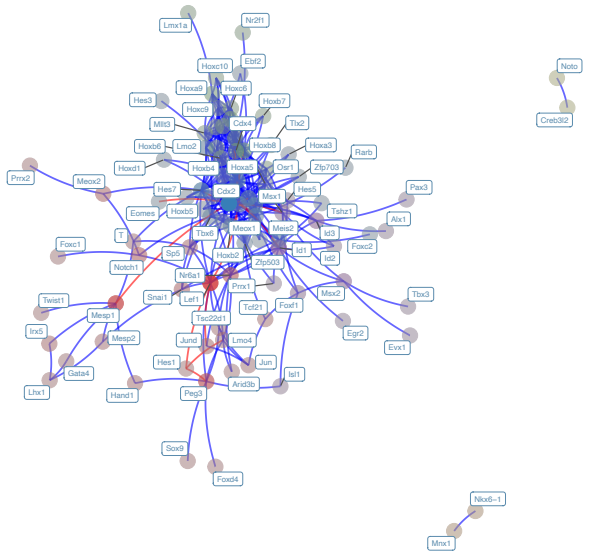

Unique to in vitro (vs. in vivo)

epoch1

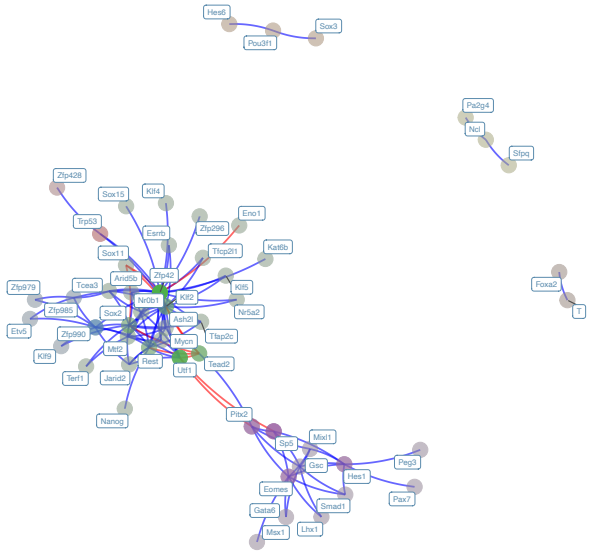

epoch2

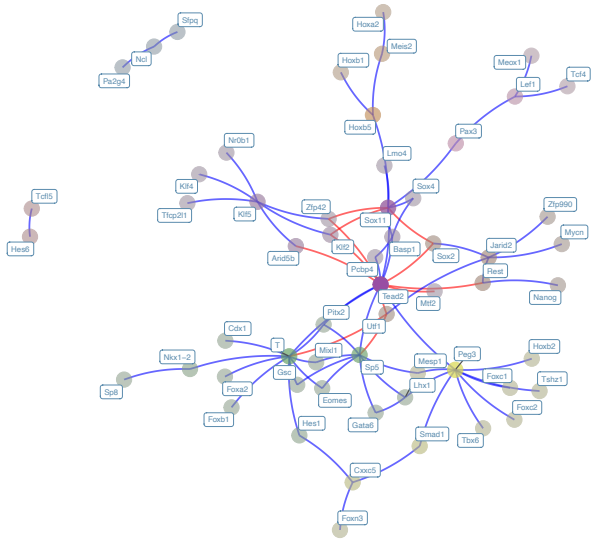

epoch3

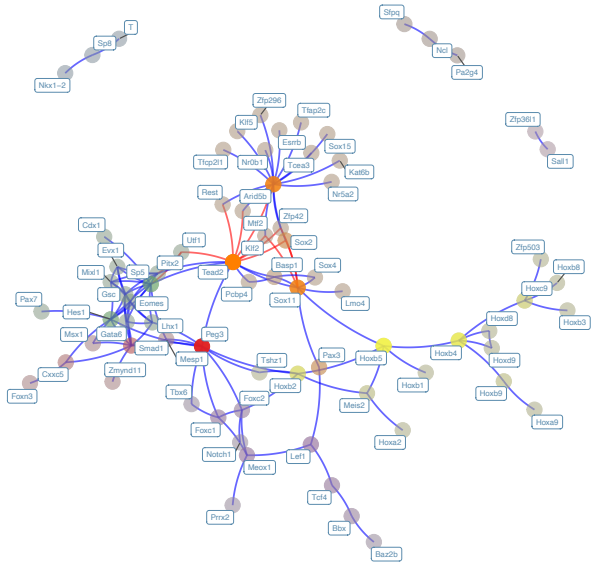

Supplementary Figure 13

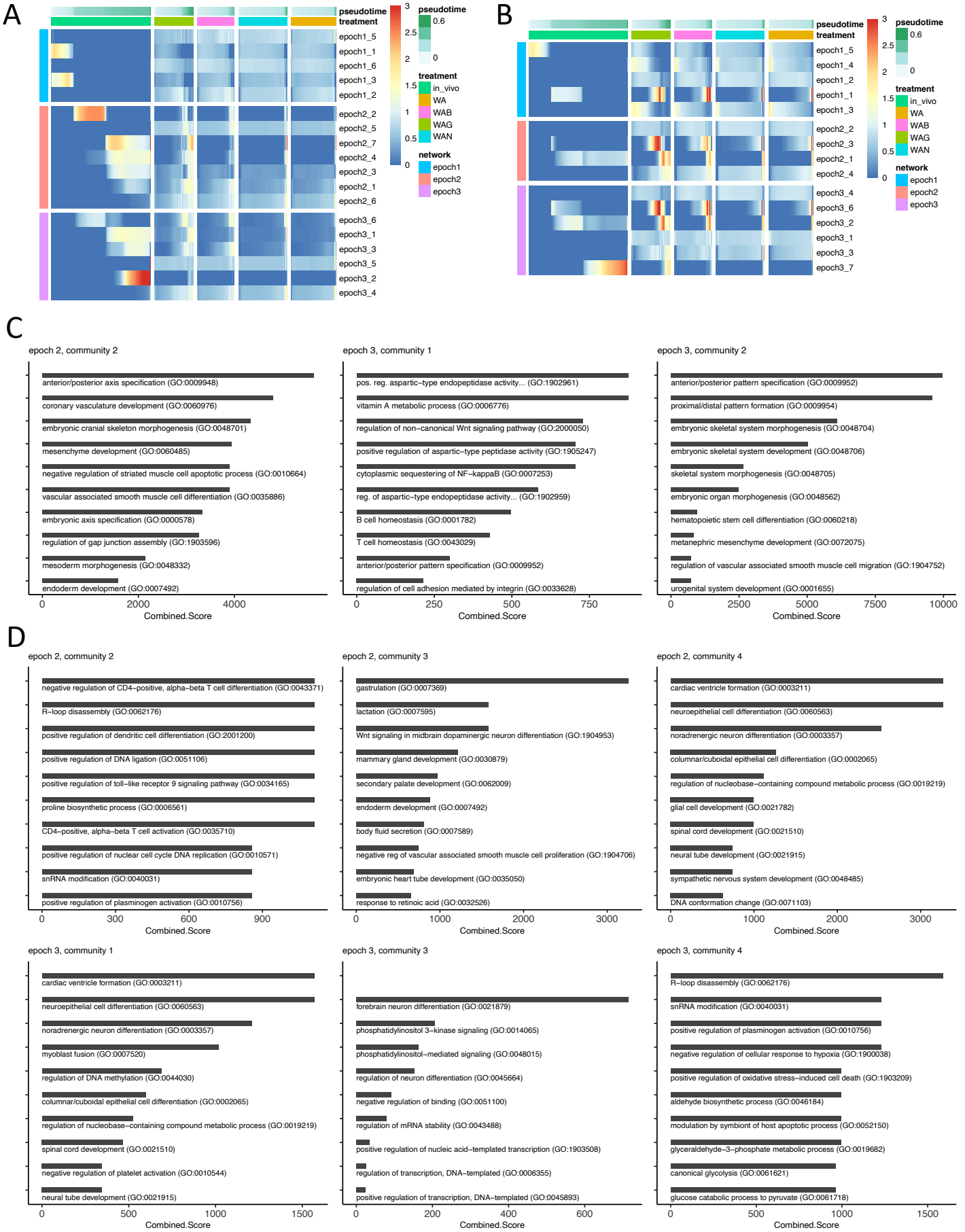

Supplementary Figure 14

Term	Combined.Score
epoch 1, community 2	
positive regulation of stem cell proliferation (GO:2000648)	773.48
regulation of mRNA splicing, via spliceosome (GO:0048024)	203.75
epoch 1, community 3	
glutathione metabolic process (GO:0006749)	405.99
epoch 1, community 4	
cellular response to laminar fluid shear stress (GO:0071499)	1,027.54
myoblast fusion (GO:0007520)	859.88
response to laminar fluid shear stress (GO:0034616)	584.21
regulation of DNA methylation (GO:0044030)	584.21
cellular response to fluid shear stress (GO:0071498)	444.11
male gonad development (GO:0008584)	182.23
development of primary male sexual characteristics (GO:0046546)	182.23
regulation of protein metabolic process (GO:0051246)	155.19
gonad development (GO:0008406)	142.01

Supplementary Figure 15

A

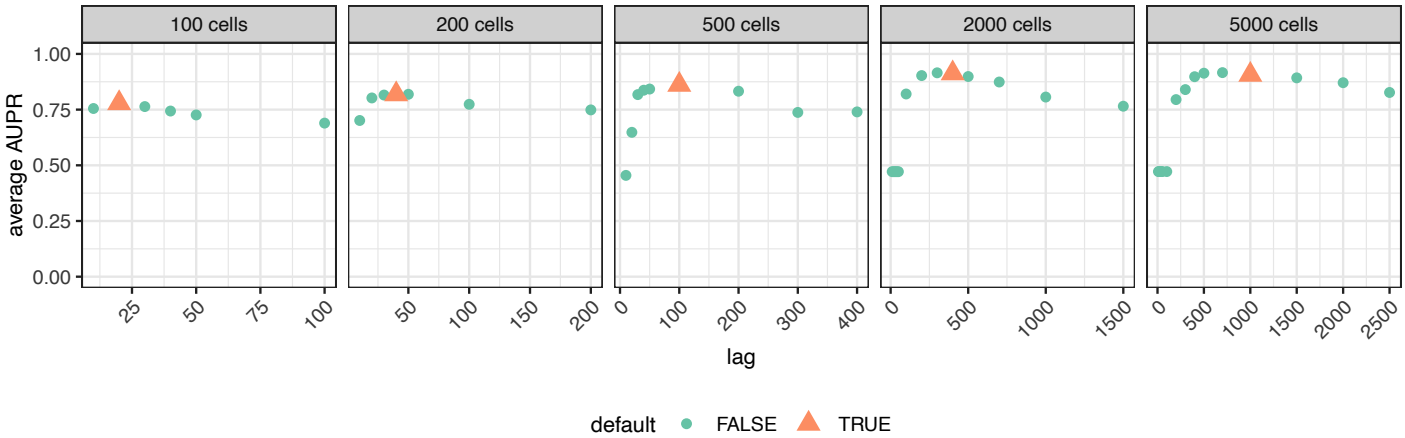

B

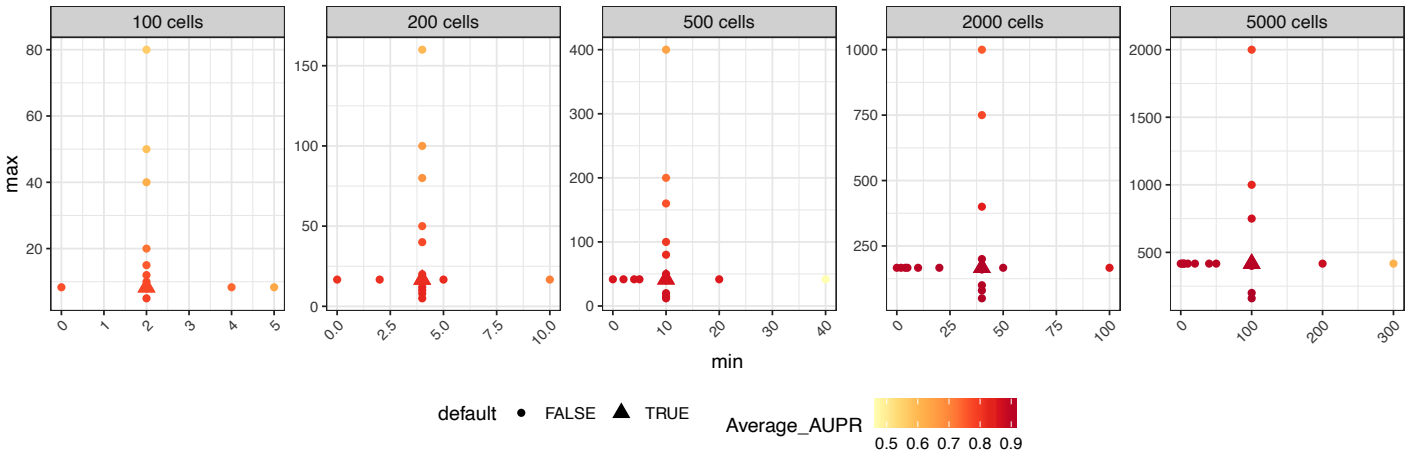

Supplementary Table 1

Cluster	Cell Type Label	Evidence
1	Undifferentiated ESCs	This cluster classifies strongly as inner cell mass and epiblast. It expresses a number of pluripotency genes including Zfp42.
3	Epiblast	This cluster classifies as epiblast with some early ectodermal signature. Fgf5 expression begins here.
0	Primitive Streak	This cluster classifies strongly as primitive streak with some early ectodermal signature. It expresses brachyury.
8	(mesoderm) Presomitic Mesoderm/Somites	This cluster classifies as presomitic mesoderm and somites, with some residual primitive streak. It expresses a number of mesodermal markers including Mesp1.
7,1	(endoderm)	7,0 exhibits strong classification for definitive endoderm and gut endoderm. It expresses definitive endodermal markers including Foxa2 and Sox17. RNA velocity suggests 7,1 cells transition into 7,0, and largely classifies as anterior primitive streak and endoderm.
7,0		
7,2	Node	This cluster strongly classifies as node, and expresses Chordin.
0,4	(neuroectoderm) Early Ectoderm	This cluster classifies weakly as a number of ectodermal cell types, but based on RNA velocity seems to be most similar to early ectodermal cells.
0,2	(neuroectoderm) Early Ectoderm, Forebrain/ Midbrain fated	This cluster classifies weakly as a number of ectodermal cell types including early ectoderm. Based on RNA velocity, this cluster transitions into cluster 5 (forebrain/midbrain fated).
5	(neuroectoderm) Future Brain, Forebrain/ Midbrain	This cluster classifies strongly as forebrain/midbrain with some weaker future spinal cord classification. It expresses Zic1 and En2.
9	(neuroectoderm) Future brain	This cluster classifies weakly as future brain, future spinal cord, and neural crest. It expresses Crabp1 and Tubb3, and RNA velocity suggests it transitions from clusters 2 or 5.
0,3	Early Neuromesodermal Progenitor	This cluster classifies weakly as a number of cell types including primitive streak and early ectoderm, but more strongly as early neuromesodermal progenitor. RNA velocity shows cells in this cluster transition into a neuromesodermal progenitor. Cells in this cluster express T and some Sox2.
4	Neuromesodermal Progenitor	This cluster classifies strongly as neuromesodermal progenitor (late and early). It has some T and Sox2 expression.
2	(neuroectoderm) Future Spinal Cord	This cluster classifies mostly as future spinal cord, and weakly as fore/midbrain. It also expresses many patterning genes from the Hox family indicative of spinal cord fated cells such as Hoxb9.